
Sub-cycle Microscopy and Near-field Spectroscopy of Terahertz Waveforms based on Quantum Dots

Von der Universität Bayreuth
zur Erlangung des Grades eines
Doktors der Naturwissenschaften (Dr. rer. nat.)
genehmigte Abhandlung

von
Moritz Benedikt Heindl
geboren in Tirschenreuth

1. Gutachter: Prof. Dr. Georg Herink
2. Gutachter: Prof. Dr. Markus Lippitz

Tag der Einreichung: 08.10.2024

Tag des Kolloquiums: 19.12.2024

Abstract

Electric fields can be sensed with semiconductor quantum dots as these change their optical properties due to the quantum-confined Stark effect (QCSE). This work describes new techniques to detect and image electric fields of infrared radiation by harnessing the QCSE in colloidal CdSe-CdS core-shell quantum dots. In particular, we detect the near-field of single-cycle terahertz (THz) pulses in gold microstructures using photons from the visible luminescence of the nanocrystals.

First, we give an introduction to the terahertz spectral regime and the employed amplifier laser system. We generate high-field terahertz pulses in a LiNbO₃ crystal with the tilted pulse front technique. Here, we provide parameters for an efficient generation setup. The single-cycle terahertz pulses centered at 1 THz offer peak fields of 400 kV/cm and are characterized by calibrated electro-optical sampling (EOS). Additionally, we describe and employ further techniques for the spatio-temporal characterization.

The second part treats the study and finite-element simulation of field enhancing structures fabricated by photolithography, that increase the terahertz field strengths to several MV/cm. We also give an introduction to low-dimensional semiconductor structures. Subsequently, the QCSE as the main effect in this work is presented, as well as a 1d simulation strategy employing the time-independent Schrödinger equation. We describe sensitive measurement techniques based on differential/lock-in detection. In particular, we present THz-pump/optical-probe setups for the detection of (ultrafast) changes in the absorption and emission of the quantum dots, enabling spectral and spatial resolution of the QCSE. Ultrafast temporal resolution is enabled by tunable, femtosecond laser pulses from an optical parametric amplifier (OPA).

Third, we experimentally introduce the QCSE by applying static fields in plate capacitor structures. The measurements show the main aspects of the QCSE in quantum dots: a reduced bandgap that scales quadratically with the electric field and an altered overlap of the electron and hole wavefunctions that changes the transition dipole moment. The shape and scaling of the spectral changes are supported qualitatively by the 1d simulation. The THz pulses enable ultrafast modulations in the quantum dot absorption that we readout in transient absorption and emission measurements. Additionally, we spectrally map THz-induced changes in the quantum dot absorption with spectrally tuned OPA pulses close to the bandgap. We show first results of a THz-modulated emission in a time window of 10 picoseconds after a quantum dot excitation with high fluence.

The absorption of the quantum dots changes due to their symmetry with the quadratic, rectified field. However, by using a static bias field, we establish an observable that scales linearly in the terahertz electric field. The bias field introduces a preferred direction that allows to induce changes in the quadratic scaling that enable linear field detection. We implement this scheme as an electro-absorptive THz antenna based on the differential readout of the quantum dot absorption. The antenna performance is examined in detail, and the measured terahertz waveforms are verified with EOS. Therefore, we enable the application of quantum dots for THz time-domain spectroscopy, as we also show in first results.

Finally, we introduce the newly developed microscopy technique called Quantum-Probe Field Microscopy (QFIM) that images terahertz electric near-fields with sub-cycle spatial and sub-diffraction limited resolution. Therefore, we locally detect the terahertz-induced changes in the emission due to the QCSE with fluorescence microscopy. We present QFIM by imaging the near-field evolutions in a single bowtie antenna and verify our findings with finite-element simulations. Here, fields up to several MV/cm are mapped, and we achieve an optical resolution far beyond the diffraction limit. Additionally, the technique allows us to map terahertz waveguide propagations in a sub-wavelength slit in the time-domain.

Zusammenfassung

Elektrische Felder können mit Halbleiter-Quantenpunkten erfasst werden, da diese ihre optischen Eigenschaften aufgrund des quantum-confined Stark-Effekts (dt. „Quantenbeschränkter Stark-Effekt“, QCSE) ändern. Diese Arbeit beschreibt neuartige Techniken zur Detektion und Abbildung von elektrischen Feldern ferninfraroter Strahlung auf Basis des QCSE in kolloidalen CdSe-CdS Kern-Schale Quantenpunkten. Insbesondere vermessen wir das Nahfeld von einzyklischen Terahertz (THz) Pulsen in Mikrostrukturen aus Gold mittels sichtbarer Photonen der Nanokristall-Lumineszenz.

Zunächst beschreiben wir den Terahertz-Spektralbereich und das verwendete Laser Verstärkersystem. Wir erzeugen die Hochfeld-Terahertz-Pulse in einem LiNbO₃-Kristall mittels einer gekippten Pulsfront (engl. „tilted pulse front“) des Erzeugerpulses. Hierzu geben wir Parameter für den Aufbau einer effizienten THz-Quelle an. Die einzyklischen Terahertz-Pulse weisen eine elektrische Spitzenfeldstärke von 400 kV/cm bei einer Zentralfrequenz von 1 THz auf. Die zeitaufgelöste Messung des elektrischen Feldes wird mittels kalibrierter elektrooptischer Abtastung (engl. „electro-optical sampling“, EOS) durchgeführt. Zusätzlich beschreiben und nutzen wir weitere Techniken zur raum-zeitlichen Charakterisierung der ferninfraroten Strahlung.

Der zweite Abschnitt der Arbeit behandelt die Feldverstärkung der Terahertz-Felder in Mikrostrukturen aus Gold, welche mittels optischer Photolithographie hergestellt werden und die Feldstärken bis zu mehreren MV/cm verstärken. Hierzu nutzen wir Finite-Elemente Simulationen. Anschließend geben wir eine Einführung in niedrig-dimensionale Halbleiterstrukturen und stellen den zentralen Effekt dieser Arbeit vor: den quantum-confined Stark-Effekt. Ebenfalls beschrieben wir die Simulation dieses Effekts in einer Dimension mittels der zeitunabhängigen Schrödinger-Gleichung. Experimentell erhalten wir Zugang zum QCSE mittels empfindlicher differentieller oder Lock-in Detektion, die es ermöglicht Änderungen in der Emission und Absorption der Quantenpunkte mit hoher zeitlicher Auflösung zu vermessen. Hierzu verwenden wir spektral verstimmbare Femtosekunden-Pulse eines optisch parametrischen Verstärkers (engl. „optical parametric amplifier“, OPA). Die verwendeten Anrege-/Abfrage-Schemata ermöglichen die spektrale und räumliche Auflösung des QCSE.

Experimentell untersuchen wir den QCSE zunächst mittels statischer, elektrischer Felder in Strukturen ähnlich einem Plattenkondensator. Diese Messungen weisen die zentralen Punkte des QCSE auf: eine reduzierte Bandlücke, welche quadratisch mit dem Feld skaliert und ein modifiziertes Übergangsdipolmoment, da der Überlapp der Elektron- und Loch-Wellenfunktionen verändert wird. Die Form und Skalierung der spektralen Änderungen in der Quantenpunkt-Emission wird qualitativ von der 1D-Simulation reproduziert. Ultraschnelle Modulationen aufgrund des QCSE werden anschließend mittels der Felder der Terahertz-Strahlung erzeugt, welche wir in Emission und Absorption der Nanokristalle nachweisen. Schließlich studieren wir Änderungen im Absorptionsspektrum nahe der Bandkante der Quantenpunkte mithilfe von OPA-Pulsen. Wir beschließen diesen Abschnitt mit ersten Ergebnissen, welche die Modulation der Quantenpunkt-Emission direkt durch die Terahertz-Felder zeigen. Diese tritt in einem Zeitfenster von 10 Pikosekunden nach einer Anregung mit hoher Fluenz auf.

Die Absorption in den Quantenpunkten ändert sich aufgrund ihrer Symmetrie quadratisch mit dem gleichgerichteten elektrischen Feld. Jedoch zeigen wir, dass mittels eines zusätzlichen statischen, elektrischen Feldes eine Messgröße erzeugt werden kann, welche die lineare Terahertz-Feldstärke misst. Dies gelingt uns durch das statische Feld, welche eine Vorzugsrichtung erzeugt und Änderungen in der quadratischen Skalierung bewirkt, welche schlussendlich eine lineare Felddetektion ermöglichen. Wir implementieren diese Methode mittels einer elektroabsorptiven THz-Antenne, basierend auf der differentiellen Messung der erzeugten Änderungen in der Absorption der Quantenpunkte. Die Antenne wird im Detail analysiert und die vermessenen Terahertz-Wellenformen mit EOS-Messungen überprüft. Somit haben wir die Nutzung von Quantenpunkten für die Terahertz-Zeitbereichs-Spektroskopie ermöglicht, wie wir auch anhand erster Ergebnisse zeigen.

Abschließend beschreiben wir die neu entwickelte Mikroskopie-Methode Quantum-Probe Field Microscopy (QFIM), welche Schwingungen von Terahertz-Nahfeldern mit einer Auflösung weit unter dem Beugungslimit abbilden kann. Dafür detektieren wir THz-induzierte, lokale Änderungen in der Emission der Quantenpunkte aufgrund des QCSE mit konventioneller Fluoreszenzmikroskopie. Wir demonstrieren QFIM durch Abbildung der zeitaufgelösten Nahfelder in einer einzelnen THz-Antenne und bestätigen unsere Ergebnisse mittels Finite-Elemente Simulationen. Elektrische Felder mit Stärken von bis zu einigen MV/cm werden mit einer Auflösung deutlich jenseits der Beugungsgrenze abgebildet. Ebenso erlaubt uns die Methode, die Propagation von Terahertz-Pulsen in einer Wellenleiterstruktur zu verfolgen, welche aus Schlitzen mit einer Größe weit unter der Terahertz-Wellenlänge besteht.

Publications

Articles in scientific journals, part of this thesis

1. Heindl, M. B., Zhu, H., Bawendi, M. G. & Herink, G. Electro-Absorptive Quantum Dot Antenna Resolves Terahertz Lightwaves via Biased Stark Effect. *ACS Photonics* **11**, 13-17 (2024)
2. Heindl, M. B., Kirkwood, N., Lauster, T., Lang, J. A., Retsch, M., Mulvaney, P. & Herink, G. Ultrafast imaging of terahertz electric waveforms using quantum dots. *Light: Science & Applications* **11**, 5 (2022).

Articles in scientific journals, not part of this thesis

1. Maleki, A., Heindl, M. B., Xin, Y., Boyd, W. R., Herink, G. & Ménard, J.-M. Strategies to enhance THz harmonic generation combining multilayered, gated, and metamaterial-based architectures. *Light: Science & Applications* **14**, 44 (2025).
2. Tiedeck, S., Heindl, M. B., Kramlinger, P., Naas, J., Brütting, F., Kirkwood, N., Mulvaney, P. & Herink, G. Single-Pixel Fluorescence Spectroscopy Using Near-Field Dispersion for Single-Photon Counting and Single-Shot Acquisition. *ACS Photonics* **9**, 2931-2937 (2022)

Contributions on international conferences

1. Heindl, M. B., Kirkwood, N., Lauster, T., Retsch, M., Mulvaney, P. & Herink, G. Sampling polar THz nearfields using nonpolar Stark-effect. **Talk**. DPG spring meeting 2023. Dresden - Germany
2. Heindl, M. B., Kirkwood, N., Lauster, T., Retsch, M., Lang, J. A., Mulvaney, P. & Herink, G. Spatially-resolved THz near-field spectroscopy. **Talk**. DPG meeting 2022. Regensburg - Germany
3. Heindl, M. B., Kirkwood, N., Lauster, T., Retsch, M., Lang, J. A., Mulvaney, P. & Herink, G. Ultrafast Field Microscopy of Terahertz Near-field Waveforms. **Talk**. DPG spring meeting 2022. Erlangen - Germany
4. Heindl, M. B., Kirkwood, N., Lauster, T., Retsch, M., Lang, J. A., Mulvaney, P. & Herink, G. Terahertz Electric Field Microscopy of Ultrafast Near-fields. **Talk**. CLEO 2022. San José - United States of America
5. Heindl, M. B., Herink, G. Phase-resolved detection of strong terahertz nearfields. **Poster**. DPG spring meeting 2019. Regensburg - Germany

Further contributions on workshops and seminars

1. Heindl, M. B., Kirkwood, N., Lauster, T., Retsch, M., Lang, J. A., Mulvaney, P. & Herink, G. Spatially-resolved THz near-field spectroscopy. **Talk**. Seminar, 2022. Hirschegg - Austria
2. Heindl, M. B., Kirkwood, N., Lauster, T., Retsch, M., Lang, J. A., Mulvaney, P. & Herink, G. Terahertz Electric Field Microscopy of Ultrafast Near-Fields. **Talk**. Seminar in the group of Prof. Jalali at UCLA, 2022. Los Angeles - United States of America
3. Heindl, M. B., Herink, G. Manipulation of quantum systems with strong THz fields. **Talk**. Seminar, 2019. Hirschegg - Austria
4. Heindl, M. B., Herink, G. Manipulation of quantum systems via intense THz radiation. **Poster**. Summer school on ultrafast dynamics in solids, 2018. Göttingen - Germany

Contents

1	Introduction and outline	1
2	Generation and characterization of intense single-cycle terahertz pulses	3
2.1	Introduction to terahertz radiation	3
2.2	1 mJ ytterbium amplifier laser system and optical parametric amplifier . .	4
2.3	Terahertz generation processes	6
2.4	Design of an efficient terahertz generation setup based on the tilted pulse front method	10
2.5	Electro-optical sampling of terahertz pulses with absolute electric field strength calibration	12
2.6	Experimental realization of generation and detection of strong THz pulses	17
2.7	Spatio-temporal characterization of single-cycle terahertz pulses	18
3	Theory and detection of the quantum-confined Stark-effect in strong electric fields	27
3.1	Electric field enhancement in gold microstructures	27
3.2	Quantum-confined Stark-effect in low-dimensional semiconductors	35
3.3	Experimental detection of the QCSE in absorption and emission	44
4	Modulation of quantum dot absorption and emission with ultrafast and static electric fields	49
4.1	Colloidal CdSe-CdS core-shell quantum dots	49
4.2	1d simulation of the quantum-confined Stark-effect	49
4.3	Emission and absorption modulation with static fields	53
4.4	Ultrafast modulation of quantum dot absorption	55
4.5	Polarity reconstruction strategies for rectified signals	59
4.6	Outlook: Ultrafast modulation of quantum dot emission	63

5	Electro-absorptive detection of terahertz fields by field biasing	67
5.1	Concept of biased QCSE	67
5.2	Electro-absorptive THz sampling using quantum dots	70
5.3	First spectroscopic application of the quantum dot antenna	75
5.4	Summary & outlook	77
6	Quantum-Probe Field Microscopy	79
6.1	Experimental realization of an ultrafast field microscope based on quantum dots	80
6.2	Imaging of ultrafast terahertz field evolutions in a bowtie antenna	81
6.3	Mapping of field patterns in a split-ring resonator	86
6.4	Tracking of propagating terahertz waves in a sub-wavelength slit	87
6.5	Summary & outlook	91
7	Conclusion and outlook	93
	Acronyms	97
	Bibliography	99

Introduction and outline

Following the theoretical work by J. C. Maxwell [1] in the middle of the 19th century, that proposed electromagnetic fields that propagate as waves with the speed of light, H. Hertz conducted experiments to prove the wave character of the electromagnetic radiation. He generated radiation with a frequency of approximately 30 MHz, which he detected after propagation through air in the dielectric breakdown of a loop antenna [2]. This resulted in a small spark, converting the radio frequency radiation to visible luminescence, that Hertz detected with his eyes. By moving the receiver antenna along the propagation direction of a standing wave, he could follow the amplitude of the electromagnetic wave and, thus, prove its existence.

In this work, we resolve the oscillations of the electric field of picosecond pulses in the terahertz (THz) spectral region, also using visible luminescence. In particular, we employ field-sensitive modulation of the absorption spectrum of semiconductors. Control of the optical properties with an external electric field was shown first in bulk semiconductors by W. Franz and L. Keldysh in the late 1950s [3, 4]. However, much higher sensitivity and robustness to high fields is provided by low-dimensional semiconductor structures [5], where the electronic motion is spatially confined. There, the field-modulated absorption is governed by the quantum confinement and is therefore called the quantum-confined Stark-effect (QCSE). In this work, we employ semiconductor nanocrystals that are highly confined in all spatial dimensions to only a few nanometers: colloidal quantum dots.

In 2023, the Nobel Prize for Chemistry was awarded to A. I. Ekimov, L. E. Brus, and M. G. Bawendi for the discovery and synthesis of quantum dots. Ekimov and Brus studied the dependency of the crystal size on its color and drew the conclusion that the energy from the emitted photons scales with the inverse squared size due to the quantum confinement [6, 7]. This enabled to freely tune the luminescence of the quantum dots by their size. For industrial purposes or in general ensemble applications of the crystals, as employed in this work, a procedure to fabricate large batches of quantum dots with nearly monodisperse size was needed. Such a method was provided first by Bawendi and coworkers in 1993 with their hot-injection technique [8].

The QCSE was first shown in quantum wells by D. A. B. Miller in 1984 [5] and in single quantum dots by Empedocles and Bawendi in 1997 [9]. The first application of the QCSE to the emerging field of THz photonics is described by Turchinovich and coworkers in 2010, showing that the optical properties can be modulated on an ultrafast timescale [10].

Due to their small size and overall flexibility, the quantum dots are predestined to act as local probes to sense electric fields on a microscopic, sub-wavelength scale, as they play a role in nanodevices, polaritonics, and plasmonics [11–13]. In the THz regime, spatial-temporal distributions of such fields are accessible with, e.g., electro-optic sampling techniques and Auston switches [14, 15], both typically used for detection of THz radiation in the time-domain. Also, typical high-resolution approaches, such as scanning near-field microscopy, scanning-tunnel microscopy, and electron microscopy have been successfully applied to the THz range, delivering spatial resolutions down to nanometers [16–18]. As a main result of this thesis, we present a novel THz near-field technique based on QCSE in quantum dots, that enables ultrafast field imaging via far-field fluorescence, especially for high electric field strengths, which e.g., exclude the use of tip-based methods.

All the presented experiments have been completely designed and set up during this dissertation. In chapter 2, we introduce the far-infrared THz radiation and the employed high-power pulsed laser system. Special attention is paid to the design of an experimental setup to efficiently generate phase-stable, single-cycle THz pulses from the near-infrared laser pulses. This is followed by the description of the employed spatial and temporal detection techniques for THz radiation. Chapter 3 introduces the key elements underlying strong-field experiments, namely THz field enhancement in gold microstructures, the quantum-confined Stark-effect and optical pump/probe readout strategies employing visible radiation. An experimental characterization of the QCSE is given in chapter 4. There, we present measurements with static and ultrafast THz bias fields and discuss them with respect to QCSE simulations based on a 1d model. Owing to the symmetry of the quantum dots, the QCSE is insensitive to the field polarization, and therefore, we present two signal-theoretical approaches to recover the polarity. We conclude this chapter with first results on direct THz modulated emission in quantum dots, an effect we observe at excitation with high fluence. In chapter 5, we address the problem of polar field detection in quantum dots from a different perspective by introducing a novel electro-absorptive terahertz antenna. Here, the field polarity is detected by employing a known static field on top of the THz field, allowing us to break the quantum dot symmetry and measure the waveform of the electric field directly. This enables the use of quantum dots as a spectroscopic tool, as we show in first applications. In chapter 6, we describe Quantum-Probe Field Microscopy (QFIM), a new technique to image THz near-fields with sub-cycle and sub-diffraction-limited resolution using quantum dots. In particular, we detect the field-induced local absorption changes in the quantum dot emission far-field in the vicinity of THz antennas employing conventional fluorescence microscopy. We investigate a single bowtie antenna, study propagations of THz waves in micro-slit waveguides, and compare our findings to simulations. The concluding chapter 7 summarizes the work and provides possible directions for future studies.

Generation and characterization of intense single-cycle terahertz pulses

2.1 Introduction to terahertz radiation

Throughout this thesis, terahertz radiation is used as an electric field bias. In particular, ultrafast THz waveforms, featuring only few electric field cycles in the picosecond temporal regime, are used for this purpose, providing fields at much higher frequencies than accessible with conventional electronics. Following its name, the spectrum spans from roughly 0.1 THz to 10 THz, thus, lies in the far-infrared region, in between electronically generable radiation and conventional photonics [19], as depicted in fig. 2.1. Until recently, this spectral region was often referred to as the "terahertz gap" due to the lack of generation mechanisms, especially for table-top or turn-key devices. As date of this thesis, multiple ways to generate THz radiation have been established. The most prominent ones are presented in section 2.3.

The low-frequency character of THz radiation, e.g., provides interesting applications in non-destructive material testing, sensing, and spectroscopy as the photon energy is in the range of only a few to ten meV [20]. Radiation centered at 1 THz corresponding to photon energy of 4 meV is employed in all experiments, thus, featuring energies far below the thermal energy of 25 meV at 300 K temperature. In this spectral region, a lot of fundamental excitations take place, e.g., rotation vibrations (gas), phonons (solids), and hydrogen bond vibrations (liquids), that can be accessed and studied with THz fields [21].

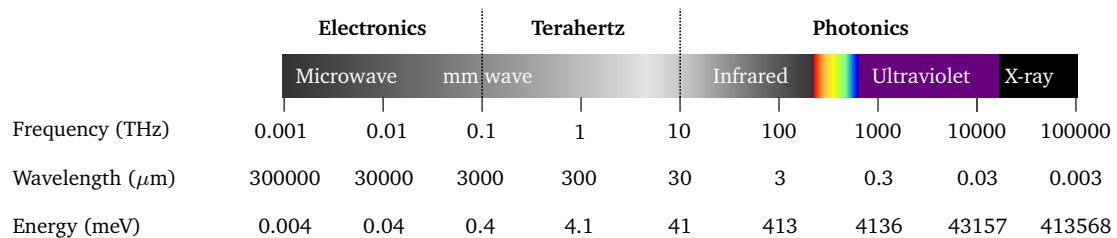


Fig. 2.1: Terahertz radiation in the electromagnetic spectrum. Illustration of the terahertz spectral region in between electronics and photonics, along with the corresponding frequency, wavelength and energy.

In particular, phase-stable THz radiation, with its rather long periods of electric field oscillations, allows for sampling of its electric field with femtosecond laser pulses. Thus, phase-resolved detection of the THz field enables the direct acquisition of complex material parameters, e.g., complex refractive indices. In contrast to conventional frequency-domain spectroscopy, this method is called THz time-domain spectroscopy (TDS) [22].

2.2 1 mJ ytterbium amplifier laser system and optical parametric amplifier

Yb:KGW amplifier system

The generation of strong terahertz pulses requires short and high-energy laser pulses in the visible to infrared spectral region, as the energy conversion efficiency is typically below 1 % for the employed tilted pulse front technique in lithium niobate [23]. Therefore, we use a regenerative amplifier laser system (Pharos SP, *Light Conversion*) at a repetition rate of 10 kHz with a pulse energy of 1 mJ, corresponding to an optical power of 10 W. The output pulse length is specified to ~ 180 fs and the spectrum is centered around 1030 nm. In detail, the regenerative amplifier is seeded by pulses from a ytterbium oscillator with a repetition rate of 76 MHz based on Kerr-lens mode-locking. Ytterbium-doped potassium gadolinium tungstate (Yb:KGW) is used as an active medium in the amplifier and is pumped by continuous-wave diodes. The seed pulses are injected by a Pockels cell, amplified via chirped-pulse amplification, and ejected by the same Pockels cell. In short, this method consists of stretching the seed pulses to low peak powers that can be safely amplified in the Yb:KGW crystal and finally compressing the pulses again to achieve ultrashort high-energy pulses.

Optical parametric amplifier

In the experiments, we use femtosecond laser pulses with widely tunable wavelengths to pump or probe samples. For this purpose, we utilize a collinear, optical parametric amplifier (OPA) which is pumped by a small fraction ($25 \mu\text{J}$) of the power from the amplifier system. The employed commercial OPA (Orpheus-HP, *Light conversion*) offers pulses from 310 nm up to 16 000 nm wavelength. In general, the OPA is based on the second-order nonlinear process optical parametric amplification, which involves three

photons with frequencies ω_p (pump), ω_s (signal) and ω_i (idler), whereas $\omega_s < \omega_p$. The nonlinear polarization $P^{(2)}(\omega_i)$ reads as [24]:

$$P^{(2)}(\omega_i = \omega_p - \omega_s) = \varepsilon_0 \chi^{(2)}(\omega_p, -\omega_s) E(\omega_p) E^*(\omega_s) \quad (2.1)$$

A weak signal beam is amplified by depletion of the pump beam and the additional creation of idler radiation, as illustrated in fig. 2.2(a) [24]. Experimentally, most of the input light from the Pharos is frequency-doubled by second harmonic generation (SHG) to provide the pump beam. Whitelight continuum is generated in a white light (WL) crystal by a part of the input beam and acts as seed for the parametric amplification. The used OPA is based on a two-stage amplification design, as sketched in fig. 2.2(b). The desired output wavelength is chosen from the white light seed by tuning the phase-matching angle of the OPA crystal and frequency filters at the output. A set of different output wavelengths of the signal beam is presented in fig. 2.2(c).

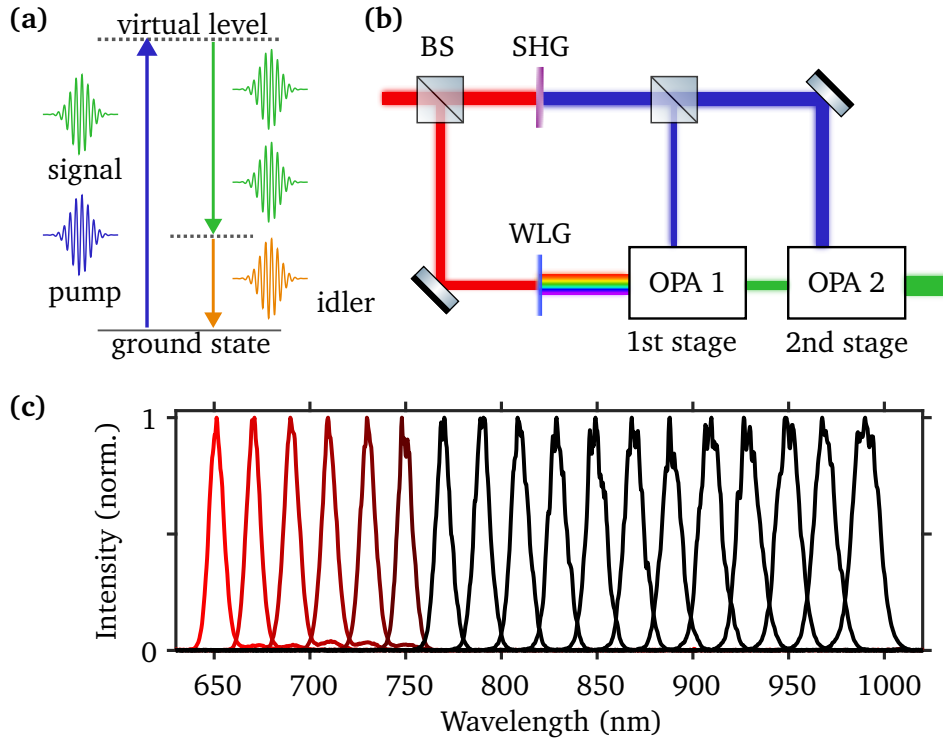


Fig. 2.2: Optical parametric amplification. (a) A photon from the pump beam is annihilated, leading to the creation of an idler and an additional signal photon via virtual levels (dashed). Adapted from [25]. (b) Schematic sketch of the employed two-stage parametric amplifier. The input beam from the amplifier system (red) is split up with a beam splitter to generate white light (seed) and SHG (blue, pump). A small part of the SHG is used to pump the first stage, amplifying a narrow part of the continuum (gain 10^3 to 10^5). The power of the signal (green) pulse is further amplified in the second stage (gain 10^1 to 10^2) [25]. The idler beam is not shown. Adapted from [25]. (c) OPA spectra of the signal beam in steps of 20 nm measured with the internal OPA spectrometer.

The available wavelength range of the OPA is further extended by SHG of the signal (600 nm to 1100 nm) and idler (1000 nm to 2600 nm) beams – building up a wide, continuous range of frequencies that was used throughout the thesis. Additionally, difference-frequency generation enables access to infrared radiation up to 16 μm .

2.3 Terahertz generation processes

Overview of generation processes

In an ongoing effort to close the terahertz gap, many different ways of generating (strong) terahertz radiation have been developed – broad reviews are presented in refs. [23, 26] on the basis of which we now provide an overview. In general, a distinction can be made between low-field applications such as THz time-domain spectroscopy, typically driven by oscillator systems at MHz repetition rates, and high-field applications, for instance, THz high-harmonic generation, powered by amplified laser systems or large-scale facilities typically at repetition rates from 1 to 100 kHz [22, 27, 28].

So-called photoconductive antennas (PCA) provide a broadly used platform for time-domain spectroscopy [29]. In short, the radiation is generated in semiconductors that are externally biased in an antenna structure. Free charge carriers are generated by a short laser pulse and accelerated, yielding the emission of pulsed THz radiation. The resulting THz spectrum is governed by the carrier relaxation time. Inversely, the THz radiation can be detected with a PCA by measuring the current of free charge carriers accelerated by the electric field of the THz pulse. Another technique relies on plasma generation, e.g., in air [30], where a short laser pulse and its second harmonic are focused in ambient air, resulting in a plasma. The THz generation process can be described in a simple picture as a frequency mixing in the plasma. The THz bandwidth can be tuned by the pump pulse duration, allowing for extremely broad THz spectra. Vice versa, the principle can also be used to detect THz radiation and is known as air-biased coherent detection or air-breakdown coherent detection (ABCD) [31, 32]. To date, most high-field THz experiments rely on the $\chi^{(2)}$ -processes optical rectification (OR) and/or difference-frequency generation (DFG) in semiconductors, organic and inorganic crystals [23]. This mechanism is employed in the experiments in the present thesis and is described in detail in the section below. More recently, THz generation and detection based on spintronic emitters have emerged, offering high bandwidths and peak fields comparable to OR-based techniques [33–35]. The aforementioned techniques are mostly implemented in table-top experiments. However, there also exist large-scale facilities such as TELBE (High-Field

High-Repetition-Rate Terahertz facility @ ELBE) based on electron accelerators that provide high fields and frequency-tunable THz pulses at high repetition rates [36].

Optical rectification

In this work, the THz radiation is generated via OR / DFG of near-infrared pulses in a nonlinear crystal. In particular, DFG can be described as a $\chi^{(2)}$ -process and, thus, two strong, interacting electric fields $E(\omega_1)$ and $E(\omega_2)$ at frequencies ω_1 and ω_2 lead to a polarization $P^{(2)}$ with the difference frequency $\omega_3 = \omega_1 - \omega_2$, similar to the OPA process [24]:

$$P^{(2)}(\omega_3) = \varepsilon_0 \chi^{(2)}(\omega_1, -\omega_2) E(\omega_1) E^*(\omega_2) \quad (2.2)$$

OR can be understood as DFG in the case $\omega_2 \rightarrow \omega_1$, leading to a quasi-static polarization in the medium [24]:

$$P^{(2)}(\omega_3 \rightarrow 0) = \varepsilon_0 \chi^{(2)}(\omega_1, -\omega_2) E(\omega_1) E^*(\omega_2 \rightarrow \omega_1) \quad (2.3)$$

Experimentally, the frequency conversion is driven by broadband femtosecond laser pulses. Therefore, with $\omega_2 = \omega_1 = \omega$ and $\omega_3 = \omega_{\text{THz}}$ the polarization $P^{(2)}(\omega_3)$ can be rewritten as [26]:

$$P^{(2)}(\omega_{\text{THz}}) = \varepsilon_0 \chi^{(2)}(\omega, -\omega) \int_0^\infty E(\omega + \omega_{\text{THz}}) E^*(\omega) d\omega \quad (2.4)$$

That means every photon pair in the bandwidth of the optical pulse with a frequency difference of ω_{THz} contributes to a photon at ω_{THz} . This leads to a continuous THz spectrum, which offers a bandwidth that is theoretically limited by the bandwidth of the optical pulse, as illustrated exemplarily in fig. 2.3.

Moreover, comparable to other nonlinear processes such as second-harmonic generation, OR has to fulfill a phase matching condition to efficiently generate THz radiation in a macroscopic medium. In general, the following condition for the involved wave vectors \vec{k} has to be met [26]:

$$\Delta \vec{k}(\omega_{\text{THz}}) = \vec{k}(\omega_{\text{THz}}) + \vec{k}(\omega) - \vec{k}(\omega + \omega_{\text{THz}}) = 0 \quad (2.5)$$

The THz frequency is much smaller than the optical, therefore $\vec{k}(\omega) - \vec{k}(\omega + \omega_{\text{THz}})$ can be simplified to $\partial \vec{k} / \partial \omega \cdot \omega_{\text{THz}}$, resulting in a velocity matching condition involving the THz phase velocity ν_{THz} and the group velocity of the optical beam ν_g [26]:

$$\nu_{\text{THz}} = \nu_g \quad (2.6)$$

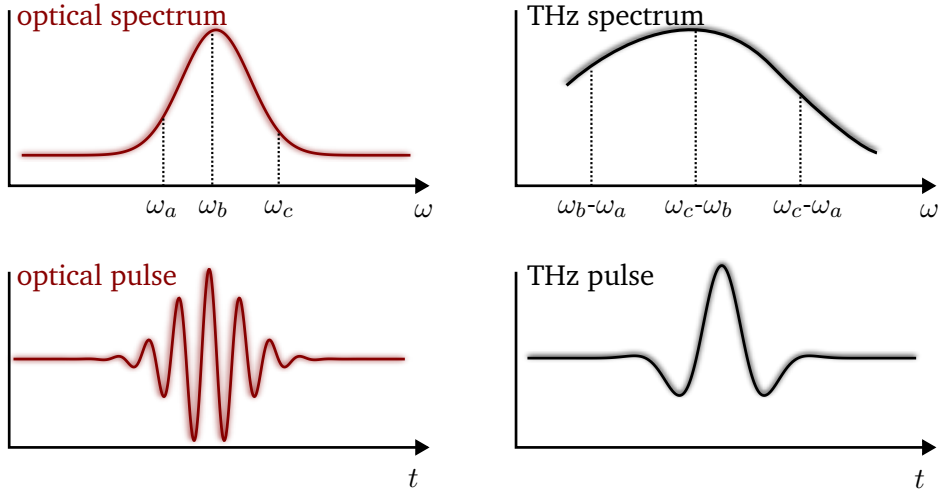


Fig. 2.3: Terahertz generation via OR and DFG. Starting from a femtosecond laser pulse (red) with a broad spectrum, we follow the generation of THz radiation for three exemplary frequencies ω_i . Besides the DC contributions for degenerated frequencies, three difference pairs can be allocated in the THz spectrum (black). Correspondingly, in the time-domain (t), a femtosecond optical pulse with few cycles of the electric field is converted into a single-cycle pulse at THz frequencies. Adapted from [24].

Tab. 2.1: Overview of THz crystals using OR. Nonlinear coefficient d_{eff} (pmV^{-1}), refractive and group refractive index n , n_g at 1030 nm, refractive index in the THz regime n_{THz} , THz absorption coefficient α_{THz} (cm^{-1}) and figure of merit FOM ($\text{pm}^2 \text{cm}^2 \text{V}^{-2}$) for various crystals used in the THz generation via OR. Table adapted from [37]. Values for 1030 nm were added as indicated, all THz values at 1 THz except DAST (0.8 THz).

Material	d_{eff}	n	n_g	n_{THz}	α_{THz}	FOM
CdTe	72.2 [38]	2.83 [39]	3.27 [39]	3.24	4.8	8.03
GaAs	53.0 [38]	3.49 [40]	3.99 [40]	3.59	0.5	2.57
GaP	22.7 [41]	3.11 [42]	3.33 [42]	3.34	0.2	0.64
ZnTe	60.3 [38]	2.78 [39]	2.98 [39]	3.17	1.3	5.94
sLN	162 [38]	2.14 [43]	2.21 [43]	4.96	17	16.0
sLN, 100K					4.8	46.2
DAST	383 [44]	2.22 [44]	2.60 [44]	2.58	50	18.4

Various materials have been used to generate intense THz radiation via OR, including organic crystals (e.g., DAST), inorganic crystals such as LiNbO_3 , and semiconductors (GaP, ZnTe, ...). The energy conversion efficiency can be described with a figure of merit (FOM) taking into account the nonlinear coefficient d_{eff} , refractive index n at 1030 nm, refractive index in the THz regime n_{THz} , THz absorption coefficient α_{THz} and the length of the nonlinear crystal L [37]:

$$\text{FOM}_{NA} = \frac{d_{\text{eff}}^2 L^2}{n^2 n_{\text{THz}}} \quad (2.7)$$

$$\text{FOM}_A = \frac{4d_{\text{eff}}^2}{n^2 n_{\text{THz}} \alpha_{\text{THz}}^2} \quad (2.8)$$

For highly absorptive generation media with a THz absorption coefficient $\alpha_{\text{THz}} > 5 \text{ cm}^{-1}$ FOM_A is used. In the opposite case, FOM_{NA} determines the efficiency, and $L = 2 \text{ mm}$ is used [37]. The relevant parameters and the FOM for various crystals are shown in table 2.1. Besides organic crystals such as DAST, LiNbO_3 provides the highest nonlinear coefficient d_{eff} resulting in a high figure of merit, which can be further improved by cooling the crystal. However, the mismatch of the group index at 1030 nm and the phase index at 1 THz is large, ruling out direct collinear pumping. The latter results in a Cherenkov-like cone emission of terahertz radiation, which is experimentally difficult to collect [45]. A non-collinear generation scheme was presented by Hebling et al. in ref. [46], that uses a tilted pulse front to achieve phase velocity matching in LiNbO_3 . Therefore, the near-infrared pump beam must undergo a tilting of the intensity front of the pulse. Experimentally, this is achieved by a prism or diffraction grating that induces an angular dispersion $\frac{d\epsilon}{d\lambda}$ resulting in an angle between the pulse front and the phase front of the beam. The relation between pulse front tilt γ and angular dispersion $\frac{d\epsilon}{d\lambda}$ can be described as follows [47]:

$$\tan \gamma = -\frac{n}{n_g} \lambda_0 \frac{d\epsilon}{d\lambda} \quad (2.9)$$

Here, λ_0 denotes the mean wavelength, n and n_g the refractive and group index, respectively, of the medium in which the pulse front tilt is investigated – the angles and the pulse front tilt are illustrated in fig. 2.4.

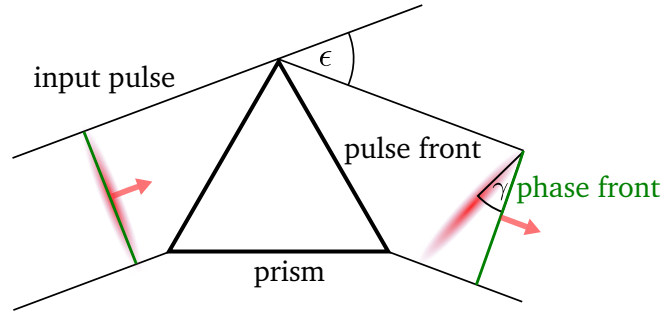


Fig. 2.4: Pulse front tilt due to a prism. The pulse front, described by locations of maximum intensity, encloses a tilt angle γ with the phase front. Adapted from [47].

A pump beam with a pulse front tilt γ leads to a new phase matching condition [46]:

$$\nu_{\text{THz}} = \cos(\gamma) \nu_g \quad (2.10)$$

$$n_{\text{THz}} = \cos(\gamma) n_g \quad (2.11)$$

The necessary pulse front tilt for a 1030 nm pump wavelength and 1 THz frequency can now be calculated from $n_{\text{THz}} = 4.96$ and $n_g = 2.21$ [43, 48]. For pump pulses with 1030 nm wavelength, a pulse front tilt of 63.5° is optimal for phase matching at 1 THz. A schematic setup for THz generation with a tilted pulse front is displayed in fig. 2.5. Since in this configuration, the THz radiation propagates non-collinear to the pump beam, the

LiNbO₃ crystal is cut at an angle of γ so that the beam leaves the material perpendicular to the surface. Furthermore, the pump beam is vertically polarized, parallel to the z-axis of the crystal, providing the highest efficiency. In order to avoid damage due to the photorefractive effect, we use stoichiometric LiNbO₃ doped with 1 % MgO [49]. The experimental realization of the optimal pulse front tilt, along with the full experimental setup, is described in detail in the upcoming section 2.4.

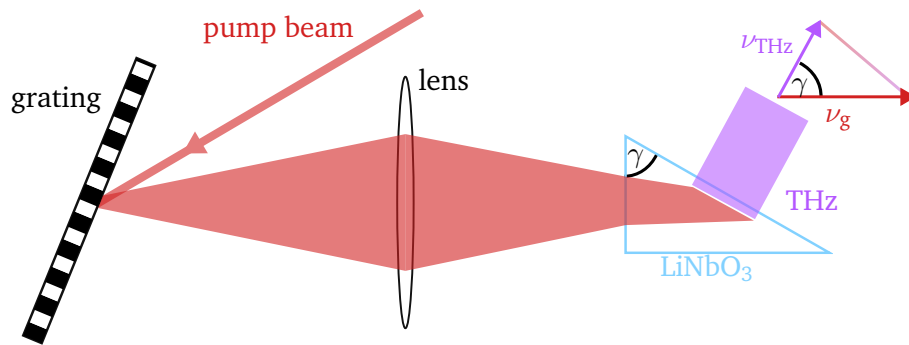


Fig. 2.5: Schematic setup for THz generation in LiNbO₃ with the tilted pulse front method. The near-infrared pump beam is dispersed by a grating, and the resulting pulse front tilt γ is imaged in a cut LiNbO₃ crystal. This leads to an efficient generation of THz radiation that exits the crystal perpendicular to its surface. Additionally, the phase velocity matching condition is illustrated. Adapted from [50].

2.4 Design of an efficient terahertz generation setup based on the tilted pulse front method

The tilted pulse front method in LiNbO₃ is widely used for high-field THz pulses but does not allow for a simple collinear scheme. Typically, gratings are used in this THz generation technique to induce the tilted pulse front. However, there also exist more exotic configurations, including echelons and phase masks [51]. In all cases, the pump pulse on the grating is imaged inside a (cut) LiNbO₃ crystal. In the grating case, this can be achieved by either a single-lens or a two-lens telescope. According to ref. [50], a two-lens telescope consisting of achromatic lenses offers far less imaging distortions compared to the use of a single lens or singlet lenses, thus resulting in a higher THz generation efficiency.

Optimal parameters for the tilted pulse front setup are derived in ref. [50, 52] and will now be discussed. A schematic sketch with all relevant parameters is shown in fig. 2.6.

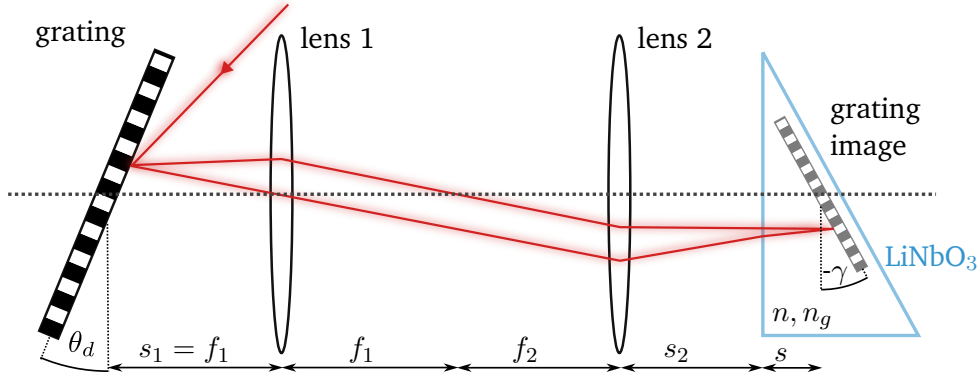


Fig. 2.6: Tilted pulse front scheme with a two-lens telescope. The pump beam on the grating is imaged inside a cut nonlinear crystal LiNbO_3 . Adapted from [52].

Optimal phase matching and imaging conditions for a grating with grating period p are found:

$$\begin{aligned}\sin(\theta_d) &= \frac{\lambda_0}{nn_g p} a \\ \sin(\theta_i) &= \frac{\lambda_0}{p} \left(1 - \frac{a}{nn_g} \right) \\ s_1 &= f_1 \\ s_2 &= f_2 - s/n \\ f_1/f_2 &= \sqrt{a} \\ a &= \frac{n^2 n_g p}{2\lambda_0} \sqrt{\frac{\lambda_0^2}{n_g^2 p^2 \tan^4 \gamma} + \frac{4}{n^2} - \frac{n^2}{2 \tan^2 \gamma}}\end{aligned}$$

Furthermore, the parameter a is linked to the required magnification M of the 4f-configuration:

$$M = \sqrt{\frac{1}{a}} \quad (2.12)$$

In order to reach optimal efficiency and separable incident and diffracted beams, blazed gratings with incident angle θ_i near the Littrow angle θ_L are used:

$$\sin(\theta_L) = \frac{\lambda_0}{2p}$$

The results for the required incident angle as a function of the grating period p are displayed in fig. 2.7(a). Furthermore, the choice of p implies a certain magnification, following eq. (2.12), as shown in fig. 2.7(b). To withstand high pump fluences, gratings manufactured for chirped pulse amplification are ideal for THz generation. From the available components, we decided for a gold-coated grating with a period of 1200 lines/mm (*Horiba*), which offers an efficiency over 93 % for TM-polarization at 1060 nm incident

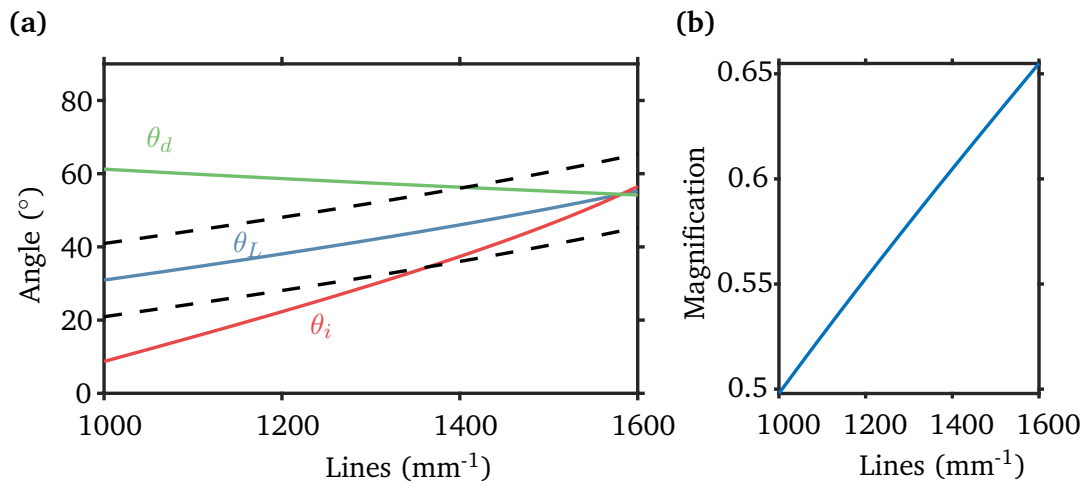


Fig. 2.7: Requirements to the tilted pulse front setup. (a) Required incident angle and resulting diffracted angle as a function of the grating period. For highest efficiency, θ_i close to the Littrow angle are favorable. The dashed lines indicate a deviation of $\pm 10^\circ$ from θ_L . (b) Choosing a grating requires a specific magnification for the imaging unit.

at the required angle $\theta_i = 22.3^\circ$. Hence, the telescope consists of two 50.4 mm-achromats (Thorlabs) with $f_1 = 150$ mm and $f_2 = 80$ mm, providing a magnification $M_{\text{exp}} = 0.53$ close to the optimal $M = 0.55$.

2.5 Electro-optical sampling of terahertz pulses with absolute electric field strength calibration

In this work, terahertz waveforms are routinely characterized by the electro-optical sampling (EOS) technique [53], which allows to directly sample the electric field evolution in the time-domain, thus, detects amplitude and phase of the electric field. Recently, this technique has also been applied successfully to near-infrared waveforms [54].

Pockels effect

The linear electro-optic effect or Pockels effect describes the relation between a linear change in refractive index as a function of a static electric field and is the base for EOS of ultrafast THz pulses.

The change in refractive index as a function of an electric field $\vec{F} = (F_x, F_y, F_z)$ can be written with the electro-optic tensor r_{ij} as [55]:

$$\Delta \left(\frac{1}{n^2} \right)_i = \sum_{j=1}^3 r_{ij} F_j \quad (2.13)$$

Thereby, the coefficients $\left(\frac{1}{n^2} \right)_i$ arise from the index ellipsoid in general form:

$$\left(\frac{1}{n^2} \right)_1 x^2 + \left(\frac{1}{n^2} \right)_2 y^2 + \left(\frac{1}{n^2} \right)_3 z^2 + 2 \left(\frac{1}{n^2} \right)_4 yz + 2 \left(\frac{1}{n^2} \right)_5 xz + 2 \left(\frac{1}{n^2} \right)_6 xy = 1 \quad (2.14)$$

The electro-optic tensor r_{ij} is material specific, and typically, a lot of tensor entries vanish due to symmetry considerations. In this work, gallium phosphide crystals are used as electro-optic material, and for such zincblende structure crystals ($4\bar{3}m$ class) r_{ij} reduces to [56]:

$$r_{ij} = \begin{bmatrix} 0 & 0 & 0 \\ 0 & 0 & 0 \\ 0 & 0 & 0 \\ r_{41} & 0 & 0 \\ 0 & r_{41} & 0 \\ 0 & 0 & r_{41} \end{bmatrix} \quad (2.15)$$

Hence, the index ellipsoid for a zincblende crystal is deformed by an external electric field \vec{F} following eq. (2.13):

$$\left(\frac{1}{n^2} \right)_1 x^2 + \left(\frac{1}{n^2} \right)_2 y^2 + \left(\frac{1}{n^2} \right)_3 z^2 + 2r_{41} F_x yz + 2r_{41} F_y xz + 2r_{41} F_z xy = 1 \quad (2.16)$$

Linear electric field detection

The changes in the refractive index from eq. (2.16) and, thus, the electric field are experimentally accessible by the measurement of changes in the polarization of a radiation that passes through the electro-optic crystal. We follow the description presented in ref. [57], where the full derivation is given for all upcoming formulas. A more general description of electro-optic detection can be found in refs. [58, 59].

We employ an optical probe beam polarized at 45° with respect to the s-polarized THz beam, that reads out Δn through measurement of its polarization state, see fig. 2.8.

With $\vec{F} = (0, 0, F_{\text{det}})$, the index ellipsoid can be rewritten in the laboratory frame (x', y', z') :

$$x'^2 \underbrace{\left(\frac{1}{n^2} + r_{41} F_{\text{det}} \right)}_{1/n_{x'}^2} + y'^2 \underbrace{\left(\frac{1}{n^2} + r_{41} F_{\text{det}} \right)}_{1/n_{y'}^2} + z'^2 \underbrace{\left(\frac{1}{n^2} \right)}_{1/n_{z'}^2} = 1 \quad (2.17)$$

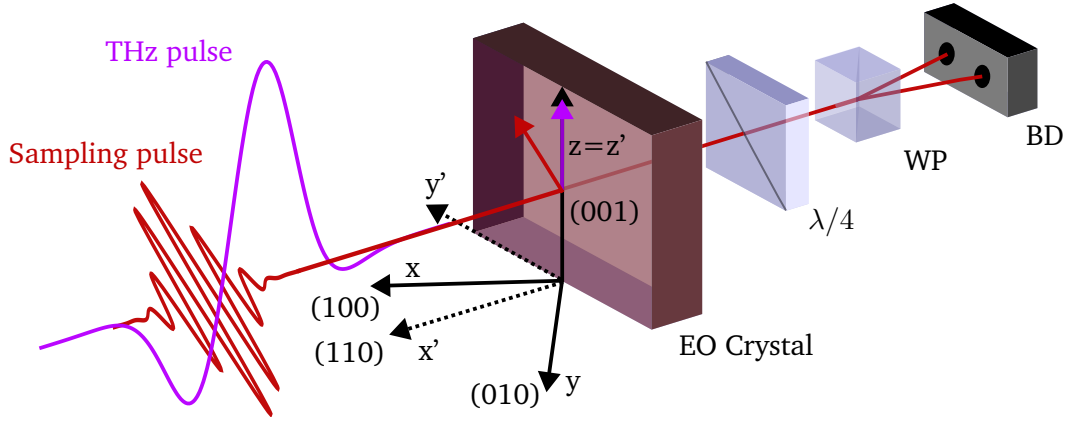


Fig. 2.8: Schematic electro-optical sampling setup. The s-polarized THz beam and the sampling beam with 45° tilted polarization hit the <110> cut zincblende crystal. Notably, the crystal frame (x, y, z) differs from the laboratory frame (x', y', z'). The refractive index changes, and thus, the electric field induced by the Pockels effect is imprinted in the polarization of the sampling beam, which is read out with a pair of balanced photodetector (BD). In particular, the crystal induces elliptical polarization of the sampling beam in the presence of an electric field. The ellipticity is converted in a linear polarization of 45° tilted by $\Delta\varphi/2$ in the quarter wave plate and is measured after splitting up the signal in the y' - and z' -component with a Wollaston prism.

The optical probe beam only has components in y' and z' and thus, the change in refractive index for the two components reads as:

$$\Delta n = n_{y'} - n_{z'} = \frac{n^3}{2} r_{41} F_{\text{det}} \quad (2.18)$$

Taking also into account the amplitude reflection at the surface of the crystal, the phase change $\Delta\varphi$ between x' and y' components for an electro-optic crystal with thickness d is given by:

$$\Delta\varphi = \underbrace{\frac{1}{1 + n_{\text{THz}}}}_s \frac{2\pi n^3 r_{41}}{\lambda_{\text{opt}}} F_{\text{det}} d \quad (2.19)$$

The first part of the equation, s , can be understood as the DC-sensitivity. Experimentally, $\Delta\varphi$ is measured by the difference of the y' and z' intensity component of the probe beam after passing the crystal. Therefore, a quarter-wave plate parallel to the incident probe beam polarization and a Wollaston prism (WP) are used. The differential signal $\Delta I = I_{y'} - I_{z'}$ between the resulting two orthogonal parts of the probe beam is measured with a pair of balanced photodiodes (BD). In particular, ΔI is detected as a voltage signal U_F which corresponds to the sine of the phase rotation $\Delta\varphi$ multiplied with a calibration constant k :

$$U_F = k \sin(\Delta\varphi) \quad (2.20)$$

For small $\Delta\varphi$, the sine can be linearized, leading to a signal linear in the electric field. The calibration constant k can be determined by rotating the quarter-wave plate by an angle $\Delta\theta_{\lambda/4}$ in absence of the external electric field. Here, $\Delta\theta_{\lambda/4}$ denotes the angle between the fast axis of the quarter wave-plate and the z -direction. Finally, the balanced diodes detect a signal $S(\Delta\theta_{\lambda/4})$:

$$S(\Delta\theta_{\lambda/4}) = k \frac{1}{2} \sin(4\Delta\theta_{\lambda/4}) \quad (2.21)$$

Deviations from a pure sinusoidal form typically arise from a misaligned setup, e.g., wrong incident optical polarization or tilted wave-plates. The influence of absorption, phase mismatch and finite sampling pulse length on $\Delta\varphi$ is discussed in detail in ref. [57]. Finally, the detection of absolute electric field strengths is feasible with eqs. (2.19) to (2.21) using a zinblende crystal with defined thickness in the described scheme.

Notably, a two times higher sensitivity can be achieved by aligning optical probe beam and THz pulse polarization parallel to each other and rotating the [001]-axis of the crystal perpendicular to the THz polarization [58].

Electro-optic crystal

The Pockels effect is, such as OR and DFG, a $\chi^{(2)}$ -process, and therefore, the involved beams need to fulfill a phase matching condition: the phase velocity of the THz pulse must be equal to the group velocity of the sampling pulse. In reality, only near-perfect phase matching is possible due to the available crystals. Consequently, the detection bandwidth is also limited by the crystal thickness. Additionally, transversal-optical phonon resonances (TO-PR) in the THz spectrum limit the accessible frequency regime. For example, ZnTe shows a TO-PR at 5.3 THz, GaP at 12.0 THz and GaAs at 8.1 THz [41]. Moreover, the overall signal strength is given on one hand by the crystal thickness, phase matching and THz absorption and on the other hand by the nonlinear coefficient r_{41} , compare eq. (2.19). ZnTe ($r_{41} = 4.04$ pm/V) offers here a four times higher value than GaP ($r_{41} = 0.97$ pm/V) [41]. Parameters for the different crystals are displayed in tab. 2.2. For a sampling wavelength of 1030 nm GaP, for 800 nm ZnTe and for 1550 nm GaAs offer the best phase matching. The detailed frequency resolved detector response is calculated in ref. [41]. In the experiment, we employ a 100 μ m thick GaP crystal along with a sampling wavelength of 1030 nm, that offers, according to ref. [60], a flat frequency response from 0 THz to 6 THz. For extremely high electric fields or thick sampling crystals, over-rotation can occur, limiting the maximum measurable field strength [61].

Tab. 2.2: Overview of different sampling crystals. Group refractive index n_g for three different sampling wavelengths along with the THz refractive index n and THz absorption α . All values taken from [41], beside the values for 1030 nm (GaAs [40], GaP [42], ZnTe [39]).

Crystal	n_g	n/α (cm ⁻¹)				
		0.5 THz	1.0 THz	2.0 THz	4.0 THz	
GaAs	800/1030/1550 nm	4.18/3.99/3.54	3.61/0.03	3.61/0.13	3.62/0.58	3.70/3.54
GaP		3.57/3.33/3.14	3.34/0.82	3.34/0.04	3.35/0.16	3.39/0.78
ZnTe		3.24/2.98/2.81	3.17/0.08	3.18/0.32	3.23/1.60	3.66/22.11

Effect of finite sampling pulse duration

The sampling process can be understood as the convolution of the THz electric field with the sampling pulse intensity in the case of sampling pulses with much larger central frequency ω_0 than spectral bandwidth $\Delta\omega$. Ignoring phase-mismatch, dispersion, and absorption processes, the transfer function $G(\omega_{\text{THz}})$ can be written as the auto-correlation of the sampling field envelope A_{opt} in the frequency domain [62]:

$$G(\omega_{\text{THz}}) = \int_{-\infty}^{+\infty} A_{\text{opt}}^*(\omega - \omega_0) A_{\text{opt}}(\omega - \omega_0 - \omega_{\text{THz}}) d\omega_{\text{THz}} \quad (2.22)$$

This can be rewritten using the convolution theorem and the intensity of the sampling pulse in the time-domain $I(t)$:

$$G(\omega_{\text{THz}}) = \mathcal{F}(I(t)) \quad (2.23)$$

Here, \mathcal{F} denotes the Fourier transform. $|G(\omega_{\text{THz}})|$ is shown in fig. 2.9 as a function of the sampling pulse length.

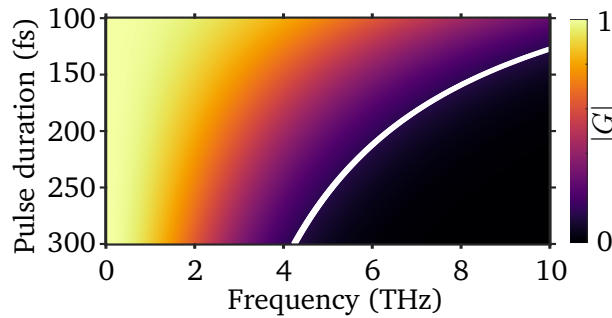


Fig. 2.9: Transfer function $|G|$ for different $1/e^2$ sampling pulse durations. The white line indicates the $1/e^2$ -bandwidth of the detection, assuming a Gaussian-shaped intensity.

2.6 Experimental realization of generation and detection of strong THz pulses

After deriving optimal parameters for the tilted pulse front scheme and presenting a platform for calibrated field measurements, the full experimental setup for THz generation and detection is given in fig. 2.10. Detailed information is given in the caption.

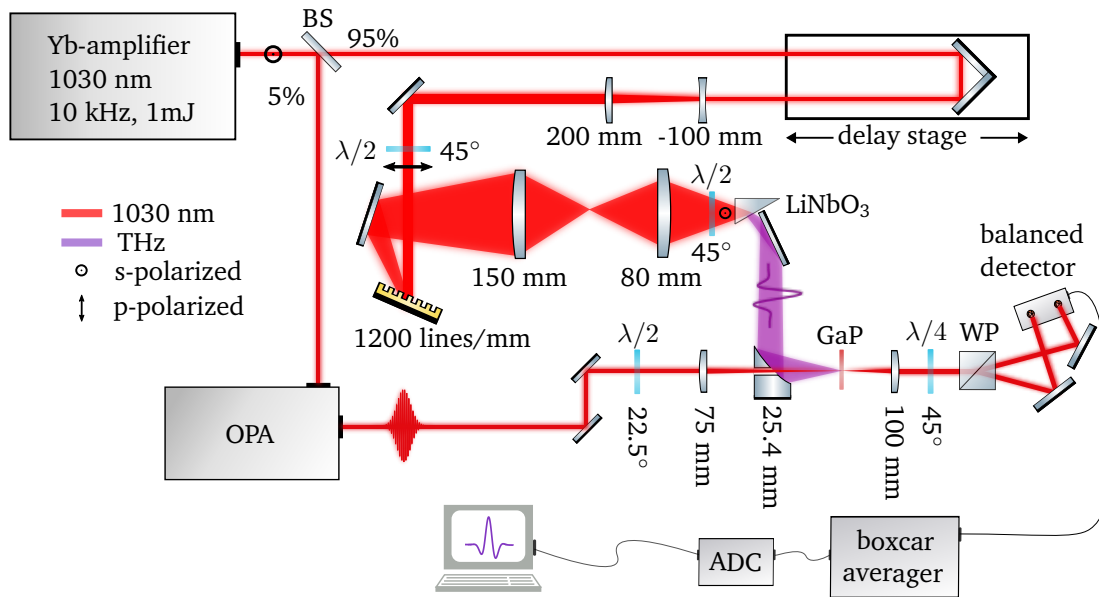


Fig. 2.10: Experimental setup for generation and detection of strong terahertz pulses. The pump pulses from the amplifier system are guided to a mechanical delay stage with a silver-coated retro-reflector, enabling variable temporal delay between the pump pulses and the OPA pulses. The pump beam is enlarged by a Galilean telescope to a $1/e^2$ -width of 1 cm to reduce the peak intensity on the grating and in the crystal. Before hitting the gold-coated grating, the polarization is rotated to ensure maximum diffraction efficiency. The spot on the grating is then imaged inside the MgO:LiNbO₃ crystal (63° wedge angle) by a telescope, consisting of two 2-inch achromats. The polarization is aligned to the z-axis of the crystal with a half-wave plate. The terahertz radiation exits the crystal perpendicular to its surface and is guided to a 90-degree, 1-inch off-axis parabolic mirror, focusing the beam in the sampling crystal. The OPA is operated at the pump wavelength 1030 nm and is focused in the GaP crystal through a hole in the parabolic mirror. The balanced detector (PDB 210A/M, Thorlabs) delivers short voltage pulses, that hinder direct detection with e.g. a lock-in-amplifier due to the relatively low repetition rate of the laser system. Therefore, we employ a boxcar averager (SR250, Stanford Instruments), that is synchronized to the laser repetition rate. The device averages only over a (variable) short portion of the input signal, improving the signal-to-noise ratio for low duty-cycle applications. The averaged signal is afterwards measured via an analog-digital converter (ADC) and recorded with a custom LabView program.

2.7 Spatio-temporal characterization of single-cycle terahertz pulses

Calibrated electro-optical sampling

In section 2.5, the calibrated detection of electric field strengths has been derived. The calibration constant k is acquired by the rotation of the quarter-wave plate, following eq. 2.21, yielding a sinusoidal curve as shown in fig. 2.11 using a $100\ \mu\text{m}$ thick $\langle 110 \rangle$ GaP crystal.

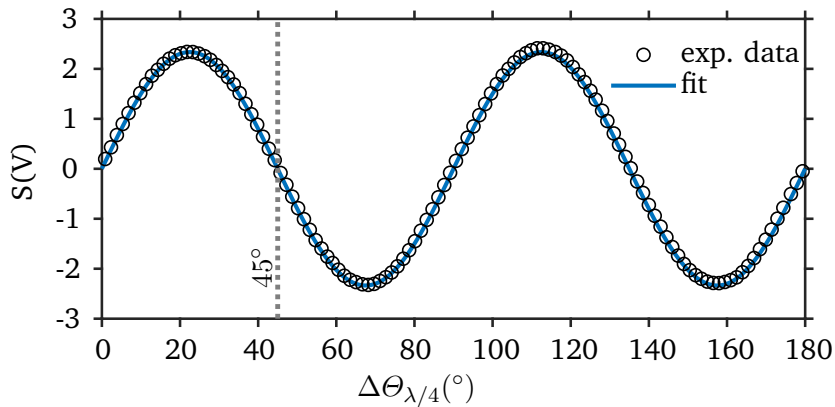


Fig. 2.11: Exemplary calibration of the EOS setup. The rotation of the quarter wave-plate leads to a strict sinusoidal behavior for $\Delta I(\Delta\theta_{\lambda/4})$. The calibration factor is determined by fitting eq. 2.21 to $k = 4.67\text{ V}$. A rotation of 180° is not necessary but can show a misaligned setup. For EOS measurement, the quarter-wave plate is set to, e.g., 45° (gray dashed line) to balance the two diodes.

The DC-sensitivity for GaP at a sampling wavelength of $1030\ \text{nm}$ can be calculated to $s = 0.21 \frac{\text{V}}{\text{cm mm}}$ using $r_{41} = 0.88\ \text{pm/V}$, $n_{\text{THz}} = 3.33$ and $n = 3.11$ [42, 63, 64]. However, also slightly higher values for r_{41} can be found in literature, e.g. $r_{41} = 0.97\ \text{pm/V}$ [65], leading to lower absolute fields. Finally, the electric field F_{det} can be measured from the detected voltage U_F using eqs. (2.19) and (2.20):

$$F_{\text{det}} = \frac{\arcsin\left(\frac{U_F}{k}\right)}{sd} \quad (2.24)$$

In the experiment, temporal sampling is achieved by delaying the THz pulse with respect to the optical sampling pulse with a mechanical delay stage. The calibrated sampling trace in fig. 2.12(a), with a temporal stepsize of $27\ \text{fs}$, shows a maximum electric field strength exceeding $400\ \text{kV cm}^{-1}$. The amplitude spectrum in fig. 2.12(b), calculated via Fourier transform, is centered around $1.2\ \text{THz}$ and shows frequencies spanning from $0\ \text{THz}$ to nearly $4\ \text{THz}$.

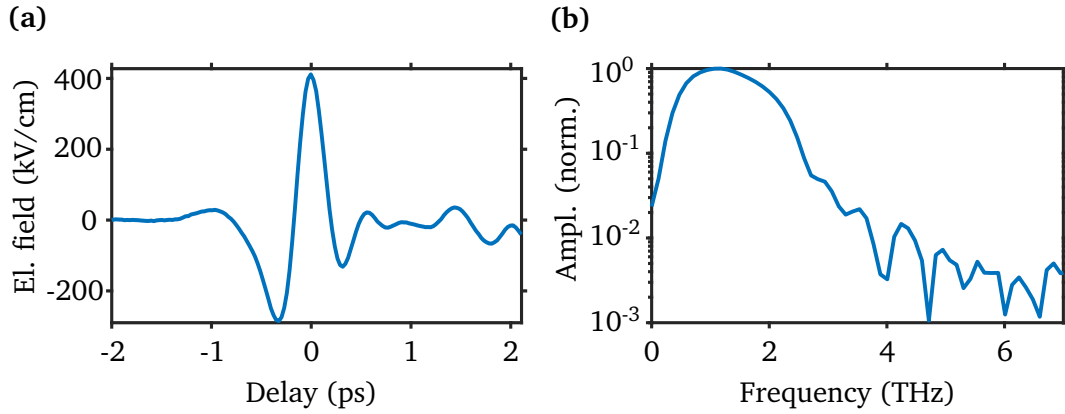


Fig. 2.12: Terahertz waveform and spectrum with calibrated field strength. (a) The THz electric field evolution is measured via EOS using a $\langle 110 \rangle$ GaP crystal with a thickness of $100 \mu\text{m}$. Applying the aforementioned calibration scheme, an electric field of over 400 kV cm^{-1} can be assigned to the peak of the pulse. (b) The corresponding amplitude spectrum centered around 1.2 THz.

Attenuation of terahertz beams by phase matching tuning

The attenuation of THz beams is typically implemented via a pair of wire-grid polarizers or a set of high-resistivity silicon (HR-Si) wafers [66]. In this work, we also control the THz field strength with the polarization of the pump beam. Therefore, we rotate the half-wave plate in front of the LiNbO₃ crystal by an angle $\Delta\theta_{\lambda/2}$, reducing the intensity polarized parallel to the $\langle 001 \rangle$ -axis, leading to the set of sampling traces in fig. 2.13(a). We extract the maximum and minimum field strengths, as displayed in fig. 2.13(b).

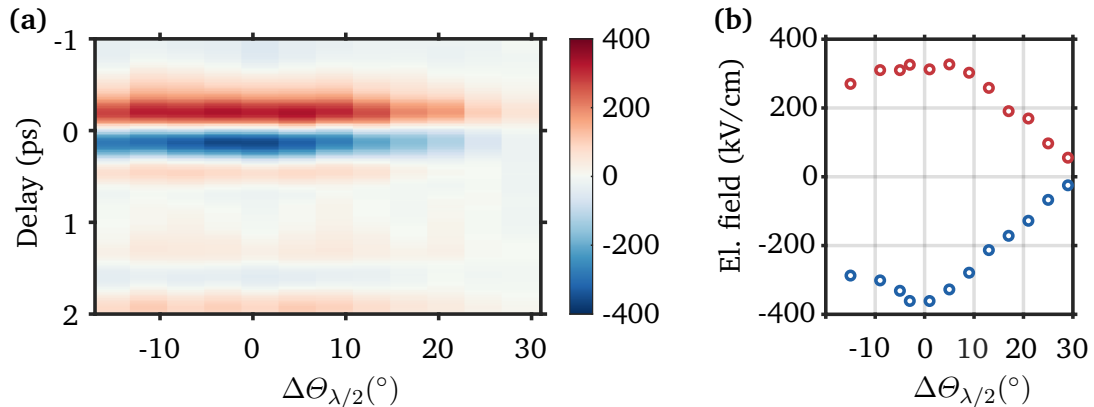


Fig. 2.13: THz attenuation via pump pulse rotation. (a) Electro-optical sampling traces for different half-wave plate angles and, thus, different polarization of the pump beam. The temporal position of the peaks was aligned to match each other because the waveforms are slightly different for different pump beam polarizations. Notably, also the waveforms changes slightly, especially for angles far away from optimum. (b) The extracted peak maxima (red) and minima (blue) are varied continuously with the half-wave plate.

Imaging and detection of terahertz beams

Detection of terahertz radiation is not feasible with, e.g., conventional silicon-based devices, as the photon energy is much smaller than the semiconductor bandgap. Hence, different devices and tools were employed throughout the thesis to facilitate the handling of the THz beam.

For qualitative detection of the radiation, we employed detectors based on the pyro-electric effect (QE8SP-B-MT, *Gentec* and L11 series, *Laser Components*). The absolute THz pulse energy can only be estimated to values around $1\ \mu\text{J}$ or below, as the exact calibration of the detection was not given by the manufacturer. That corresponds roughly to an energy efficiency of the THz generation in the order of 1×10^{-3} or below. For the visualization of the THz beam, we used detector cards built for mid-infrared radiation (e.g. VRC6H, *Thorlabs*) that change the color depending on the deposited heat of the THz beam using a layer of thermo-chrome liquid crystals. This works especially well for strongly focused THz beams, as the minimum detectable power density is specified to $0.05\ \text{mW}/\text{mm}^2$. A photograph of the focused THz beam on the liquid crystal card aligned with an optical beam is displayed in fig. 2.14.

We also determine the THz beam profile with a cost-efficient micro-bolometer camera (Thermal Pro, *SEEK*), that is typically used for thermal imaging. In ref. [67] this particular camera is compared to a dedicated THz camera, showing comparable results in THz beam profiling. We removed the lens in front of the camera and directly exposed the $(3.84 \times 2.88)\text{mm}^2$ sized chip. The THz beam at the output of the crystal, optimized for the highest energy output, shows an irregular shape, see fig. 2.15(a), hindering optimal focusing. After slight adjustments of the LiNbO_3 position perpendicular to the pump beam direction, a nearly-perfect Gaussian beam shape has been established at slightly lower output energy, as shown in fig. 2.15(b).

The beam size in the focal plane of the parabolic mirror is essential for the experiments in this work, as it defines, along with the THz pulse energy, the electric field strength. An optimized THz focus is displayed in fig. 2.16, revealing a $1/e^2$ -beam diameter of $350\ \mu\text{m}$ to $400\ \mu\text{m}$. The theoretical waist diameter can only be estimated as the beam properties on the parabolic mirror are unknown. However, by propagating a Gaussian beam from the exit of the generation crystal to the focus of the parabolic mirror, the beam diameter can be estimated to $w_{\text{theo}} = 320\ \mu\text{m}$, details see fig. 2.16(b).

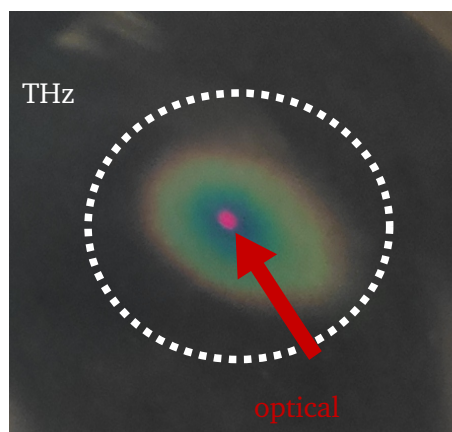


Fig. 2.14: Terahertz detector card. The deposited heat of the focused THz beam changes the color of the thermochromic liquid crystal.

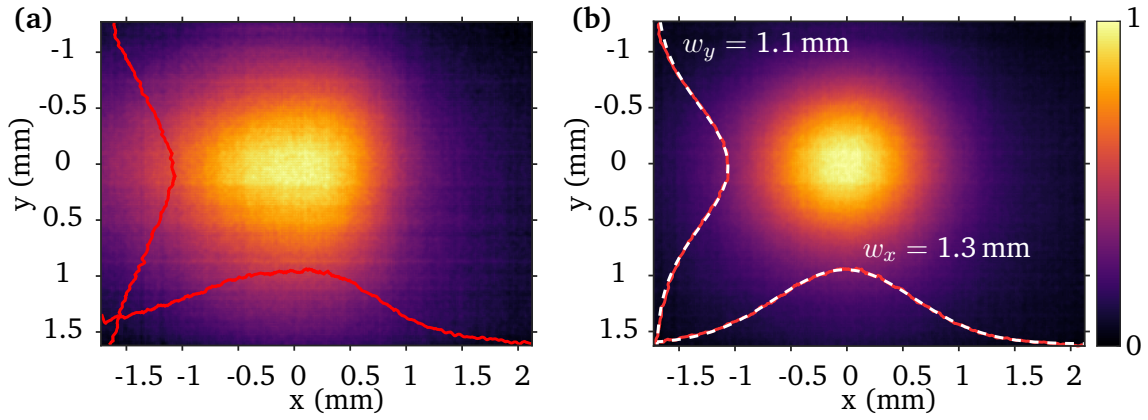


Fig. 2.15: Terahertz beam profiles close to the surface of the LiNbO₃ crystal. (a) For the highest energy output, the THz beam profile shows a strong asymmetric beam profile, as apparent from the cut lines through maximum intensity (red). (b) The optimized THz output beam shape, along with cut lines (red) through the peak intensity, evidence a Gaussian beam shape. The fitted 1d-Gaussians (white, dashed) show slightly different $1/e^2$ -diameters w in x- and y-direction.

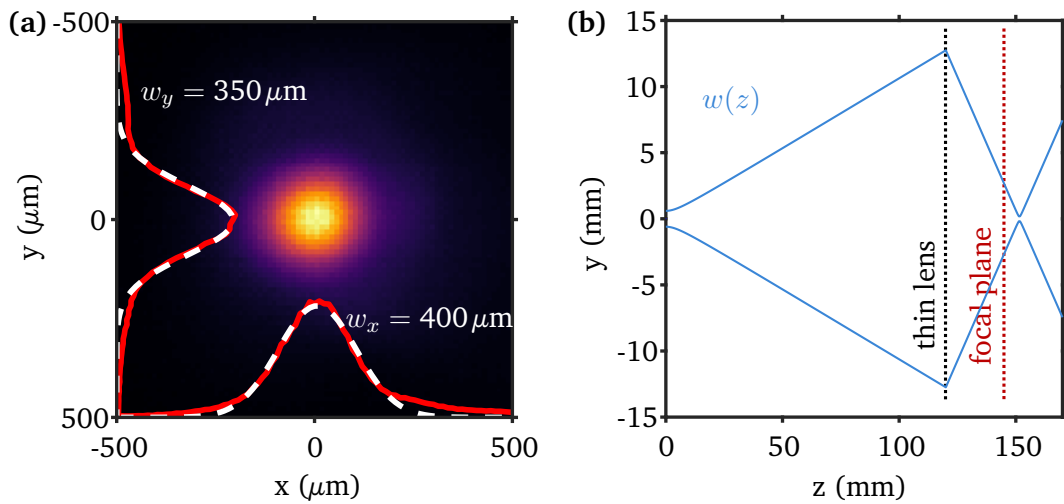


Fig. 2.16: Focused terahertz pulse. (a) The THz beam profile at the focus of the parabolic mirror shows a close-to-Gaussian shape. Two slightly different beam sizes are determined from cuts (red) through the peak intensity via 1d-Gaussians (white, dashed). (b) A Gaussian beam with a frequency of 1.2 THz and a diameter of $w = 1.2$ mm propagates 120 mm and is then focused by a thin lens (black, dotted) with a focal length of 25 mm to a focus of approximately $w_{\text{theo}} = 320 \mu\text{m}$. Notably, the strongly divergent beam hits the lens under an angle. This also has implications on the focus position, which is approximately 32 mm away from the focusing element, thus, shifted about 7 mm than expected from the focal length (red, dotted) – this effect also has been observed in the experiment. For the calculations, we use the formulas given in ref. [68].

Gouy-phase of focused terahertz beams

A focused Gaussian beam undergoes a carrier-envelope phase (CEP) shift of π throughout the focus. This so-called Gouy-phase shift φ_G can be calculated for a focused monochromatic Gaussian beam with Rayleigh length z_R propagating in z -direction [69]:

$$\varphi_G = -\arctan\left(\frac{z}{z_R}\right) \quad (2.25)$$

Here, $z = 0$ indicates the position of the focus. The Gouy-phase shift is hidden to intensity-based techniques, as the envelope of the electric field is not affected by the CEP. Therefore, we detect the electric fields with EOS at different positions z across the focus, as displayed in fig. 2.17. This allows us to estimate the Rayleigh range z_R by fitting the formula from above, yielding $z_R = (0.9 \pm 0.1)$ mm - the procedure is described in the caption of fig. 2.17. Starting from the beam-diameter at the focus position w and the wavelength λ , we can calculate the theoretical Rayleigh range [69]:

$$z_R = \frac{\pi (w/2)^2}{\lambda} \quad (2.26)$$

Using the center-of-mass of the spectrum at $z = 0$, $\lambda = 300 \mu\text{m}$, and a measured $1/e^2$ beam diameter of $w \approx 530 \mu\text{m}$, we calculate $z_R \approx 0.7$ mm, slightly below the derived value. Deviations could arise from the non-monochromatic THz radiation as the Gouy-phase is treated for a monochromatic light source and for broadband radiation deviations from the arctan-law have been shown [70, 71]. Additionally, we observed that the spectrum also changes far away from the focus position. Based on the CEP shift, we will derive in section 4.5 a method to detect polarities from rectified waveforms.

Estimation of terahertz pulse energy

We can estimate the photon efficiency of the THz conversion process by studying the depletion of the pump beam and the resulting change in the spectrum of the Pharos $S(\lambda)$ at the output and after the LiNbO₃ crystal, as described in ref. [72]. Therefore, we calculate the first momenta $\bar{\lambda}$ of the spectra before ($\bar{\lambda}_0$) and after the THz generation process ($\bar{\lambda}_{\text{THz}}$):

$$\bar{\lambda} = \frac{\int \lambda S(\lambda) d\lambda}{\int S(\lambda) d\lambda} \quad (2.27)$$

The two spectra are shown in fig. 2.18, yielding a difference $\Delta\bar{\lambda} = 4.1$ nm.

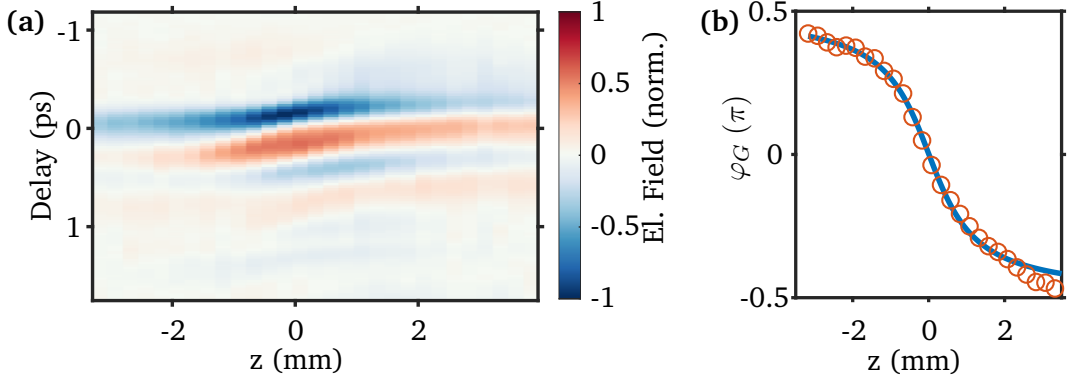


Fig. 2.17: Gouy-phase shift in EOS traces. (a) Electro-optical sampling traces for different positions across the THz focus. Here, negative z -values are closer to the parabolic mirror. The Gouy-phase shift is visible in the temporal shift of minima and maxima due to a shift in the CEP. In other words, the electric field flips completely through the focus. (b) We derived the CEP by Fourier-transforming the curves from (a) and weighting their phase with the pulse spectrum. The extracted data points (red) are fitted (blue) with eq. 2.25, yielding $z_R = (0.9 \pm 0.1)$ mm.

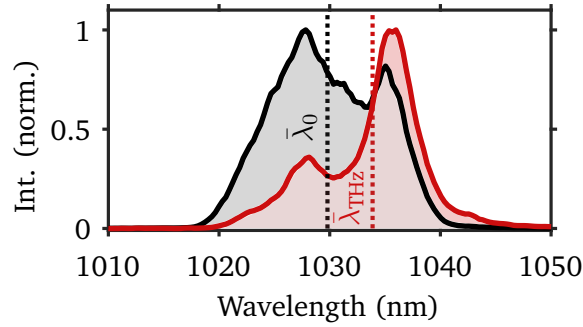


Fig. 2.18: Pump laser spectrum before and after THz generation. The Pharos spectrum is shifted and shaped by depletion in the THz generation process by about 4 nm from the black to the red curve.

For a photon efficiency of 100 %, the theoretical wavelength shift $\Delta\bar{\lambda}_{\text{theo}}$ can be calculated using the first moment of the THz frequency spectrum shown in fig. 2.12 $\bar{\nu}_{\text{THz}} = 1.34$ THz as frequency shift $\Delta\nu$ and the optical pump frequency $\nu = 291$ THz:

$$\Delta\bar{\lambda}_{\text{theo}} = \frac{c}{\nu^2} \Delta\nu = 4.8 \text{ nm} \quad (2.28)$$

Hence, the photon conversion efficiency can be estimated to $\eta = 85\%$. Finally, the terahertz pulse energy $E_{\text{THz}}^{\text{pulse}}$ can be calculated:

$$E_{\text{THz}}^{\text{pulse}} = h\nu_{\text{THz}} \frac{E_{\text{NIR}}^{\text{pulse}}}{h\nu} \eta = 3.2 \mu\text{J} \quad (2.29)$$

Here, we used an estimated optical pump pulse energy of $E_{\text{NIR}}^{\text{pulse}} = 800 \mu\text{J}$ at the crystal position, taking into account losses at the grating and the silver mirrors.

However, $E_{\text{THz}}^{\text{pulse}}$ estimates the pulse energy inside the THz crystal, whereas due to the high refractive index ($n_{\text{THz}}^{\text{LiNbO}_3} = 4.96$) only $\approx 55\%$ of the THz energy can leave the crystal. Additionally, the crystal shows a high THz absorption coefficient of $\alpha \approx 17 \text{ cm}^{-1}$, leading to further attenuation depending on the unknown propagation length inside the crystal. In ref. [72], a propagation length of 1 mm has been assumed without further explanation, leading to an absorption loss of roughly 80%. Finally, taking into account absorption and reflection losses inside the crystal, the pulse energy outside the crystal can be estimated to:

$$E_{\text{THz}}^{\text{out}} = 0.35 \mu\text{J} \quad (2.30)$$

This corresponds to an energy efficiency of the whole setup of approximately 0.035%. Ref. [72] reports an efficiency of 0.025% for 400 μJ pump pulses at 1035 nm employing a tilted pulse front setup with a single lens and a LiNbO₃ crystal at room temperature. Another way to estimate the THz pulse energy $E_{\text{THz}}^{\text{pulse}}$ is given by the following formula for a Gaussian-shaped pulse with duration τ , area A_{THz} and peak field strength F [73]:

$$E_{\text{THz}}^{\text{pulse}} = \frac{F^2 \varepsilon_0 c \tau A_{\text{THz}}}{2} \quad (2.31)$$

Using typical values of the setup ($\tau = 1 \text{ ps}$, $F = 400 \text{ kV cm}^{-1}$, $A = 0.13 \text{ mm}^2$) a pulse energy of 0.3 μJ can be calculated. The optical power is then $0.3 \mu\text{J} \times 10 \text{ kHz} = 3 \text{ mW}$.

Temporal overlap of terahertz and optical pulses

The temporal overlap of the THz pulses and the OPA signal pulses can be found by scanning the mechanical delay stage, as the EOS technique provides a large signal at 1030 nm. Later on in this thesis, we also employ probe wavelengths below 650 nm from another OPA interaction where we cannot apply EOS. Therefore, we implement another approach: pump/probe transient absorption of THz radiation in an optically pumped semiconductor such as silicon. In particular, we optically pump a semiconductor substrate, e.g. a HR-Si wafer, above its bandgap and detect changes in the THz transmission to ensure the temporal overlap. The bandgap E_g of silicon is 1.1 eV [74] at 300 K and upon interaction with intense optical pulses free charge carriers are generated, that reduce the THz transmission [75]. We use OPA pulses at 480 nm wavelength with a power of about 2 mW that are loosely focused on the semiconductor samples. The transmitted THz power is detected as a function of the temporal delay between optical and THz pulses using a pyroelectric detector, a mechanical delay stage and a lock-in amplifier. Therefore, the optical pump beam is modulated using a mechanical chopper wheel.

The resulting change in the transmitted energy is presented in fig. 2.19 for a HR-Si and an undoped GaAs ($E_g = 1.4 \text{ eV}$ at 300 K [74]) wafer, showing a decrease of the transmittance,

when the optical beam arrives before the THz beam (delay > 0). The change in transmittance for negative delays is attributed to reflections of the THz beam in the semiconductor wafer. Due to the long charge carrier lifetime in HR-Si up to milliseconds [76], a recovery in the transmittance is not observable in the time window of the measurement. In contrast, the GaAs sample shows a recovery, enabling the measurement of charge carrier lifetimes, see, e.g., ref. [77].

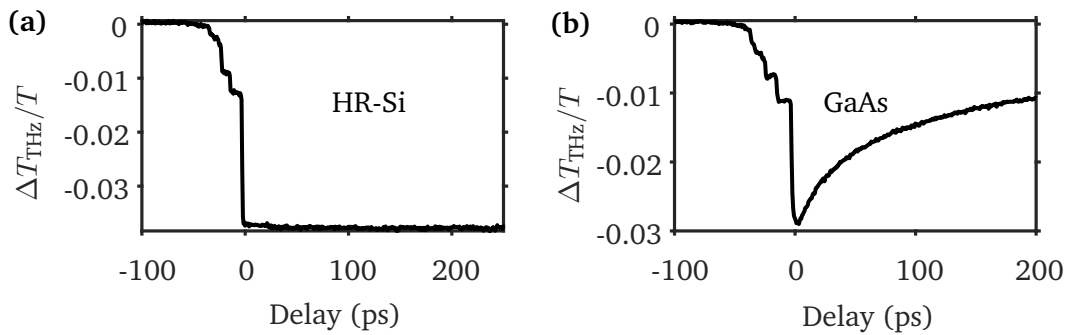


Fig. 2.19: Optical-pump THz-probe measurement in semiconductors (a) The transmission ΔT_{THz} of the THz beam through an optically-pumped silicon wafer is reduced by several percent, offering a way to determine the temporal overlap of THz and optical beam. (b) The recombination of photo-excited carriers in GaAs can be observed in the recovery of the THz transmission.

Theory and detection of the quantum-confined Stark-effect in strong electric fields

3.1 Electric field enhancement in gold microstructures

The employed tilted pulse front technique generates terahertz pulses with high field strengths up to 400 kV/cm, that we use in this work to change the optical properties of quantum dots. In particular, the change in absorption of the nanocrystals depends approximately quadratically on the electric field, as we demonstrate in our experiments. Therefore, we employ gold microstructures fabricated with photolithography to increase the THz electric fields by up to an order of magnitude and thus amplify the effect. In detail, the near-field of THz radiation impinging metallic microstructures is locally enhanced and also spectrally shaped by e.g. structural resonances. Here, we provide a short overview of the fabrication, enhancement factors, and time-transient simulations of the near-fields in gold microstructures in the THz regime.

Dielectric function of gold in the THz spectral region

Fundamentally, the reaction of a metal to an electric field is given by its relative dielectric function ε_r [78], which consists of a real part ε' and a complex part ε'' . In particular, it is linked to the complex refractive index n [79]:

$$\varepsilon_r = \varepsilon' + i\varepsilon'' = n^2 = (n' + i\kappa)^2 \quad (3.1)$$

In contrast to ε_r of gold in the visible spectral region, where interband transitions play a role, the permittivity in the THz range is sufficiently well described by a Drude model. Therefore, ε_r as a function of the angular frequency ω is determined by a plasma frequency ω_p and a relaxation time τ [79]:

$$\varepsilon_r = \underbrace{\left(1 - \frac{\omega_p^2}{\omega^2 + \tau^{-2}}\right)}_{\varepsilon'} + i \underbrace{\left(\frac{1}{\omega\tau} \frac{\omega_p^2}{\omega^2 + \tau^{-2}}\right)}_{\varepsilon''} \quad (3.2)$$

The dielectric function of gold is studied in various works, see e.g. ref. [80], but only few data exist in the far-infrared spectral region. In particular, ε_r in the THz regime is measured and evaluated in refs. [81, 82]. From their results, the plasma frequency is determined to $\hbar\omega_p \approx 9$ eV and the relaxation time to $\tau \approx 24$ fs. The resulting ε' and ε'' are displayed in fig. 3.1 along with the data from ref. [82]. For the Drude model, the intersection point of ε' and ε'' can be found from $\frac{1}{2\pi\tau} \approx 6.4$ THz, above which $-\varepsilon'$ is larger than ε'' . This leads to fundamental differences in the interaction of gold with far-infrared radiation compared to optical frequencies. For example, there exist no bound solutions for surface plasmon polaritons below 6.4 THz due to $\varepsilon'' > -\varepsilon'$ [78]. This region is also referred to as the conduction region in contrast to the plasmonic region where $\varepsilon'' < -\varepsilon'$ [83].

Furthermore, the complex conductivity $\sigma = \sigma' + \sigma''$ can also be computed from the Drude parameters ω_p and τ [79]:

$$\sigma(\omega) = \left(\frac{\omega_p^2 \tau \varepsilon_0}{1 + \omega^2 \tau^2} \right) + i \left(\frac{\omega_p^2 \tau \varepsilon_0 \omega \tau}{1 + \omega^2 \tau^2} \right) \quad (3.3)$$

σ' is significantly larger than σ'' in the region around 1 THz and σ' approaches the DC conductivity of gold $\sigma_{DC} \approx 4 \times 10^7 \Omega^{-1} \text{m}^{-1}$ for small frequencies [74], as evident in fig. 3.1(b). This low-frequency part of the conductivity ($\omega\tau \ll 1$) is also called the Hagen-Rubens regime. There, the skin-depth δ_0 , describing the metal film thickness where the electric field drops to $1/e$, can be estimated using the DC conductivity [79]:

$$\delta_0 = \sqrt{\frac{2c^2 \varepsilon_0}{\omega \sigma_{DC}}} \quad (3.4)$$

The resulting skin depth as a function of the frequency is shown in fig. 3.1(c,d) along with the transmitted electric field ratio for different frequencies and thicknesses. In the experiments, gold thicknesses between 100 and 150 nm have been employed, resulting in a transmission between 30 % and 15 % at 1 THz.

Fabrication of gold microstructures via photolithography

The investigated gold microstructures are manufactured using photolithography, and the fabrication has been carried out by Tobias Lauster, Nelson Pech-May, and Stefan Rettinger (Physical Chemistry I, University of Bayreuth). In short, a soda-lime glass slide is coated with a lift-off photoresist that is subsequently baked. In the next step, a positive photoresist is applied using spin-coating and also baked. Then, the structure of interest is written in the resist by scanning the sample in a focused ultraviolet (UV) beam using a direct-write lithography system (ML3 Baby Plus, *Durham Magneto Optics*).

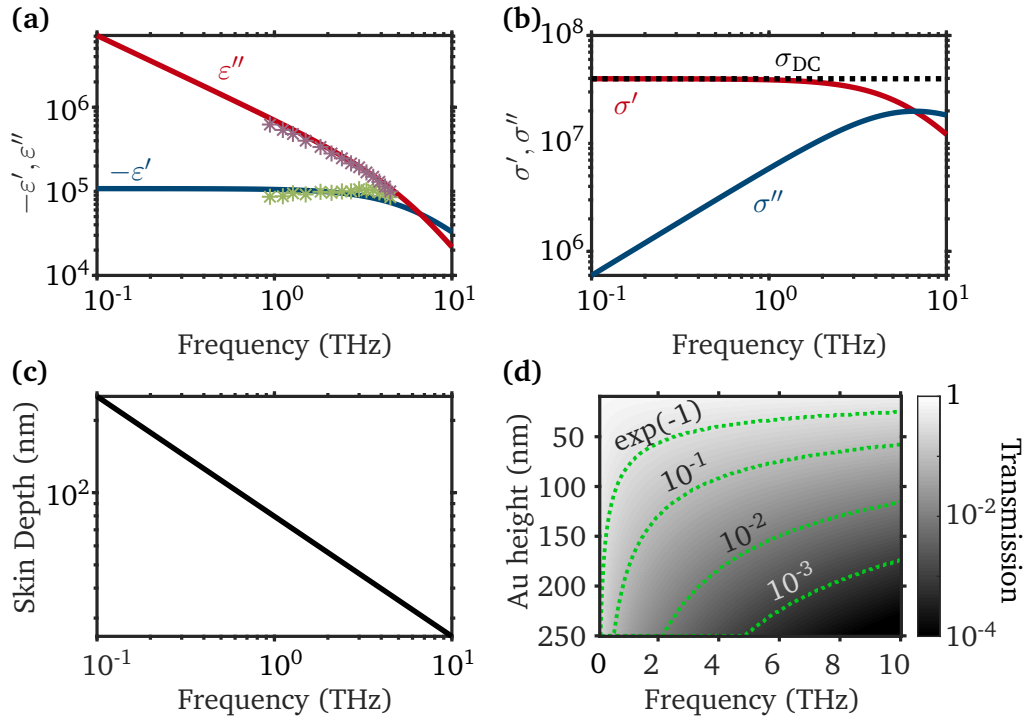


Fig. 3.1: Dielectric function, conductivity and skin depth for gold from 0.1 to 10 THz. (a) The calculated permittivity ϵ' and ϵ'' for gold using the Drude-Sommerfeld-theory for $\hbar\omega_p \approx 9$ eV and $\tau \approx 24$ fs along with derived data points from ref. [82]. The plasma frequency lies in the ultraviolet spectral range at much higher energies. (b) The components of the complex conductivity as a function of the frequency. The real part σ' is nearly constant for low frequencies and approaches σ_{DC} . (c) The calculated skin-depth δ_0 using the DC conductivity increases for lower frequencies. At 1 THz, the skin depth has a value of $\delta_0 \approx 80$ nm. (d) Transmission of the electric field through a gold film for different heights and frequencies. The green lines indicate the parameters for a fixed transmission.

The minimum feature size is specified to $1 \mu\text{m}$. The resist is developed and removed from the areas where it has been exposed to UV light. Afterwards, the surface of the sample is covered with ~ 2 nm of chromium as an adhesive layer and 100-150 nm of gold by physical vapor deposition. Finally, the residual photoresist is removed and, thus, also the metal layer on top of it is removed, yielding the intended gold microstructure. The procedure is illustrated briefly in fig. 3.2.

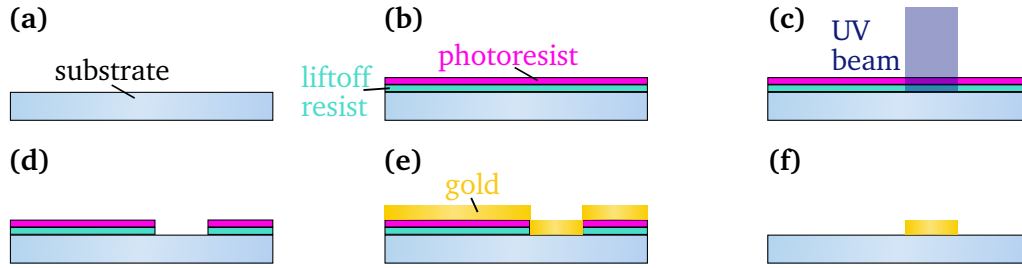


Fig. 3.2: Double-layer lift-off photolithography. (a,b) A lift-off (cyan) and a positive photoresist (magenta) are spin coated and baked on a glass slide (blue). (c) Focused, blue radiation writes the structure in the resists by moving the substrate with a mechanical stage. (d) The UV-exposed areas are removed in the development step. (e) Chromium (not shown) and gold are deposited on the sample. (f) The undeveloped resist with the metal layers is removed and the desired gold structure remains.

Static electric fields in a plate capacitor

The most common way to generate an electric field is realized by metallic plate capacitors filled with a dielectric. In our experiments, we use planar gold capacitors fabricated by optical lithography. Therefore, we will, in short, discuss the strength and the spatial distribution of the electric fields inside such a device. The electric field F between two parallel plates separated by a distance d with a constant potential difference U is given by [84]:

$$F = \frac{U}{d} \quad (3.5)$$

The above equation also holds true independently of a homogeneous dielectric when the potential difference is kept constant. In fig. 3.3, we present the electrostatic field inside two plate capacitors with different dimensions calculated with a finite-element solver (COMSOL Multiphysics v. 5.6). For a small metal thickness compared to the gap size, the electric field is inhomogeneously distributed in the gap, leading to much higher peak fields than in the opposite case, where a more homogeneous behavior is observable. However, the mean electric field is the same in both cases, according to eq. 3.5.

Experimentally, the maximum electric field that can be generated with this technique is limited by the dielectric strength of the dielectric and strongly affected by the electrode geometry. For air, values between 4 kV cm^{-1} and 30 kV cm^{-1} can be found [85]. In the experiment, however, the gap is not filled with air only but also with semiconductor quantum dots. Ref. [86] reports a maximum electric field of 400 kV cm^{-1} for gap dimensions comparable to our geometry.

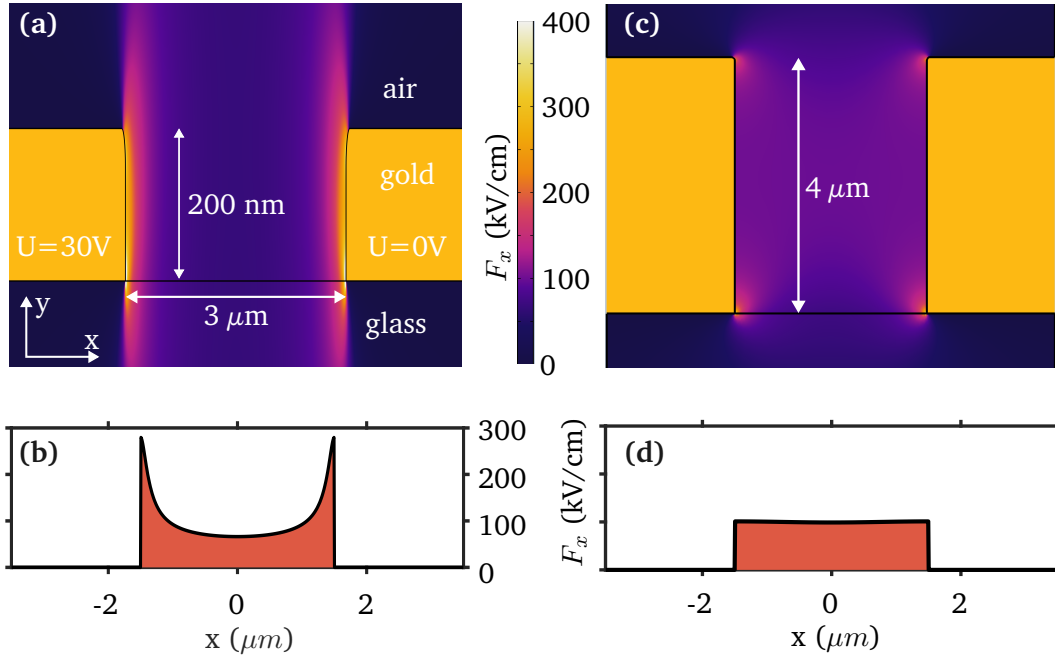


Fig. 3.3: Electric field in plate capacitors with different heights. (a) The x-component of the electric field in a plate capacitor with a gold height of 200 nm, comparable to the value used in the photolithography process, shows a much higher electric field close to the gold edges than expected from eq. 3.5, yielding $F=100 \text{ kV cm}^{-1}$. (b) This is also visible in the cut line through the center of the capacitor, showing an u-shape. Still, the mean electric field value is exact 100 kV cm^{-1} . (c) A plate capacitor with the same gap size but a much higher gold thickness shows a nearly constant electric field inside, besides effects at the edges of the structure. (d) Therefore, the cut line through the center shows a quasi-constant electric field inside.

Field-enhancement in a periodic slit array

A periodic array of gold bars, like sketched in fig. 3.4, with a periodicity p , a height h , and a gap size of g , offers a non-resonant enhancement of electric fields with a wavelength of λ for $p, h < \lambda$. We define the enhancement factor FE as the ratio of near-field F_{nf} and incident field F_{inc} :

$$FE = \frac{F_{\text{nf}}}{F_{\text{inc}}} \quad (3.6)$$

In the case of a free-standing gold structure, the quasi-static enhancement factor FE_s for an incident field polarized perpendicular to the gaps is derived in ref. [87] treating the gold as a perfect electric conductor to:

$$FE_s = \frac{p}{g} \quad (3.7)$$

Therefore, the gap structure can be understood as a funnel for the energy of the incident field. The dependency of the enhancement with respect to the wavelength λ is governed mostly by the grating period. For a single slit, corresponding to $p = \infty$, the enhancement is

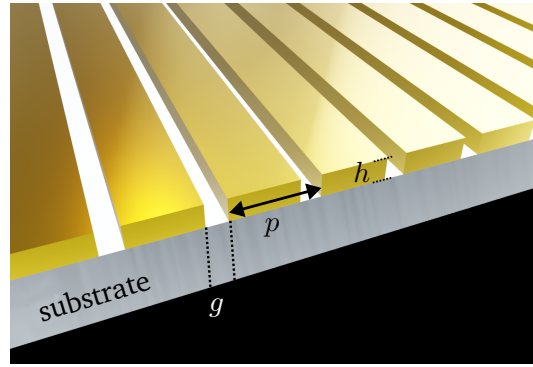


Fig. 3.4: Geometry of a periodic slit array. The enhancement structure is defined by its periodicity p , height of the gold h and the gap size g . For perpendicular polarization of the incident electric field to the gaps, the field enhancement is maximized.

proportional to the wavelength, $FE \propto \lambda$, because the gap appears relatively "smaller" for longer wavelengths. For increasingly smaller periods, the enhancement for the longer wavelengths follows increasingly the quasi-static factor [87].

Considering the substrate with a refractive index n_{sub} , the field enhancement is lowered as the effective refractive index in the typically sub-wavelength gap is increased, see e.g. ref. [88].

Time-dependent simulation of electric field distributions

We use a finite-element solver (COMSOL Multiphysics v. 5.6) to investigate the 2d/3d electric near-fields of gold antennas in the time-domain. In particular, the software solves the following wave equation for the magnetic vector potential \mathbf{A} [89]:

$$\mu_0 \sigma \frac{\partial \mathbf{A}}{\partial t} + \mu_0 \epsilon_0 \frac{\partial}{\partial t} \left(\epsilon_r \frac{\partial \mathbf{A}}{\partial t} \right) + \nabla \times \left(\mu_r^{-1} \nabla \times \mathbf{A} \right) = 0 \quad (3.8)$$

Here, μ_0 denotes the vacuum magnetic permeability, σ the electric conductivity, ϵ_0 the permittivity, μ_r the relative magnetic permeability and ϵ_r the relative permittivity. The simulated volume is enclosed by planes with different boundary conditions. In the experiment, the antennas are positioned in the focus of the THz beam. Since the curvature of the wavefront at the focal point is zero, the THz beam is approximated in the simulation by a plane wave. The polarized radiation is coupled in and out of the geometry via a scattering boundary condition (SBC). In particular, either a measured THz waveform or a pre-defined electric field pulse $F_{\text{THz}}(t)$ is used. An incident electric field reads as:

$$F_{\text{THz}}(t) = F_0 \cos(\omega_0 t + \phi_s) \exp\left(-4 \ln(2) (t - t_0)^2 / \Delta t^2\right) \quad (3.9)$$

Here, F_0 denotes the amplitude, ω_0 is the central frequency of the pulse, and ϕ_s a shift in the carrier-envelope phase. The Gaussian envelope is defined by the temporal shift t_0 and the full-width at half-maximum (FWHM) pulse duration Δt . The polarization and the propagation direction are defined in the software. According to the THz polarization, the boundary conditions parallel to the propagation direction are chosen in the 3d-case as perfect electric conductor (PEC) and perfect magnetic conductor (PMC), respectively, see fig. 3.5. The surfaces of the gold microstructures are approximated as perfect electric conductors and in the 3d-case additionally as thin layers.

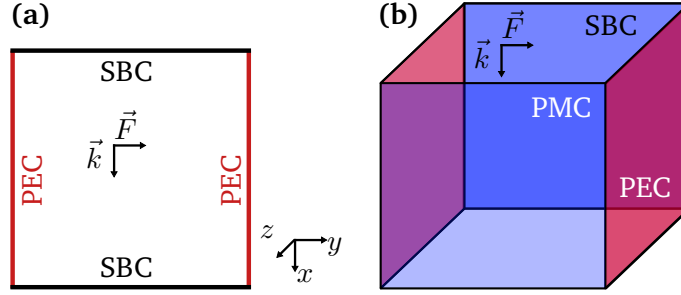


Fig. 3.5: Boundary conditions for simulations in 2d and 3d (a) A plane wave with wavevector \vec{k} is coupled in by the top SBC and propagates in the x-direction with a linear polarization in y-direction. Therefore, the boundaries perpendicular to the propagation direction are perfect electric conductors. In the case of a periodic structure, they can be replaced by periodic boundary conditions. The wave is coupled out of the simulation region with another SBC. (b) In 3d, perfect magnetic boundary conditions (blue) are used in addition to the PEC (blue).

The simulation software discretizes the space in a mesh consisting of small elements (2d: triangles, 3d: tetrahedrons) adapted to the structure of interest. The maximal mesh element size s_{\max} needs to be defined appropriately for the structure, e.g., thin layers. For propagation in free space, a good start point is given by the highest frequency f_{\max} that needs to be resolved and a factor $N \approx 5 - 10$ [90]:

$$s_{\max} = \frac{c}{f_{\max}N} \quad (3.10)$$

Here, c denotes the speed of light. In the case of $N = 10$, the largest mesh element will be ten times smaller than the smallest wavelength. Besides the choice of the mesh size, also the time step Δt in which the solution is calculated needs to be specified. The relation between spatial and temporal discretization is given by the so-called Courant-Friedrichs-Lewy number CFL , which is the proportion of a mesh element of size s_{\max} that is passed by a wave with speed c in the timestep Δt [90]:

$$\Delta t = \frac{CFL}{f_{\max}N} = \frac{CFL \cdot s_{\max}}{c} \quad (3.11)$$

In particular, a $CFL < 0.2$ ensures comparable discretization errors in space and time for the employed general-alpha solver. In order to reduce computing time, a CFL -number between 0.1 and 0.2 is used [91].

Given the simulation scheme, we calculate the enhancement factors for periodic slit arrays with periodicity $100 \mu\text{m}$, $50 \mu\text{m}$ and $10 \mu\text{m}$, a gap of $2 \mu\text{m}$ and a gold height of 100 nm . As an additional parameter, we model the enhancement structures free-standing and on a soda lime glass substrate with refractive index $n = 2.6$ [92]. We use a generic terahertz pulse as an incident electric field, and the shape of the enhancement in the slit at 50 nm height is shown in fig. 3.6(a), showing the u-shape. The frequency-dependent enhancement factors in fig. 3.6(b) are obtained from the ratio of the Fourier-transformed enhanced and incident fields averaged in the slit at 50 nm height. Regarding the free-standing structures, the enhancement factors follow at low frequencies the quasi-static value from eq. (3.7) and show a subsequent roll-off at higher frequencies. This behavior is more pronounced for larger periodicities. Consideration of the substrate leads to an overall lower enhancement and shift to lower frequencies.

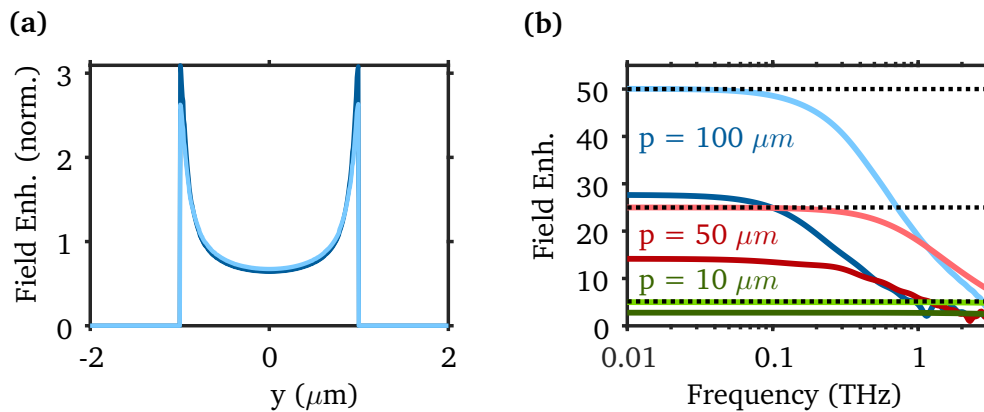


Fig. 3.6: Enhancement in a periodic slit array (a) The profile of the enhancement in the slit is normalized to the mean enhancement factor. We show the results for $100 \mu\text{m}$ periodicity on glass (dark blue) and without substrate (light blue), that provide nearly the same u-shape with higher fields at the edges. (b) The field enhancement as a function of the frequency for $100 \mu\text{m}$, $50 \mu\text{m}$, and $10 \mu\text{m}$ periodicity and a $2 \mu\text{m}$ gap. The dark colors provide the results with a glass substrate, the light versions without substrate. The dashed lines indicate the quasi-static enhancement factors.

Dielectric attenuation

In the calculations of the (enhanced) electric field strength F_{THz} , we have not yet included the investigated sample: an ensemble of colloidal quantum dots. Principally, the electric field strength in the quantum dots strongly depends on the dielectric constant of the nanocrystals and also on the dielectric environment. However, in literature, there are

different approaches to deal with this local field problem. In ref. [93], the dielectric constant for CdSe-CdS core-shell quantum dots, which are similar in size to the ones we use, is determined to $\varepsilon'_{\text{QD}} \approx 10$ using the Maxwell-Garnett effective medium theory. Therefore, the enhanced THz field in a single quantum dot is $F_{\text{QD}} = F_{\text{THz}}/\varepsilon'_{\text{QD}}$, thus, lowered by a factor of 10. Additionally, the quantum dots do not form a homogeneous layer, and in particular, in a thin film of quantum dots, the dielectric constant is further dependent on the nanoscopic structure and surrounding, e.g., voids in the film or ligands on the surface, that are crucial to modify the quantum dot properties such as the solubility [94]. In ref. [95], the electric field in the quantum dot film is calculated via $F_{\text{QD}} = \frac{\varepsilon'_i}{f\varepsilon'_i + (1-f)\varepsilon'_{\text{QD}}} F_{\text{film}}$ using the permittivity of the ligand ε'_i and a fill-factor f resembling the quantum dot volume ratio. This leads to a lower electric field in the quantum dots compared to the film in the case of the application of a DC electric field with constant potential difference applied to the electrodes. They relate the electric field strength in the film F_{film} and the quantum dots F_{QD} to the ratio of the permittivities $\frac{F_{\text{film}}}{F_{\text{QD}}} = \frac{\varepsilon'_{\text{QD}}}{\varepsilon'_{\text{film}}}$. Therefore, the electric field depends strongly on the microstructure of the quantum dot layer. Additionally, one also has to take into account the Fresnel reflection of the THz beam at the surface of the quantum dot film [96]. Corrections to the local field in the quantum dot with respect to the macroscopic external field F_{ext} can also be dealt with in the Onsager-Böttcher model, see, e.g., [97, 98]. Taking into account the permittivity of the surrounding dielectric ε'_d , the internal field is $F_{\text{int}} = \frac{3\varepsilon'_d}{2\varepsilon'_d + \varepsilon'_{\text{QD}}} F_{\text{ext}}$.

Given the associated uncertainties in the determination of the local field, we will use the incident field strength in all our discussions and graphs, and provide the simulated enhancement factors in absence of the quantum dots.

3.2 Quantum-confined Stark-effect in low-dimensional semiconductors

Strong electric fields provide the possibility to alter the optical properties of, e.g., dyes, gases, and semiconductors [99]. Historically, the effect of an external electric field on the optical properties was first described by J. Stark in 1913, who observed the splitting of electronic levels in hydrogen [100]. In this chapter, we describe in particular the quantum-confined Stark-effect in low-dimensional semiconductors, which typically manifests in a quadratic scaling of the bandgap energy shift with the external field. The following description of the QCSE theory, equations and its computational realization are oriented to a large extent on the book "Quantum Wells, Wires and Dots: Theoretical and Computational Physics of Semiconductor Nanostructures" by P. Harrison and A. Valavanis [101].

Theoretical description of low-dimensional semiconductors

The effect of quasi-static electric fields on the electronic structure of low-dimensional semiconductors is modeled via the time-independent Schrödinger equation. Starting from a bulk semiconductor, the Schrödinger equation in effective mass approximation can be written as:

$$-\frac{\hbar^2}{2m^*}\nabla^2\Psi = E\Psi \quad (3.12)$$

Here, m^* denotes the effective mass, which approximately accounts for the effect of the periodic crystal potential, Ψ the wavefunction, and E the energy eigenvalue. In particular, the formulation only treats the envelope function Ψ , and is therefore called the envelope function approximation. The Bloch-function part u , which oscillates on the level of the crystal lattice is neglected from the treatment. On a microscopic level, the ansatz for the wavefunction Ψ_m reads as:

$$\Psi_m = \Psi \cdot u \quad (3.13)$$

In detail, two energy bands can be distinguished: the conduction and the valence band, containing electrons and holes, when electrons from the valence band are excited to the conduction band. In a semiconductor, the two bands are separated by a bandgap energy E_g . The motion of electrons can be confined by reducing one or more dimensions of the bulk semiconductor, see fig. 3.7. Typically, heterostructures are created by joining two or more different semiconductor materials side by side. A potential term $V(r)$ as a function of a spatial coordinate r is introduced to describe the energy potential of the heterostructure:

$$\left(-\frac{\hbar^2}{2m^*}\nabla^2 + V(r)\right)\Psi = E\Psi \quad (3.14)$$

Depending on the size and the materials, different alignments of the bands occur, as depicted in fig. 3.8. In this work, quantum dots consisting of CdSe cores and CdS shells are employed, and the respective effective masses and bandgaps are provided in table 3.1. The band offset between core and shell, defining the alignment type, is not directly predictable from the material composition, as it depends, e.g., on the fabrication process [102]. Typical values suggest a conduction band offset of ± 0.3 eV resulting in a valence band offset of $0.4 - 1.0$ eV, according to the bandgaps [102]. Consequently, all three presented alignments are possible. Notably, the classification of electron-hole pairs, excitons, in the aforementioned types does not solely depend on the band alignment but also on the size of core and shell [103, 104].

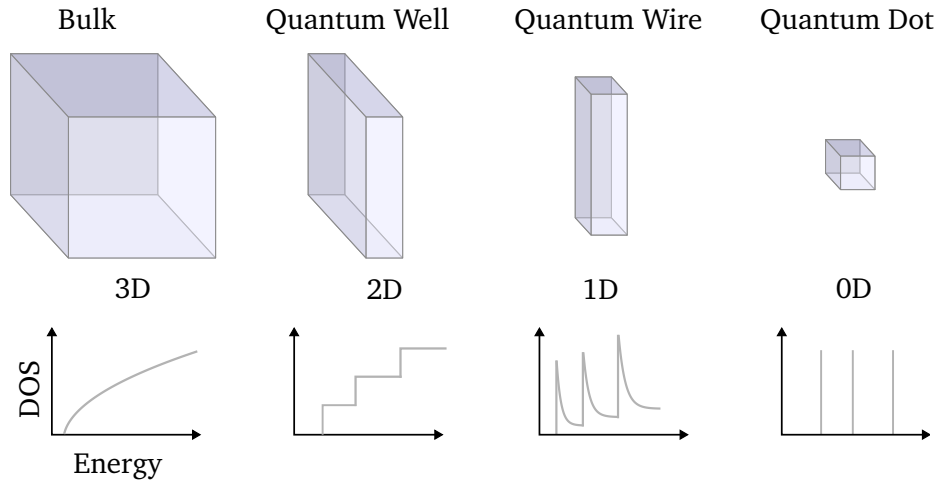


Fig. 3.7: Types of quantum confined structures. In a bulk semiconductor, the electron movement is not confined, providing 3 degrees of freedom. When one or more dimensions are decreased below the material-specific exciton radius (CdSe: $a_{exc.} \approx 6$ nm), quantum-size effects play a role [105]. Depending on the confinement, quantum wells, wires, or dots are created. This further confinement leads to an increasing discretization of the energy in specific states, as evident from the density of states (DOS) that is continuous for the bulk and discrete in the case of a quantum dot. Adapted from ref. [106].

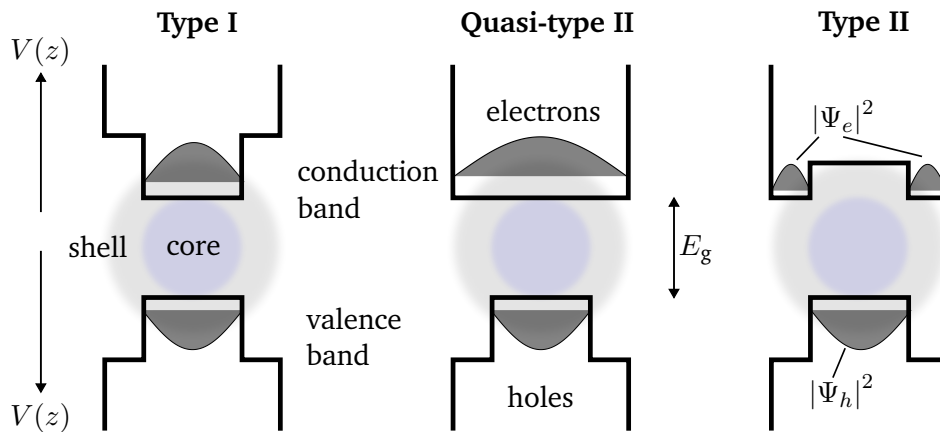


Fig. 3.8: Band alignments in heterostructures. Depending on the design of a semiconductor heterostructure, different band alignments for valence and conduction band are feasible. Typical for heterojunctions, the potential $V(z)$, which describes the material-dependent confinement, is discontinuous at the interface. For a type I band alignment, the lowest wavefunctions for electron and hole are confined to the core. Quasi-type II alignment describes the case of a vanishing band offset between core and shell, where the electronic wavefunction is spread out over the whole heterostructure. In contrast to type I quantum dots, the probability densities $|\Psi_{e,h}|^2$ of electron and hole in type II quantum dots are spatially separated due to a characteristic band offset for the core and shell potential. Adapted from ref. [107].

Tab. 3.1: Values for the effective mass for electron m_e^* and hole m_h^* and the bandgap E_g for CdSe and CdS, from [104]. m_0 denotes the electron mass.

Material	m_e^*	m_h^*	E_g (eV)
CdSe	$0.13m_0$	$0.45m_0$	1.75
CdS	$0.21m_0$	$0.80m_0$	2.49

One-dimensional particle in a box and Stark-effect

An introductory example for wavefunctions in confined structures is given by the one-dimensional particle in a box, resembling a quantum well. The potential V inside the box with length L is 0 and ∞ outside. Therefore, $\psi \neq 0$ only inside the box, because of the finite potential. Using the ansatz $\Psi(z) = A \sin(kz) + B \cos(kz)$, following solution for the energy levels E_n and the wavefunctions Ψ_n are found, where n is an integer:

$$E_n = \frac{\hbar^2 \pi^2 n^2}{2mL^2} \quad (3.15)$$

$$\Psi_n(z) = \sqrt{\frac{2}{L}} \sin\left(\frac{\pi n z}{L}\right)$$

Hence, the energy E_n is proportional to $\frac{1}{L^2}$ and can be tuned by the size of the box. In case of a finite potential outside of the box, the wavefunctions will penetrate the walls. The application of a constant external electric field F to the semiconductor structure leads to an additional contribution to the potential, namely $-eFz$ for an electron with the elementary charge e :

$$\left(-\frac{\hbar^2}{2m^*} \nabla^2 + V(z) - eFz\right) \Psi = E \Psi \quad (3.16)$$

The field-induced change in potential reads eFz for the holes, thus, a reversed tilting of the potential compared to the electrons. Since the wavefunctions move to the lower potential side in the quantum well, the electron and hole energies of the first levels are effectively lowered, leading to a lower transition energy $E_F = E_0 + \Delta E$. The scaling of this effect with the electric field can be estimated via perturbation theory. First-order changes of ΔE with the field F are described by:

$$\Delta E^{(1)} = \langle \Psi_1 | -eFz | \Psi_1 \rangle \quad (3.17)$$

Since Ψ_1 is even and z is uneven, $\Delta E^{(1)} = 0$, thus, F does not induce changes in the ground state energy. In a second-order perturbation ansatz, $\Delta E^{(2)}$ reads as:

$$\Delta E^{(2)} = \sum_{m=2}^{\infty} \frac{|\langle \Psi_m | -eFz | \Psi_1 \rangle|^2}{E_m - E_1} \quad (3.18)$$

Since F is constant and the sum over m takes into account each of the excited states, one can find contributions $\langle \Psi_m | z | \Psi_1 \rangle \neq 0$. This leads to a quadratic dependence of the lowering of the ground state energy from the electric field, typical for the quantum-confined Stark-effect:

$$\Delta E \propto -F^2 \quad (3.19)$$

The energy shift for a quantum well with infinite barriers reads as [108]:

$$\Delta E = \frac{m^* e^2 F^2 L^4}{24 \hbar^2} \frac{1}{\pi^2} \left(1 - \frac{15}{\pi^2} \right) \quad (3.20)$$

Due to the quadratic scaling of ΔE with the electric field also, the term "second-order Stark-effect" is used. The effect is driven by a change in the polarizability $\Delta\alpha$. In contrast, also a linear dependency is observed in systems with a permanent dipole moment, which depends on the change in the permanent dipole moment $\Delta\mu$. From this point of view, ΔE is typically written in vector notation as [99]:

$$\Delta E \propto -\Delta\vec{\mu} \cdot \vec{F} - \frac{1}{2} \vec{F} \cdot \Delta\vec{\alpha} \cdot \vec{F} \quad (3.21)$$

Matrix-formulation of the Schrödinger equation

In order to study the quantum-confined Stark-effect, we solve eq. (3.16) in a finite-difference approach. This means that the derivatives of a function $f(z)$ are rewritten as differences of f at points separated by δz . If the interval δz is sufficiently small, the first derivation can be approximated by:

$$\frac{\partial f}{\partial z} \approx \frac{\Delta f}{\Delta z} = \frac{f(z + \delta z) - f(z - \delta z)}{2\delta z} \quad (3.22)$$

In the same manner, also the second derivative is approximated by a difference:

$$\frac{\partial^2 f}{\partial z^2} \approx \frac{f(z + \delta z) - 2f(z) + f(z - \delta z)}{(\delta z)^2} \quad (3.23)$$

In case of a discontinuity of the effective masses, e.g., in a core-shell quantum dot, the so-called BenDaniel and Duke boundary conditions need to be obeyed. Therefore, $\Psi(z)$ and also the term $\frac{1}{m^*} \frac{\partial}{\partial z} \Psi(z)$ must be continuous. The effective mass in such a heterostructure is a function of the spatial coordinate and, therefore, the Schrödinger equation with external electric field is written as:

$$\underbrace{\left(-\frac{\hbar^2}{2} \frac{\partial}{\partial z} \left(\frac{1}{m^*(z)} \frac{\partial}{\partial z} \right) + \underbrace{V(z) - eFz}_{V'} \right)}_H \Psi = E\Psi \quad (3.24)$$

This equation can be transformed into a finite-difference form that satisfies the BenDaniel and Duke boundary conditions:

$$\frac{-\hbar^2}{2(\delta z)^2} \left[\frac{\Psi_{j+1}}{m_{j+1/2}^*} + \frac{\Psi_{j-1}}{m_{j-1/2}^*} - \frac{\Psi_j}{m_{j+1/2}^*} - \frac{\Psi_j}{m_{j-1/2}^*} \right] + V'(z)\Psi(z) = E\Psi(z) \quad (3.25)$$

The indices denote the z -position, whereas $j + 1/2$ is the average between the respective values at $z(j)$ and $z(j + 1)$. The aforementioned equation can be numerically solved, e.g., by the shooting method or a matrix diagonalization approach. In this work, we have chosen the matrix method due to its superior performance. Hence, we rewrite eq. (3.25) as a matrix equation $H\Psi = E\Psi$ with the $N \times N$ tri-diagonal matrix H , with N the total number of spatial points:

$$H = \begin{pmatrix} b_1 & c_1 & 0 & \cdots & 0 \\ a_2 & b_2 & c_2 & \cdots & 0 \\ 0 & \ddots & \ddots & \ddots & 0 \\ \vdots & \cdots & a_{N-1} & b_{N-1} & c_{N-1} \\ 0 & \cdots & 0 & a_N & b_N \end{pmatrix} \quad (3.26)$$

The entries, a_i, b_i, c_i are derived from the finite-difference formulation of the Schrödinger equation:

$$a_{i+1} = c_i = -\frac{\hbar^2}{2m_{i+\frac{1}{2}}^* (\delta z)^2} \quad (3.27)$$

$$b_i = \frac{\hbar^2}{2(\delta z)^2} \left(\frac{1}{m_{i+\frac{1}{2}}^*} + \frac{1}{m_{i-\frac{1}{2}}^*} \right) + V'_i$$

The resulting N energy eigenvalues and eigenvectors, which represent the wavefunctions, are computed using LAPACK routines, that are implemented in the numpy package for python [109]. In a final step, the wavefunctions are normalized.

Stark shift in a quantum well

We numerically study the QCSE by solving for the wavefunctions in the 1d-case and calculate the change in the ground state energy ΔE for a 5 nm CdSe quantum well as a function of the external electric field F . The resulting first electron wavefunctions for $F = 0 \text{ kV cm}^{-1}$ and $F = 400 \text{ kV cm}^{-1}$ are shown in fig. 3.9(a). The resulting shift in the ground state energy is displayed as a function of the electric field along with the theoretical values in fig. 3.9(b), showing the lowering of the energy proportional to the square of the electric field.

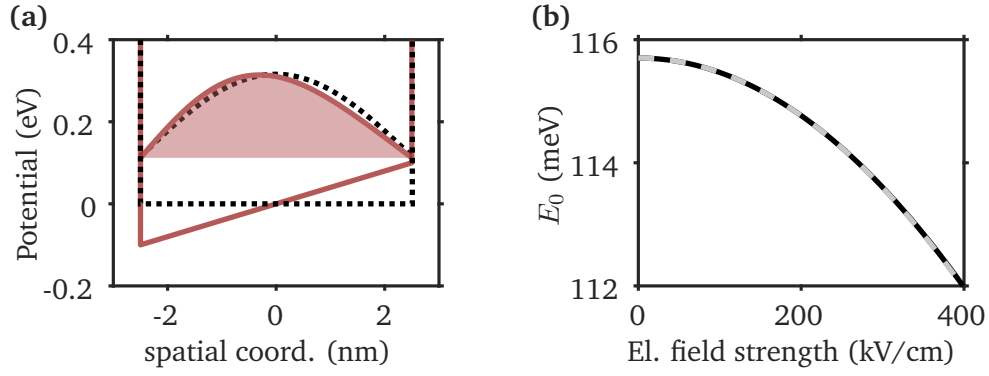


Fig. 3.9: Simulated Stark shift in a quantum well. (a) Potentials of a 5 nm CdSe quantum well with infinite barriers and first electronic wavefunction for 0 (black, dashed) and 400 kV cm^{-1} (red) external electric field. The tilted potential shifts the wavefunction to its lower side. For the calculations, a discretization of $\delta z = 0.01 \text{ nm}$ has been used. (b) The simulated energy eigenwert (black) of the first electronic state is lowered with increasing external electric field and agrees with the analytic solution (gray, dashed) from eqs. 3.15 and 3.20.

Field-induced changes in emission and absorption

A static electric field tilts the potential of quantum structures, resulting in modified wavefunctions and eigenenergies. Therefore, the absorption and emission process differs in the presence and absence of an external electric field. Here, we follow the approach described in ref. [110] to calculate the wavefunctions and transition strengths in 1d. This method has already been applied in ref. [96] to simulate different band alignment types and their influence on ultrafast quantum dot absorption spectra that are altered by strong THz pulses.

Generally, absorption occurs in a semiconductor upon resonant interaction with an optical field at photon energy $\hbar\omega$ larger than the bandgap. This creates an exciton consisting of an electron in the conduction band and a hole in the valence band, which are coupled with lowered energy by the exciton binding energy. This is typically treated by solving the Schrödinger and Poisson equation in a self-consistent way. Here, we are only interested in qualitative aspects of the QCSE, and therefore, we neglect the Coulomb attraction given by the two charges. The exciton can recombine either by emission of a photon or via a non-radiative decay path, and the oscillator strength f for a specific transition reads as [110]:

$$f = \frac{E_p}{2E'} \left| \int \Psi_e(z) \Psi_h(z) dz \right|^2 \quad (3.28)$$

Here, E_p is the Kane energy ($E_p = 17.5$ eV for CdSe [111], $E_p = 19.6$ eV for CdS [112]) that arises from the Bloch wavefunctions and E' the exciton transition energy, which we calculate from the eigenenergies E_e and E_h of electron and hole:

$$E' = |E_e| + |E_h| \quad (3.29)$$

Hence, the absorption strength is proportional to the squared overlap of the electron and hole wavefunctions. Therefore, only transitions for $\Delta n = 0$ are allowed without external electric field, since the wavefunctions are orthogonal. Owing the fact that we experimentally investigate large ensembles of quantum dots with a distribution of diameters and, thus, a distribution of emission wavelengths, we assume that the linewidth of the absorption and emission process is governed by the size distribution of the nanocrystals. The energy of the first exciton $E_{\text{exc.}}$ can be estimated via the bandgap of the bulk and the energy of the first electron and hole state (compare eq. (3.15)):

$$E_{\text{exc.}} = E_g + \frac{\hbar^2 \pi^2}{2m_e^* L^2} + \frac{\hbar^2 \pi^2}{2m_h^* L^2} \quad (3.30)$$

If the well size L now is changed by a small $\pm \Delta L$, the exciton energy changes by $\Delta E'$ [96]:

$$\Delta E' = \mp 2 (E_{\text{exc.}} - E_g) \frac{\Delta L}{L} \quad (3.31)$$

The latter expression is then used to determine the inhomogeneously broadened absorption and emission lines, using a Gaussian lineshape [96]:

$$\Delta E'(E') = \exp\left(-\left(\frac{E - E'}{\Delta E'}\right)^2\right) \quad (3.32)$$

The change in absorbance $\Delta A(E, F)$ as a function of the energy E and the electric field F is then calculated from the difference in the oscillator strengths with (f_F) and without field (f_0) multiplied with the respective lineshapes:

$$\Delta A(E, F) \propto [f_F \cdot \Delta E'_F - f_0 \cdot \Delta E'_0] \quad (3.33)$$

For multiple transitions, the individual ΔA are summed up. Notably, the absorbance A is related to the experimentally accessible transmission T :

$$A = \log_{10}(1/T) \quad (3.34)$$

Band structure in CdSe nanocrystals

In a more accurate description, the band structure for wurtzite semiconductors, such as CdSe, is especially for the valence band more complex than described before and comprises more than one band. In particular, the conduction band is created by 5s orbitals of cadmium and the valence band by 4p orbitals of selenium, which are sixfold degenerated. Three subbands arise, namely the light- and heavy-hole-band (lh , hh) and the split-off band (so), as depicted in fig. 3.10(a). lh and hh are slightly separated by Δ_{cf} induced by the crystal field ($\Delta_{cf} = 25$ meV, bulk CdSe) – the so is split-off by the spin-orbit-coupling ($\Delta_{so} = 0.42$ eV, CdSe) [105].

In quantum dots, the valence bands described above mix due to the confinement, and regarding the relative large Δ_{so} , we will only study the mixing of lh - and hh -band. To this purpose, we have to reconsider the Bloch-functions and especially the associated angular momentum J , since the crystal lattice plays an important role. The lh - and hh -band are related to $J = 3/2$, the so -band to $J = 1/2$. The total angular momentum $F = L + J$ is the relevant quantum number using the orbital momentum L of the envelope wavefunction. Due to the so-called S-D mixing, states with L and $L + 2$ are involved in the mixing. The resulting states are labeled as nL_F using the smallest involved L . L is then typically given as S, P, D, F for $L = 0, 1, 2, 3$. The lowest resulting states for a CdSe quantum dot are shown in an energy diagram in fig. 3.10(b) for conduction and valence bands along with the allowed transitions. Notably, the transition rule $\Delta n = 0$ is relaxed due to the band mixing, and therefore, e.g., the transition from $2S_{3/2}(h)$ to $1S(e)$ is allowed [105].

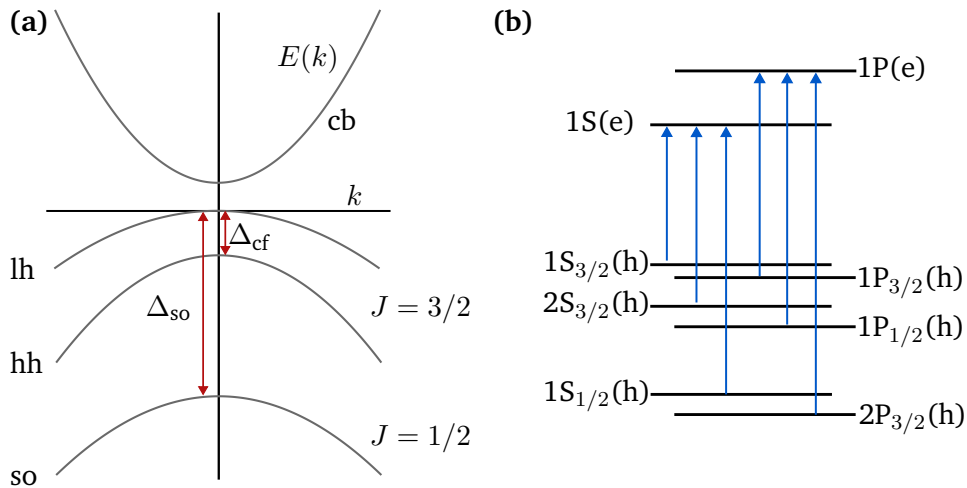


Fig. 3.10: Band structure in CdSe and resulting quantum dot states. (a) The band structure for bulk wurtzite semiconductors close to the wavevector $k = 0$ can be described in the conduction band (cb) with a single band and in the valence band with lh -, hh - and so -subbands. Adapted from [105]. (b) Energy diagram for a CdSe quantum dot with the allowed transitions (blue arrows). Adapted from [105].

3.3 Experimental detection of the QCSE in absorption and emission

The aforementioned absorption changes in quantum dots due to electric fields can be detected directly by measuring changes in the transmission or via changes in the emission rate. Here, we present the employed techniques to detect the QCSE, where we typically modulate the applied electric field and detect differential changes. The modulation, as well as the chopper reference or function generator signal, have a rectangular shape.

Generation of static electric fields

Complementary to ultrashort electric fields using THz pulses, we also employ static electric fields to alter the optical properties of the quantum dots. To this end, we typically utilize gold microstructures forming opposing electrodes comparable to a plate capacitor. The two parts of the microstructure are connected to a voltage and a grounded connection. We attach copper wires with silver lacquer to the gold structure. Modulated fields with rectangular shape are provided by combining an arbitrary function generator (DG1022Z, *Rigol*), a DC voltage source (PPS-16005, *Voltcraft*; TPS-4000, *Topward electric instruments*) and a voltage amplifier, providing voltages between 0 V and 60 V at frequencies up to 1 kHz.

Differential transmission detection

The field-modulated absorption is measured by detection of the differential transmission using balanced detection, boxcar averaging, and subsequent demodulation of the signal with a lock-in amplifier at a modulation frequency of f_{mod} , as sketched in fig. 3.11. For the balanced detection, a part of the beam is split off and directed to one arm of the detector without trespassing the sample. The circuit inside the balanced detector (PDB 210A/M, *Thorlabs*) takes the difference of both arms, suppressing fast and slow fluctuations of the laser power (“common mode noise”). The difference signal is not well matched to a lock-in amplifier, as the output pulse duration is much shorter than the time between two subsequent laser pulses, as the output provides a 3dB output bandwidth of up to 1 MHz. Therefore, a boxcar averager (SR250, *Stanford Research Systems*) generates an integrated, low-pass filtered signal proportional to the difference signal by integrating over one detector pulse. Subsequently, this is demodulated by the lock-in amplifier (SR850, *Stanford Research Systems*) at f_{mod} . The absolute signal modulation can be obtained by balancing the detector arms and measuring the output of the boxcar averager while

blocking one beam path, providing the voltage for 100 % modulation. The scaling of the lock-in output is provided by the sensitivity setting, and additionally, a correction for rectangular modulation has to be considered. Such a modulation is given when using a mechanical chopper, and consequently, the signal needs to be scaled by $1/0.45$ as the lock-in amplifier detects only the sinusoidal parts at f_{mod} . [113]. Femtosecond temporal delay between THz and optical pulses is enabled in all experiments by a mechanical delay stage in the pump beam path.

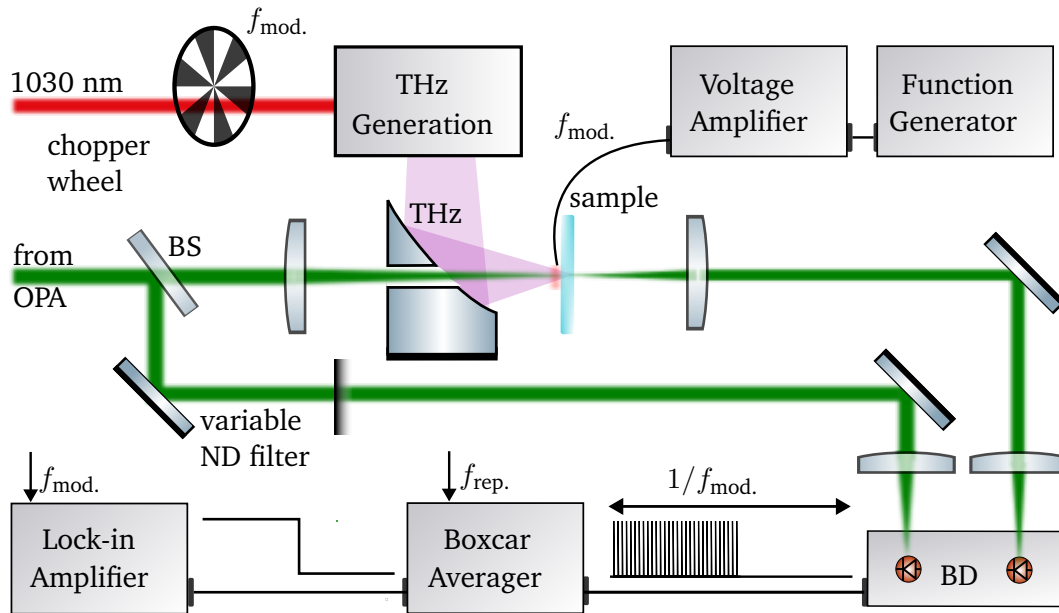


Fig. 3.11: Measurement of field-induced transmission changes. The QCSE is induced either by a THz pulse or a DC electric field in the quantum dots. We modulate the THz beam by f_{mod} using a mechanical chopper in the pump beam path. In particular, the chopper blade is covered with aluminum foil to avoid ablation. Also the DC fields are modulated with f_{mod} using a function generator. Pulses from the OPA are focused with a lens ($f = 75$ mm) on the sample, and we detect changes in the transmission using a pair of balanced diodes (BD). For optimal noise suppressing, the BD output is balanced to zero using a variable neutral density filter in one arm. The resulting output voltage is converted in a low-pass filtered signal by a boxcar averager suited for demodulation with a lock-in amplifier. Subsequently, the signal output voltage from the latter is detected using an analog-digital converter connected to a computer. Finally, the signal is recorded using a LabView program.

Differential emission detection

The quantum dots emit luminescence, which we collect using an objective (BD Plan 20x NA = 0.4, BD Plan 40x NA = 0.5, *Nikon*) or a lens with a short focal length (AC254-030-AB-ML f=30 mm, *Thorlabs*). In the OPA beam, we use a 550 nm shortpass filter (FESH0550, *Thorlabs*) to remove residual laser light from the OPA. The excitation beam and residual stray light from the THz generation, mostly fundamental and second-harmonic radiation around 1030 nm and 515 nm respectively, are filtered out using a shortpass and a longpass filter (FELH0550, FESH0750, *Thorlabs*), providing a detection window between 550 nm and 750 nm appropriate for CdSe quantum dot emission. The collected photoluminescence signal is focused onto the light-sensitive photocathode area of a fast photo-multiplier tube (PMT, H10721-20, *Hamamatsu*). The PMT is able to temporally resolve the radiative decay (~ 10 ns) of the fluorescence after pulsed excitation, given a fast rise time of 0.6 ns. Therefore, the output pulse duration of the PMT is also too short to be detected efficiently by a lock-in amplifier due to the low-duty cycle. In order to increase the ratio of spectral components at $f_{\text{mod.}}$, an RC circuit is used between PMT and the lock-in amplifier. According to ref. [114], the maximum signal for a randomly distributed arrival time of the photons within half of a modulation period $T/2 = 1/(2f_{\text{mod.}})$ can be achieved by using an RC circuit with a time constant $\tau = T/6$. The requirements for signal statistics are approximately given in our experiments, as the photons arrive within the radiative lifetime at the laser repetition rate of 10 kHz on the PMT, where we typically use pump modulation frequencies around $f_{\text{mod.}} = 150$ Hz. Accordingly, we employ an RC circuit with a time constant of $\tau = RC = 1\text{M}\Omega \times 1\text{nF} = 1\text{ms}$, optimizing the signal at 167 Hz modulation frequency.

Differential spectral and spatial detection

Spectral and spatial mapping can alternatively be achieved using a monochromator (SpectraPro HRS-300, *Teledyne Princeton Instruments*) with a spectrometer camera (PIXIS: 100B, *Teledyne Princeton Instruments*) or an imaging camera (Orca ER, *Hamamatsu*; Zyla 4.2, *Oxford Instruments*). Instead of focused quantum dot excitation, we employ a widefield illumination, and the collected light is imaged on the camera chip with a lens (LA1725-A-ML f = 400 mm, 2-inch diameter, *Thorlabs*) or focused on the entrance slit of the monochromator. In order to implement low-noise differential detection, we acquire multiple frames alternating with and without an external electric field. We subtract the averaged images using software based on triggered readout of the camera, phase-locked to $2f_{\text{mod.}}$ to separate frames with and without the THz pump. This is ensured by a customized trigger logic employing a microcontroller (Arduino Mega 2560) and a LabView program, see fig. 3.12(a). Specifically, a measurement is divided into several steps, e.g.,

different temporal delays between THz and optical pulse. A gate voltage set to LOW indicates a BUSY state of the measurement, e.g., when the delay stage moves. Switching to the HIGH-state initiates the acquisition of triggered images at $2f_{\text{mod}}$, by sending trigger pulses at the rising and falling edge of the rectangular chopper signal. Additionally, the microcontroller ensures that only a rising edge in the chopper modulation starts the trigger sequence, keeping the measurement locked to the same chopper phase over the whole measurement. When the desired amount of frames for the measurement step is acquired, the gate voltage is set to LOW. This procedure is sketched for one pair of frames in fig. 3.12(b).

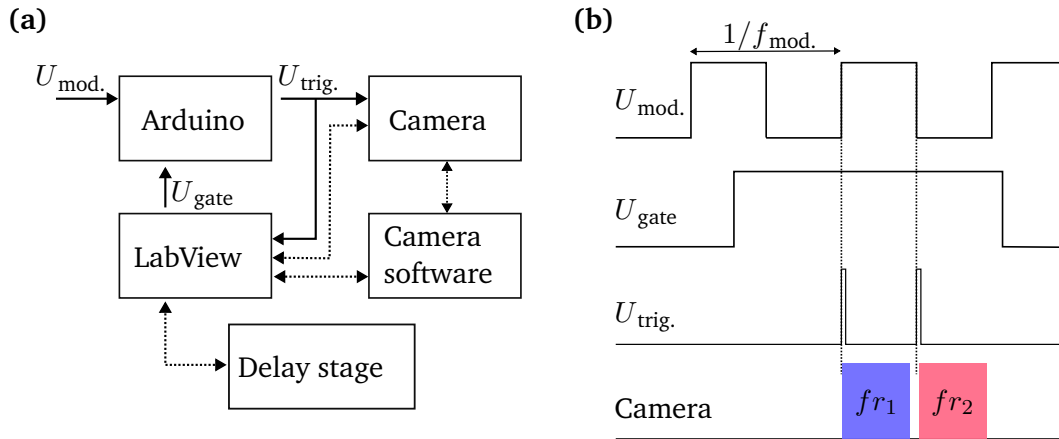


Fig. 3.12: Control and trigger scheme for differential spectral /spatial acquisition. (a) The procedure is controlled by a LabView program that starts the measurement by setting the gate voltage to HIGH. Then, the Arduino delivers the trigger pulses to the camera. Software control connections are shown as dashed lines. **(b)** The edges of the chopper reference voltage U_{mod} are converted to trigger pulses U_{trig} when U_{gate} is set to HIGH. In particular, the imaging sequence starts only at rising edges. The frames fr_i are acquired and subtracted via software post-processing.

The exact readout scheme depends on the particular camera. In the case of the spectrometer camera, the employed LightField software (*Teledyne Princeton Instruments*) acquires triggered frames that are subtracted from each other ("paired frames"). Additionally, a predefined number of pairs is averaged and the result is recorded using a LabView program. The readout of the Orca-CCD is not directly incorporated into a LabView routine. In particular, every frame is saved with a proprietary software (HPD-TA 8, *Hamamatsu*) and processed in a Matlab program to yield the differential images. The Zyla-CMOS camera readout and image processing are fully controlled with a LabView program. Each frame is buffered to the RAM of the measurement PC and processed to a differential video. In general, the sum of camera integration and readout time must be smaller than $1/2f_{\text{mod}}$, whereas f_{mod} is typically a few Hertz, to ensure a phase-locked measurement.

Modulation of quantum dot absorption and emission with ultrafast and static electric fields

4.1 Colloidal CdSe-CdS core-shell quantum dots

In this chapter, we investigate the QCSE in quantum dots using static and ultrafast electric fields. In particular, we employ colloidal CdSe-CdS core-shell quantum dots fabricated by Nicholas Kirkwood from the group of Prof. Paul Mulvaney (University of Melbourne). Details on the fabrication are provided in the supplemental information of ref. [115]. The ensemble absorption and emission spectra are presented in fig. 4.1(a), showing emission centered at a wavelength of $\lambda = 645$ nm with a FWHM of $\Delta\lambda = 28$ nm. From the shape of the absorption spectrum, the involved electron and hole states near the lowest transition can be assigned using the schematic state diagram in fig. 3.10(b). The radiative quantum yield of the nanocrystals is approximately 60% as measured relative to Rhodamine 101. The size as well as the size distribution of the quantum dots is studied using a transmission electron micrograph, displayed in fig. 4.1(b). From the data, an average diameter of 11 nm with a standard deviation of 1.2 nm is derived, as evident in the histogram of the size distribution in fig. 4.1(c). In particular, the CdSe core has a diameter of 4.3 nm covered by a CdS shell with a radius of 3.4 nm. Typically, the shell size is given in monolayers (ML) of the material, and for CdS, one ML has a thickness of 0.34 nm resulting in a shell of 10 ML thickness [116]. In all experiments, the quantum dots are solved in toluene and deposited via drop casting on the structure of interest with a typical concentration of ≈ 1 mg/ml.

4.2 1d simulation of the quantum-confined Stark-effect

Given the simulation scheme of the QCSE in a quantum well in section 3.2, we qualitatively discuss the QCSE in quantum dots, in particular the field-modulated emission and absorption spectra as well as the generic scaling behavior of the QCSE process with the electric field.

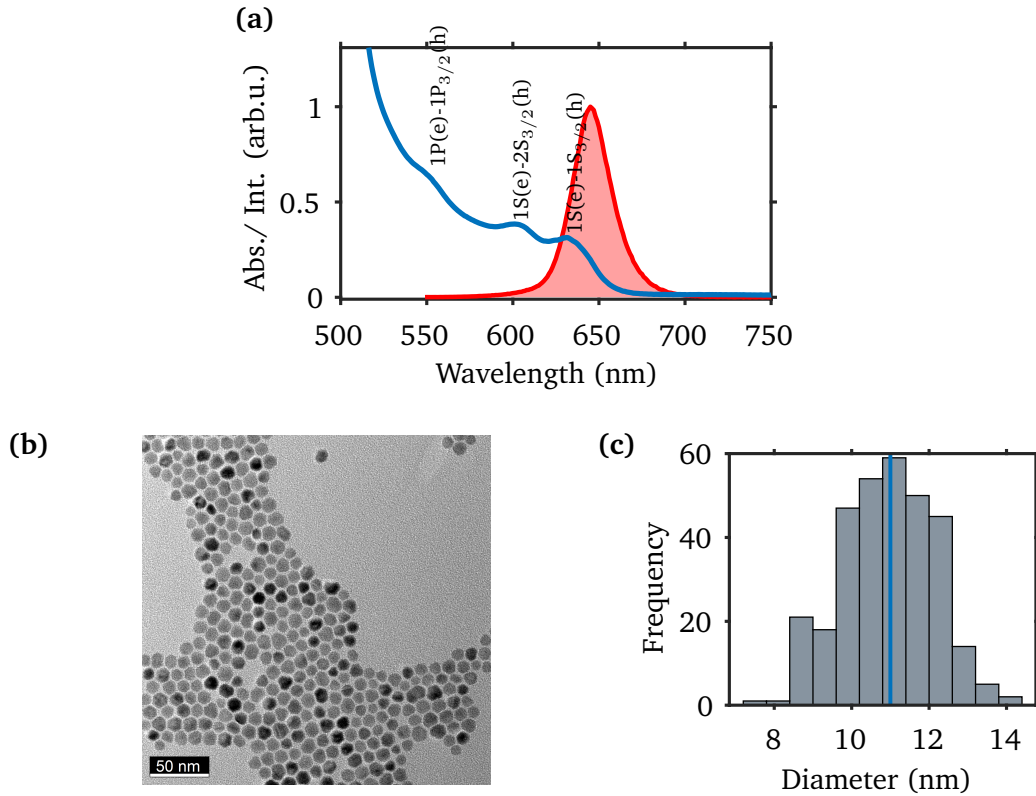


Fig. 4.1: Characterization of CdSe-CdS core-shell quantum dots. (a) Absorption and emission spectra of the employed nanocrystals. Additionally, the transitions are assigned to the peaks in the absorption spectrum. (b) Transmission electron microscope image of the quantum dots. (c) The histogram of the quantum dot diameters, derived from (b), is centered around 11 nm (blue line). All data has been captured by Nicholas Kirkwood.

First, we concentrate on the lowest transition involving the s-state wavefunctions of electron and hole, which is qualitatively relevant for the emission process. Since the exact band alignment is unknown, we use valence band offsets of 0 meV and ± 30 meV, corresponding to quasi-type II, type I and type II band alignment, respectively. For the spectral broadening of the lines, we employ the size dispersion. We use for the exciton energy $E_{exc.} = 1.92$ eV derived from the emission peak. Taking into account the size dispersion, we obtain $\Delta E = 36$ meV from eq. (3.31) in agreement with the emission spectrum. The calculated probability densities and the resulting (differential) spectra are provided in fig. 4.2, using the aforementioned dimensions of the quantum dot core and shell. Due to the separation of the wavefunctions with increasing field, the absorption is reduced. Additionally, the characteristic lowering of the transition energy with the square of the electric field leads to a redshift in the spectra. In particular, the strongest redshift and relative reduction of the absorption can be observed for the type-II alignment, where the wavefunctions are already highly separated at low fields compared to the other cases.

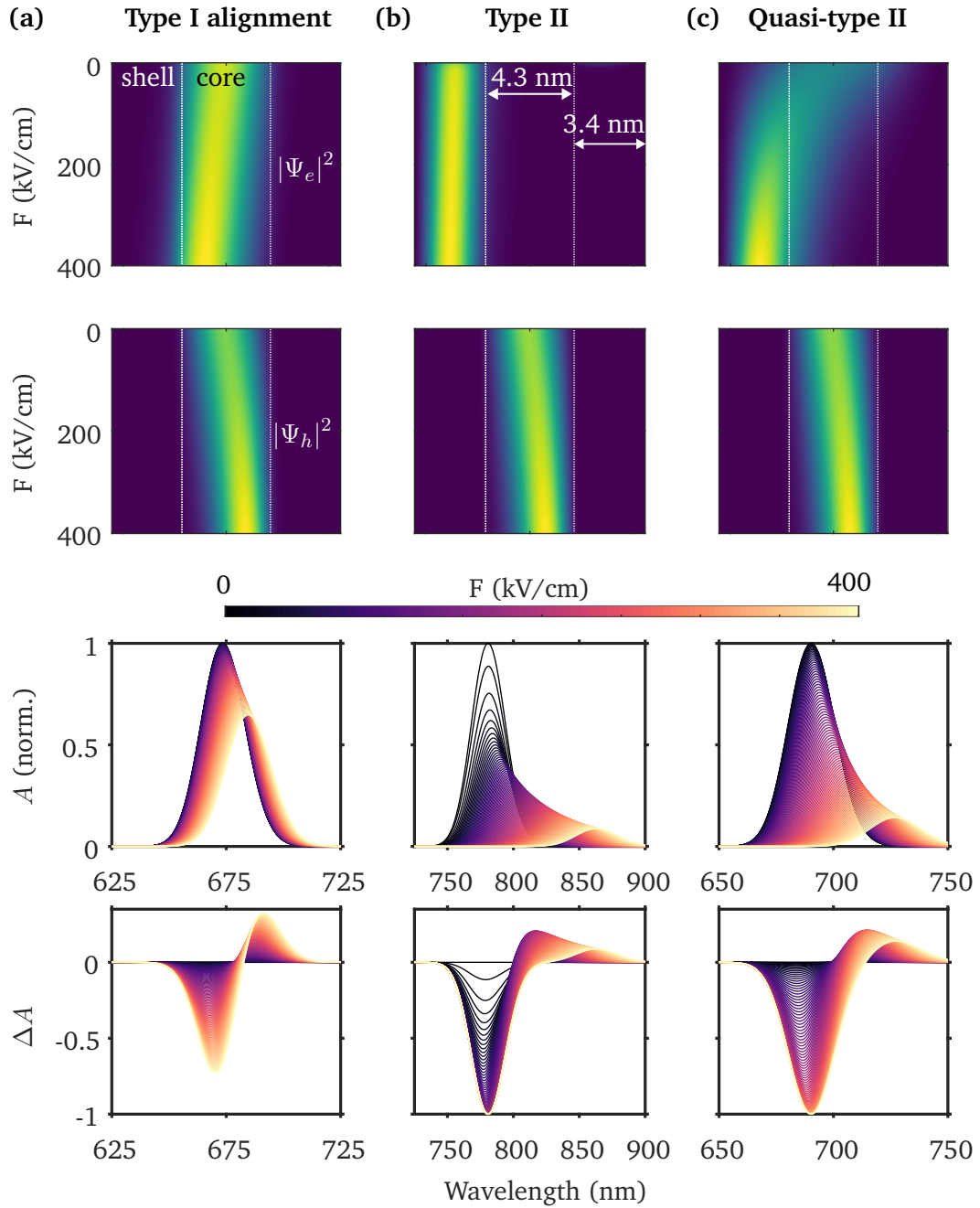


Fig. 4.2: Simulation of the QCSE for different band alignments. (a) For type I alignment, the wavefunctions for electron and hole, Ψ_e and Ψ_h , are solely confined to the core. They separate upon interaction with an external electrical field, leading to an increasingly redshifted, reduced absorption A . This is also evident from the differential absorption $\Delta A = A(F) - A(0)$. (b) In the case of a type-II band alignment, the wavefunctions separate rapidly, leading to a greatly weakened absorption when applying an electrical field. (c) The intermediate case, the quasi-type II alignment, offers a moderate separation of the wavefunctions between type I and type II. Thus, the redshift and also the reduction of the overlap, observable in the decrease of peak absorption, lies in between the two other band alignments.

The changes in absorption scale initially quadratic with the electrical field, as evident in fig. 4.3, where we show the differential absorption ΔA at 680 nm as a function of the applied field exemplary for the quasi-type-II band alignment. This behavior saturates at high fields, as the separation of the wavefunctions is limited by the potential. Experimentally, this saturation of the QCSE has been shown in ref. [10] by applying high-field THz pulses to InGaAs-GaAs quantum dots. In general, the strength of the field-induced modulation depends on the band alignment [96] and the accessed states [117], however, always scales quadratically in quantum dots – at least in the case of low to moderate fields before saturation [118, 119].

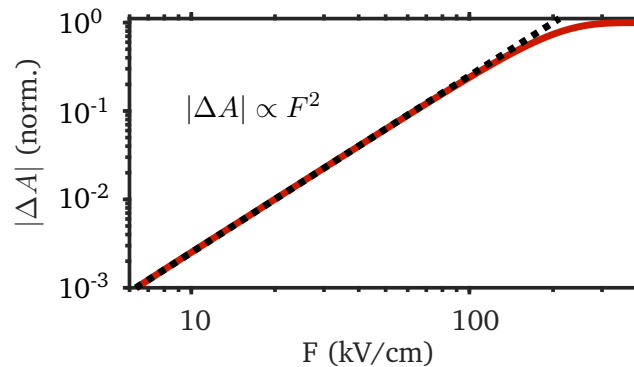


Fig. 4.3: Quadratic scaling of ΔA with the electric field. The simulated differential absorption ΔA at 680 nm (red) for the quasi-type II band alignment shows a quadratic scaling (dashed line) with the field, which saturates at high fields.

Additionally, we illustrate that initially forbidden transitions, here for $\Delta n \neq 0$, are increasingly allowed by tilting the confinement potential with an electric field. Therefore, we use the lowest electron and second lowest hole wavefunction. The results are provided in fig. 4.4, showing a dark state turned bright by an external electric field.

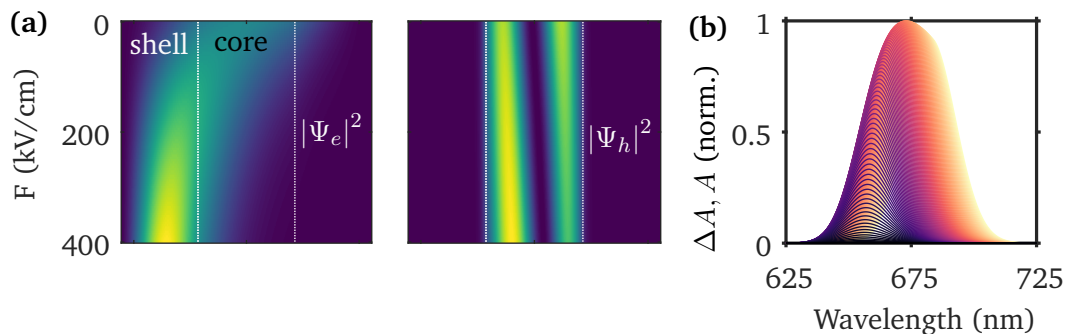


Fig. 4.4: Softening of selection rules by the QCSE. (a) The probability densities for electron and hole in a quasi-type II band alignment using the lowest electron and second-lowest hole state. (b) The initially forbidden transition is allowed as the orthogonality of the wavefunctions is canceled by the electric field, leading to an increased absorption for higher fields.

4.3 Emission and absorption modulation with static fields

First, we introduce the QCSE experimentally by applying static electric fields to the quantum dots. Static measurements are well established and studied in various low-dimensional structures [86, 120]. Here, we apply voltages U up to 35 V to a gap of approximately $3\ \mu\text{m}$ of a gold microstructure, resulting in maximum electric fields of $F \approx 120\ \text{kV cm}^{-1}$. In particular, we excite the quantum dots in the gap well above the bandgap with focused OPA pulses at 480 nm wavelength and detect the (differential) emission spectrum. Two acquisition modes have been employed: (a) the acquisition of spectra as a function of the applied electric field and (b) the acquisition of differential spectra by modulation of the voltage with a frequency of a few Hertz and automatic triggered subtraction of subsequent spectra. Typically, a few hundred spectra are collected for each voltage.

The spectra for varying electric field strengths are presented in fig. 4.5(a). Most apparently, the emission intensity at the peak is lowered by up to 7%. We extract a Stark shift of up to 2.2 meV using the center-of-mass of the emission spectra, showing the characteristic reduction of the emission energy, see fig. 4.5(c). Based on a fit with $\Delta E = a \times F^x$, the shift scales with $x = 2.1$ close to the quadratic dependence typical for the QCSE. Additionally, the overall shape of the emission changes slightly and is broadened for increasing fields, as evident in fig. 4.5(d), yielding an increased FWHM of about 3 meV. In literature, this effect is typically attributed to an increased exciton-phonon interaction, see refs. [9, 121].

The differential emission spectra in fig. 4.6(a) show the overall decrease of emitted photons, whereas the bandgap shift manifests itself in reduced emission at the initial peak wavelength and the emergence of red-shifted emission. In particular, the spectral changes qualitatively agree with the simulated changes in absorption from fig. 4.2. However, a direct comparison is rather difficult, e.g., due to the unknown band alignment. From the data, we examine the scaling of the changes in the emission with the electric field in fig. 4.6(b) in two regions: (i) around the initial emission peak at 645 nm and (ii) in the red-shifted region. Both ranges show an essentially quadratic scaling with the electric field with different strengths.

Additionally, we investigate field-induced changes in the absorption of the nanocrystals using pulses at a wavelength of 480 nm. The resulting differential transmission ΔT as a function of the applied electric field is shown in fig. 4.7, and the analysis yields that the differential absorption also scales essentially quadratic with the electric field.

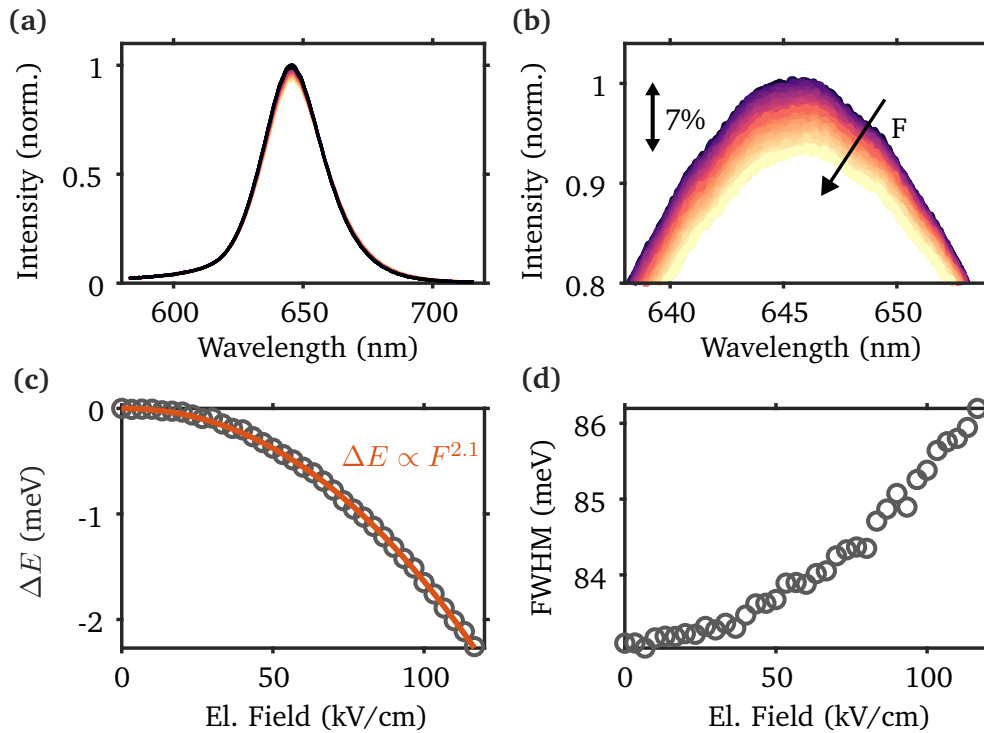


Fig. 4.5: QCSE of quantum dots in static electric fields. (a) Spectra for electric fields between 0 and $\approx 120 \text{ kV cm}^{-1}$ show most apparently a decrease in the peak emission intensity, arising from a detuned overlap of the electron and hole wavefunction. (b) The enlarged view from (a) shows the decrease of the peak emission by 7% for the highest applied field. (c) The characteristic red-shift of the peak emission (gray), corresponding to an effectively lowered bandgap, is evaluated and a fit (orange) yields the essentially quadratic dependency of the applied voltage. (d) The full-width at half-maximum of the emission spectra increases by up to 3 meV.

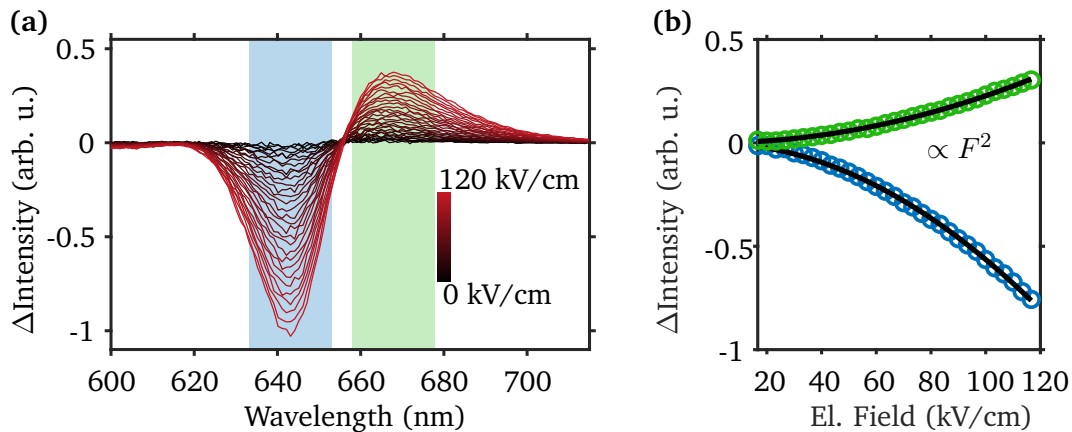


Fig. 4.6: Differential biased emission spectra. (a) The differential emission spectra between 15 kV/cm and 120 kV/cm (from black to red) show the overall reduced emission yield and the red-shifted luminescence. (b) The averaged changes in intensity from the blue and green colored areas from (a) show both close to quadratic scaling (fit in black).

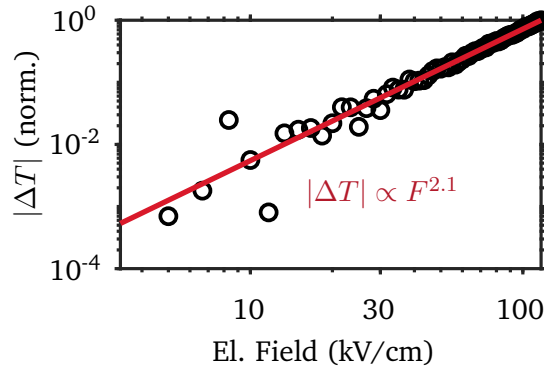


Fig. 4.7: Differential biased absorption at 480 nm. Analogously to the emission, the absorption is also modulated by a static electric field and also shows an essentially quadratic scaling with the applied electric field. Notably, the absorption at 480 nm is reduced for increased voltages, indicating a lower wavefunction overlap upon biasing.

4.4 Ultrafast modulation of quantum dot absorption

THz-induced absorption modulation in quantum dots

Terahertz pulses enable ultrafast, strong electric field evolutions that we will use in this section to study the absorption modulation of the CdSe-CdS quantum dots near the bandgap. Similar studies employing transient white-light absorption and tuned OPA pulses are reported in refs. [93, 96]. Here, we detect changes in the absorption using OPA pulses at different wavelengths to spectrally map the modulation of the absorption bands by measuring differential changes in the transmission of the pulses. The incident THz pulses are further enhanced in micro-slit arrays with a gap size of about $2 \mu\text{m}$ and a periodicity of $100 \mu\text{m}$.

The incident THz electric field is shown in fig. 2.12(a) and acts now as an ultrafast bias to the quantum dots. We measure two exemplary differential transmission curves at 641 nm and 662 nm, that show unipolar positive and negative changes, respectively, as presented in fig. 4.8. In particular, the measured waveform at 641 nm is well reproduced by the squared simulated electric field in the slit structure. From the simulation, we estimate the mean peak field to about 2 MV/cm. This leads to the conclusion that the oscillations of the THz electric near-field in the structure are imprinted onto the transmission. Additionally, the sign of the absorption change depends on the involved states in the quantum dots.

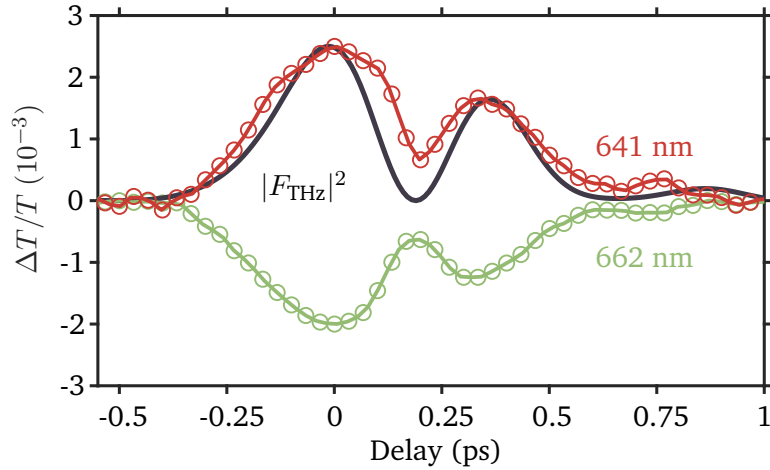


Fig. 4.8: Ultrafast absorption modulation in quantum dots using THz pulses. Two exemplary transient transmission curves at 662 nm (green) and 641 nm (red) show a decrease and increase in transmission, respectively. The characteristic shape of the signal is linked to the value of the electric field in the quantum dots. We calculate the signal shape by taking the square of the simulated near-field inside the slit structure, yielding the black line, showing good agreement with experimental data. We assume a quadratic scaling of the transmission signal and include a CEP shift 0.2π . Deviations arise, e.g., from the finite sampling pulse duration, leading to a broadened signal and blurred minima.

Terahertz Stark-spectroscopy of quantum dots near the bandgap

Similarly, we study the strength of the transmission changes for different wavelengths close to the bandgap from 580 nm to 700 nm and the resulting curves are presented in a 2d spectro-temporal representation in fig. 4.9. The evaluation of the absorption strength at the peak field yields fig. 4.10, showing at wavelengths above 620 nm a qualitatively similar behavior to the DC-induced emission modulation. Analogously, the electric field reduces the overlap of the $1S(e)$ and $1S_{3/2}(h)$ wavefunction, and the transition appears shifted at lower energy, yielding a lowered transmission in the presence of the THz pulse above 650 nm. At higher energies, more transitions contribute, and, e.g., forbidden transitions such as $1S(e)-1P_{3/2}(h)$, expected between $1S(e)-2S_{3/2}(h)$ and $1S(e)-1S_{3/2}(h)$, can appear [97].

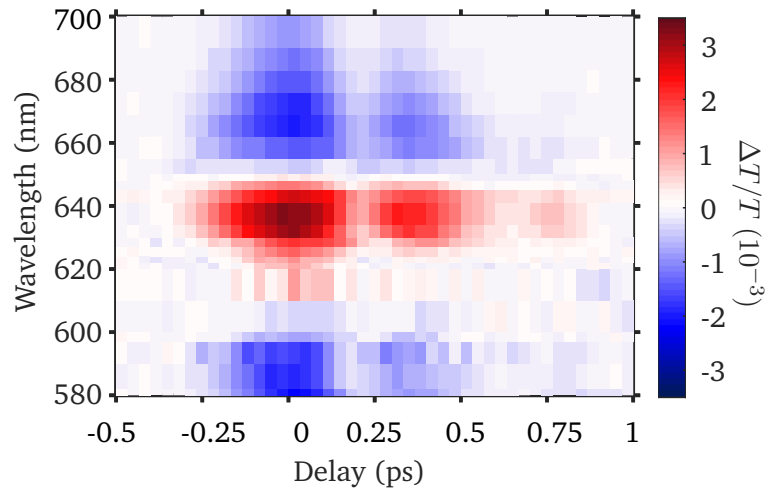


Fig. 4.9: Spectro-temporal transmission changes in the quantum dots. The THz-induced ultrafast transmission changes in the quantum dots exhibit a strong dependence on the absorbed wavelength. Besides the higher transmission close to 635 nm, also lower transmission, indicating a higher absorption, is observable due to the Stark-induced red-shift of the transitions. In between, also regions with no modulation appear.

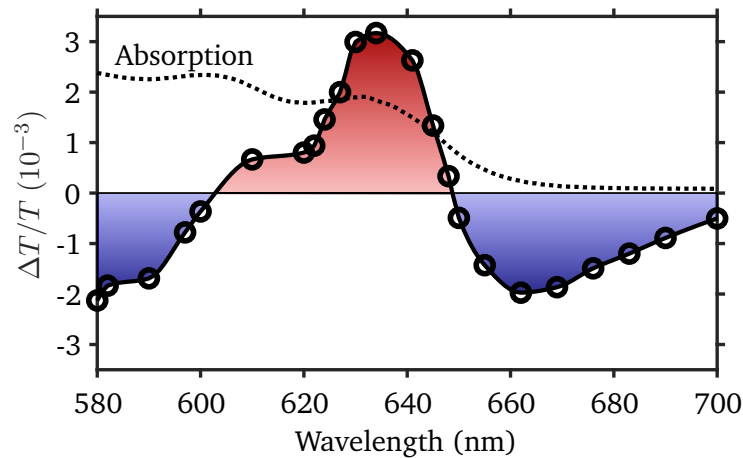


Fig. 4.10: Spectral dependence of the transient transmission changes. Here, we derived the $\Delta T/T$ values (circles) at the maximal signal at 0 ps delay from the traces in fig. 4.9. Additionally, the absorption spectrum is shown (dotted line). Comparable to the changes in the emission induced by a DC field, the curve shows the red-shifted absorption behavior at wavelengths above 620 nm. At lower wavelengths contributions from e.g. $1S(e)-2S_{3/2}(h)$ and also the formerly forbidden $1S(e)-1P_{3/2}(h)$ transition play a role.

Ultrafast absorption changes detected in the emission

Since the absorption process is modulated by an external field, also the total amount of emitted photons is changed as more or less excitons are created that decay in visible fluorescence. Therefore, we use a PMT to detect field-induced changes in the luminescence. For the measurement in fig. 4.11, the THz pulses are not enhanced further by a structure, and thus, the shape and strength of the field in the quantum dots are dictated only by the incident field. The THz-induced changes in emission upon excitation at 480 nm are provided in fig. 4.11(b), along with the square of the THz field, showing good agreement. We also show the square of the incident field convoluted with a 240 fs sampling pulse, illustrating the blurring of the minima and the overall broadening of the curve.

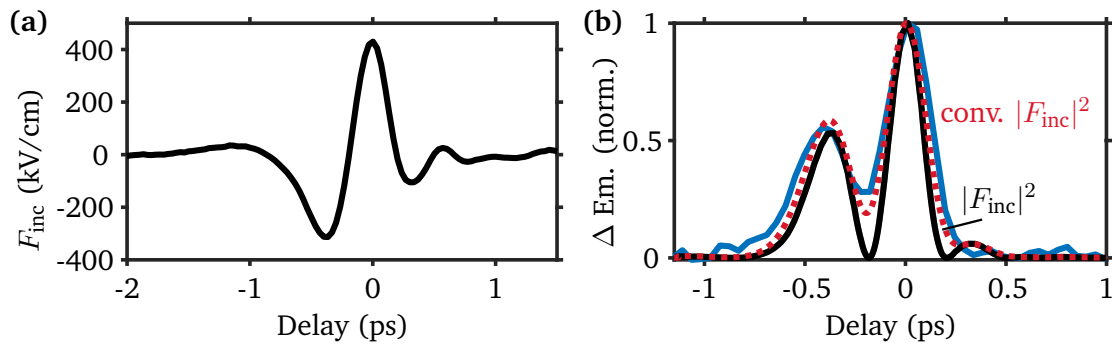


Fig. 4.11: Ultrafast absorption modulation in quantum dots using THz pulses detected in the emission. (a) The incident THz pulse, detected with EOS, provides a peak electric field above 400 kV cm^{-1} . (b) The normalized changes in the emission intensity (blue) follow the square of the incident electric field F_{inc} (black), as no field-enhancing structure is used, which would shape the near-field. The deviations arise from the convolution of the squared electric field with the finite sampling pulse duration, especially at the zero crossing of the incident waveform, as shown by $|F_{\text{inc}}|^2$ convoluted (red, dashed) with a Gaussian pulse with 240 fs duration ($1/e^2$).

Additionally, we investigate the modulation of the emission spectrum at a wavelength of 530 nm induced by THz pulses that are enhanced in a slit structure. The spectrum of the quantum dots at the peak modulation, as well as the original spectrum, is presented in fig. 4.12(a). In contrast to the DC-emission modulation, a change of the emission shape is not observable, as evident by dividing the spectra, showing a constant enhancement of about 12 % across the emission spectrum. This can be explained by considering the radiative lifetime of the quantum dots in the order of tens of nanoseconds, provided in fig. 4.12(b), rendering the modulation of the emission process by picosecond THz pulses highly inefficient. The amount of THz modulated emission is negligible compared to the unmodulated part, as we detect the integrated emission intensity and, thus, the modulation arises only from changes in the absorption rate.

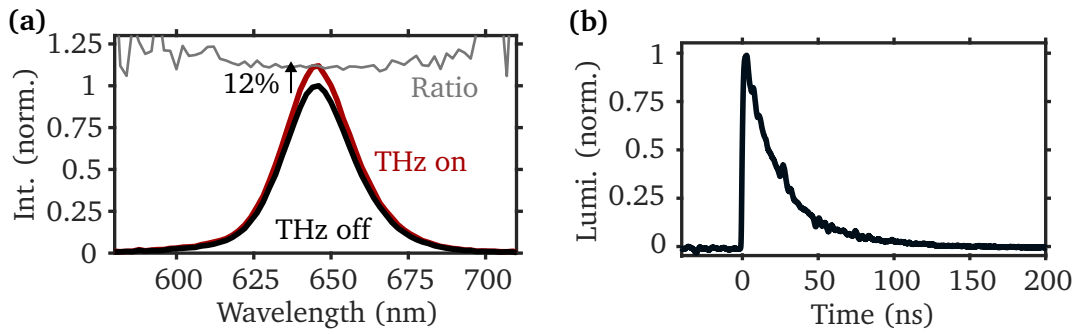


Fig. 4.12: Spectral emission modulation with a THz pulse. (a) The quantum dots exhibit an enhanced emission intensity (red) of 12% at the peak THz field upon excitation at 530 nm compared to no field (black). Additionally, the relative modulation of the spectra is shown (gray), showing no spectral changes, as only an overall increase in emission yield is observed. In particular, the THz pulses are enhanced in gold slits with a slit width of about $2\ \mu\text{m}$ and a periodicity of $100\ \mu\text{m}$. Taking into account an incident peak field of $400\ \text{kV/cm}$, the average field can be estimated to $2\ \text{MV/cm}$. (b) The excitation of the quantum dots decays radiatively on a much longer timescale ($\approx 100\ \text{ns}$) compared to the picosecond THz pulse. Therefore, only the absorption process in the quantum dots is altered, leading to practically no influence of the THz pulse on the long emission process. The lifetime data is captured using a photo-multiplier tube (H10721-20, Hamamatsu) in analog mode and a fast oscilloscope (Waverunner 204MXI 2 GHz, LeCroy).

4.5 Polarity reconstruction strategies for rectified signals

The QCSE signal in quantum dots depends nonlinearly on the electric field and is inherently insensitive to the field polarity due to the symmetry of the quantum dots. Consequently, the measured data is not directly suited for spectroscopic applications. Therefore, we developed two reconstruction strategies based on signal theoretical considerations to recover the underlying electric fields. Here, we concentrate on THz pulses that are shaped linearly by, e.g., a resonant antenna. Due to the QCSE in quantum dots, the field is rectified and scaled in a nonlinear fashion, as illustrated in fig. 4.13. The nonlinearity can be reverted rather easily, given the known scaling behavior of the QCSE. However, the reconstruction of the (absolute) polarity appears non-trivial because the unipolar signal allows for many different assignments of polarities, e.g., for an underlying antenna-shaped field.

Gouy-phase assisted polarity recovery

The shift of the carrier-envelope phase of a focused Gaussian beam, the Gouy-phase, is introduced in section 2.7. In short, the CEP changes by a value of π throughout the focus, but the envelope of the electric field does not change, or in other words, the amplitude spectrum remains constant. We can make use of this simple fact to recover the polarity of

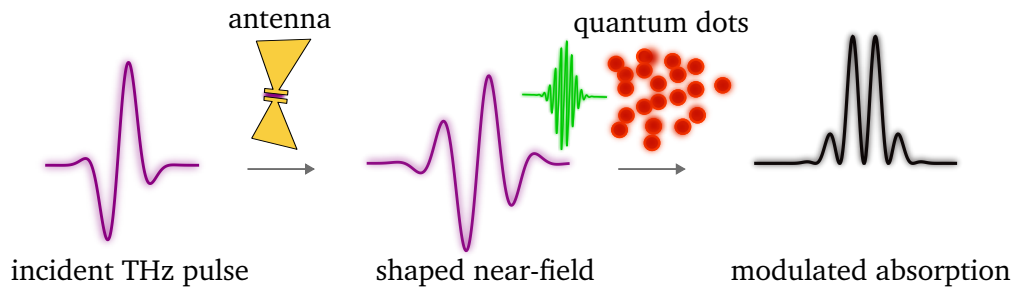


Fig. 4.13: Antenna-shaped THz-modulated absorption in quantum dots. An antenna shapes the near-field of an incident THz pulse. This field is readout using quantum dots and a probe pulse (green) and the pulse polarity information is lost due to the quantum dot symmetry.

the rectified signal by measuring the QCSE signal at two distinct locations z_i along the THz focus, as illustrated in fig. 4.14. This leads to two traces S_{QCSE} with different CEP shifts $\phi_i(z_i)$ and, therefore, different shapes. However, the amplitude frequency spectra of the underlying electric fields are the same, because only the carrier-envelope phase has changed.

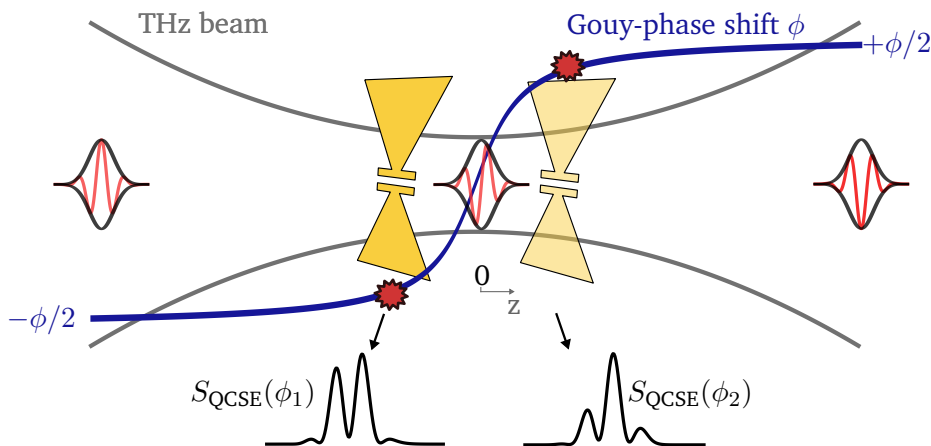


Fig. 4.14: Measurement procedure of a QCSE signal in quantum dots using a bowtie antenna at different z -positions. The measured signal S_{QCSE} is rectified and nonlinearly scaled by the QCSE. The modulations are phase-shifted by the Gouy-phase.

In order to find the underlying electric field, the nonlinear scaling of the QCSE is inverted. After identification of the potential half-cycles of one S_{QCSE} trace, multiple, ambiguous polarity assignments are possible, as shown in fig. 4.15. Subsequently, one can recalculate the QCSE signal by applying the phase-shift $\Delta\phi = \phi_2 - \phi_1$ and the nonlinear scaling. Finally, the „true“ underlying electric field is found by minimizing the error between reconstructed and measured $S_{\text{QCSE}}(\phi_2)$. The incorrect, underlying waveforms offer a different amplitude spectrum that can not reproduce the measurement.

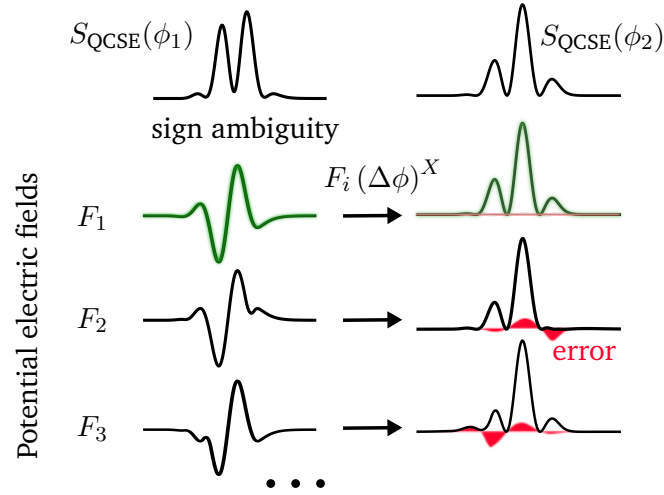


Fig. 4.15: Illustration of the Gouy polarity-reconstruction scheme. Starting from the $S_{\text{QCSE}}(\phi_1)$ multiple potential electric fields F_i can be constructed. The application of the CEP shift $\Delta\phi$ and the nonlinearity X leads to reconstructed $S_{\text{QCSE}}(\phi_2)$ that can be compared to the QCSE trace at ϕ_2 . Whereas F_2 and F_3 lead to a significant difference (red) between these two traces, F_1 matches the measurement and therefore is the underlying electric field.

Reconstruction based on the Hilbert transform

A linear, time-invariant system can be generally described by its transfer function $G_T(\omega)$, consisting of a real part $R(\omega)$ and an imaginary part $X(\omega)$. For an antenna, $G_T(\omega)$ can be calculated from the incident electric field F_{inc} and the antenna shaped field F_{ant} [122]:

$$G_T(\omega) = R(\omega) + iX(\omega) = \frac{F_{\text{ant}}(\omega)}{F_{\text{inc}}(\omega)} \quad (4.1)$$

Starting from the transfer function in the frequency domain, the impulse response of the system $h(t)$ is calculated via Fourier transform [122]:

$$h(t) = \mathcal{F}(G_T(\omega)) \quad (4.2)$$

Assuming causality, the system can only show a response during or after the excitation:

$$h(t) = 0 \quad \text{for } t < 0 \quad (4.3)$$

From this, a connection between the real and the imaginary part of the transfer function can be derived via the Hilbert transform \mathcal{H} [122]:

$$X(\omega) = \mathcal{H}(R(\omega)) = \frac{1}{\pi} \int_{-\infty}^{+\infty} \frac{X(\omega)}{\omega - \Omega} d\Omega \quad (4.4)$$

Thus, the correct antenna response function has to obey this relation. We can obtain the imaginary part of the transfer function $X(\omega)$ in two ways: (a) directly from the transfer function using only the experimental time-domain signals and (b) via the Hilbert transform of the real part of the transfer function $R(\omega)$. By comparing $X(\omega)$ and $\mathcal{H}(R(\omega))$, we can decide which reconstructed waveform fits the incident waveform in the sense of a causal, linear system. Furthermore, this equation builds the basis for the Kramers-Kronig relations that link real and imaginary parts of frequency-dependent material parameters, e.g., the complex permittivity $\varepsilon = \varepsilon' + i\varepsilon''$.

We illustrate this reconstruction strategy for an artificial THz pulse that is shaped by an antenna with a single resonance. Subsequently, we use the correct waveform and a waveform with a flipped half-cycle, representing a wrong polarity assignment, see fig. 4.16. There, we compare the phases $\phi_G = \arctan\left(\frac{X(\omega)}{R(\omega)}\right)$ $\phi_H = \arctan\left(\frac{\mathcal{H}(R(\omega))}{R(\omega)}\right)$, which is equivalent to analyze $X(\omega)$ and $\mathcal{H}(R(\omega))$. Only the correct waveform generates coinciding phases, whereas the incorrect pulse produces a huge mismatch in ϕ_H and ϕ_G . Despite the simplicity of the example, it shows that it is possible to determine the polarity based on the incident waveform.

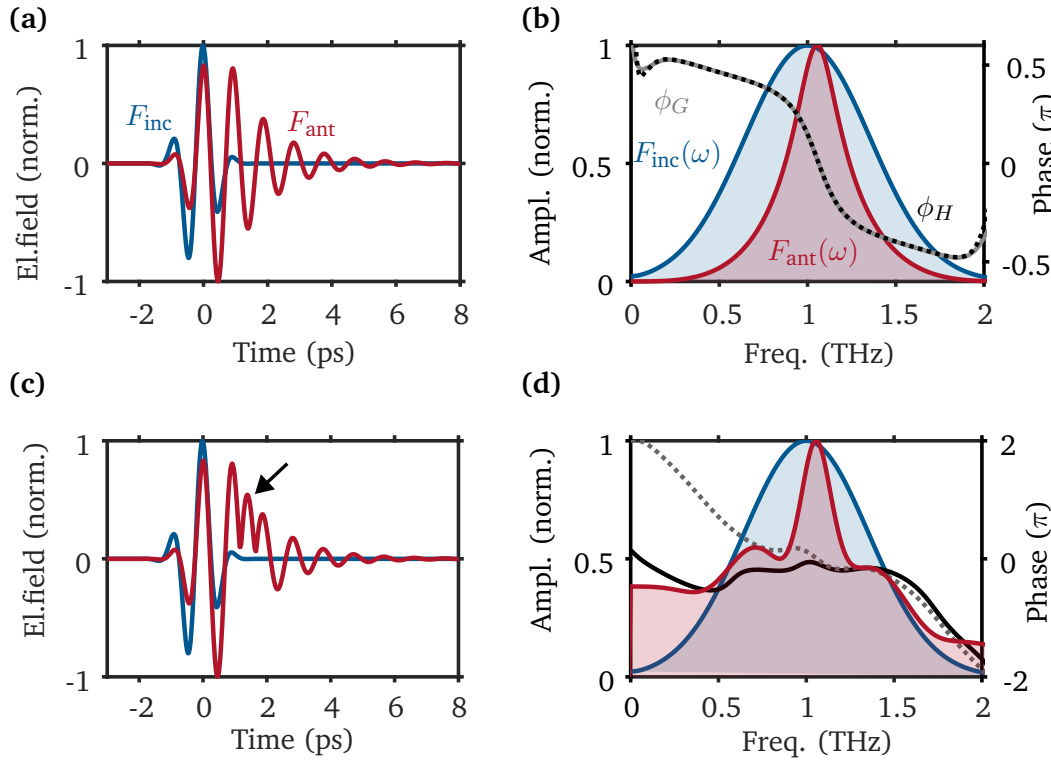


Fig. 4.16: Polarity reconstruction via the Hilbert transform. (a) The incident electric field F_{inc} and the correctly reconstructed antenna signal F_{ant} lead to coinciding phases ϕ_G (gray, dashed) and ϕ_H (black) arising from the transfer function G_T and the Hilbert transform in (b). (c) In contrast, a wrongly assigned polarity (arrow) leads to mismatching phases ϕ_G and ϕ_H in (d), indicating that the antenna field is not linked to the incident waveform via a causal, linear transformation.

Reconstruction with experimental data

Application of the reconstruction schemes to experimental data is practically challenging due to noise and the convolution of the waveforms with sampling pulses of finite duration. This renders the derivation of possible underlying electric fields difficult and error-prone at this stage. In both techniques, a consistent temporal axis in both measurements is crucial. For example, in the Hilbert approach, the incident waveform is measured with EOS at 1030 nm probe wavelength and the QCSE data at around 500 nm in a different OPA setting. This could be circumvented by employing quantum dots that can be probed efficiently at 1030 nm. In general, the use of shorter sampling pulse durations in combination with increased readout sensitivity could facilitate the application of the described schemes.

4.6 Outlook: Ultrafast modulation of quantum dot emission

In sec. 4.3 and 4.4, we presented the QCSE in quantum dots in static and ultrashort electric fields. In principle, the THz pulses can be regarded as quasi-static electric fields during the interaction with the quantum dots. However, taking into account the radiative lifetime of the quantum dots, the emission process cannot be modulated efficiently by picosecond THz pulses. Hence, only the absorption process is modulated – in contrast to the application of static fields, as described in fig. 4.17(a), which enables modulation of the absorption and emission process. In other words, we only detect a QCSE signal when optical and THz pulses overlap temporally. If a fast decay channel on the order of picoseconds exists that can be affected by strong electric fields, also the emission process can be efficiently modulated, as illustrated in fig. 4.17(b).

In quantum dots, fast decay channels open up at high pump fluences or energies due to the creation of multiexcitons generated by hot carriers. In particular, the relaxation of hot charge carriers typically occurs on a femtosecond to picosecond timescale [123]. An overview of the timescales involved in a strongly excited quantum dot is given in fig. 4.18(a). Multiple excitons are generated efficiently for excitation energies of at least twice the bandgap energy of the quantum dot [124]. It can also occur below this limit but requires higher pump fluences to yield multiphoton absorption [125].

The generated excitons decay mostly via non-radiative Auger-recombination on a pico- to nanosecond timescale. There, the energy of the recombination of an electron and hole is transferred to another charger carrier, which is promoted to a higher state [124]. This typically manifests in contributions with short lifetimes in the radiative lifetime curve, as evident in fig. 4.18(b), where we compare the radiative decay for different excitation peak fluences excited with OPA pulses at 480 nm wavelength. The time resolution in this

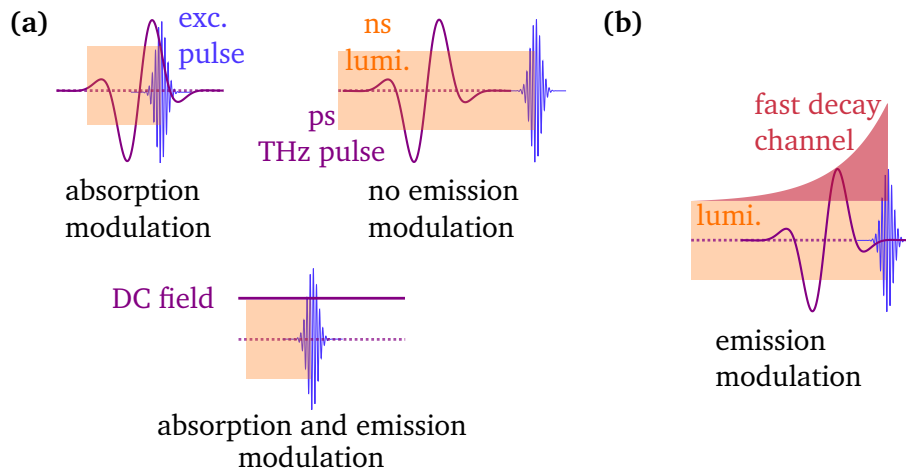


Fig. 4.17: Quantum dot emission and absorption modulation. (a) The absorption process can be modulated with a strong THz pulse with respect to no field (dashed) when optical excitation and THz pulse are temporally overlapping. This leads also to an indirect modulation of the emission process, as shown in the experiments before. Due to the long radiative lifetime (orange), there is effectively no emission modulation. In the case of a static electric field, the absorption and emission processes are both modulated. (b) In the presence of a significant (non-)radiative decay channel (red) with a lifetime comparable to the THz pulse duration, which can be modulated by strong electric fields, direct modulation of the emission can be observed.

measurement is limited to ~ 2 ns, determined by the instrument response function. Thus, potentially faster decays of picoseconds are not resolved.

Introducing a first demonstration of ultrafast THz-modulated emission, we present THz-induced changes in the quantum dot emission for low, medium, and high excitation fluences in fig. 4.18(c). For the lowest excitation fluence, the expected decrease in the emission is observed when the THz pulse is present, attributed to the QCSE. For medium to high peak fluences, however, the emission is increased during and also after the excitation pulse, when the THz pulse interacts with the excited quantum dots. In particular, the waveforms show a complex shape that could arise from the overlap of the QCSE and the increased emission. These two processes occur on different timescales, as the QCSE is quasi-instantaneous and follows the THz electric field, whereas the enhanced emission decays on a timescale of 20 ps, as evident in fig. 4.18(d).

In the literature, intense electric fields have been used to increase luminescence by removing an excess charge from a charged quantum dot [127], which is described as an accumulative effect of the interaction with many THz pulses. In our measurements, the THz pulse also induces an increased luminescence but only in a time window of 20 ps after the strong excitation. Hypothetically, the THz pulse removes a charge before the non-radiative Auger recombination or the relaxation of a hot charge carrier occurs, enabling increased radiative recombination. Auger recombination times down to picoseconds

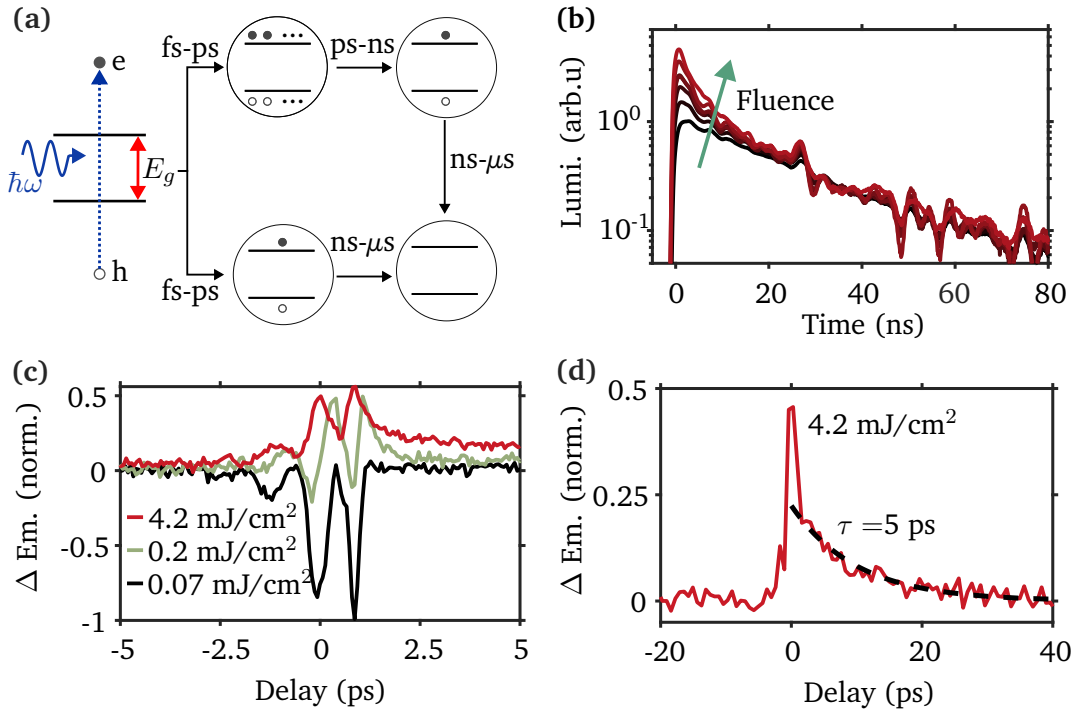


Fig. 4.18: THz enhanced luminescence. (a) A photon with an energy $\hbar\omega > 2E_g$ excites hot carriers in a quantum dot, that can relax in femtoseconds to picoseconds in multiple or single excitons. The multiexcitons recombine mostly via non-radiative Auger recombination in pico- to nanoseconds to single excitons, which decay radiatively on a nano- to microsecond timescale. Adapted from ref. [126]. Timescales taken from ref. [123]. (b) The radiative decay for increasing pump fluences shows an increasing number of short-lived states. Employed peak pump fluences: 0.01 mJ/cm², 0.13 mJ/cm², 0.21 mJ/cm², 0.42 mJ/cm², 0.67 mJ/cm², 1.34 mJ/cm², 4.23 mJ/cm². The curves are scaled to overlap at times larger than 40 ns. (c) Differential emission time-traces for different peak excitation pump fluences. The THz fields are enhanced with a bowtie structure. (d) The increased emission for the highest pump fluence shows a sharp peak at 0 ps delay, which we attribute to the THz QCSE signal, and a decay with a 1/e-lifetime of about 5 ps (dashed line).

have been observed for pairs of multiple electrons and holes in CdSe quantum dots [128]. Comparability to our quantum dots is not fully given, as the exact rates strongly depend on the size of the nanocrystals. In general, the Auger time constant is lower when more electrons and holes are involved [128]. In the experiments, we employed pump energies $E_p = 2.6$ eV only slightly higher than the 1s-exciton absorption at 2.0 eV. In future experiments, higher pump energies are favorable to investigate the influence on the THz-induced emission modulation. However, for a deeper understanding of the involved states, a spectro-temporal mapping of the emission, i.e., with a streak camera with picosecond temporal resolution or transient whitelight absorption in combination with ultrafast THz pulses and strong excitation, could provide complementary insights.

Electro-absorptive detection of terahertz fields by field biasing

The QCSE in quantum dots leads to a change in absorption independent of the external electric field direction. Thus, a direct polarity sensitive readout is not possible, hampering spectroscopic applications. As to date, there exist various field sensitive sampling techniques that resolve the electric field, such as EOS, ABCD and PCA, as detailed in section 2.3. The polar field sampling in low-dimensional structures has been shown so far in (asymmetric) quantum well structures [129, 130]. In this chapter, a new technique based on the QCSE in quantum dots is presented which exploits the breaking of symmetry in the nanocrystals by an additional external electric field with known polarity. Parts of this chapter are published in:

Heindl, M. B., Zhu, H., Bawendi, M. G. & Herink, G. **Electro-absorptive Quantum Dot Antenna Resolves Terahertz Lightwaves via Biased Stark Effect.** *ACS Photonics* **11**, 13-17 (2024)

Figures are adapted with permission. Copyright 2024 American Chemical Society.

5.1 Concept of biased QCSE

Derivation of linear field detection

The idea of detecting polarity with the unpolar QCSE in quantum dots relies on applying an additional external field with known direction to the THz electric field. In fact, a particular feature of the QCSE is employed: the quadratic scaling of the differential absorption signal S_{QCSE} with the electric field. S_{QCSE} is obtained from the difference between absorption with (S_{THz}) and without (S_0) THz field. In order to establish a measure that detects signals linear in the electric field, the nonlinear scaling is derived by differential detection upon modulation of the THz field F_{THz} with an external bias F_{bias} . Therefore, the new observable S_{Δ} is obtained for a bias modulation between 0 and F_{bias} :

$$\begin{aligned}
 S_{\Delta} &\propto S_{\text{QCSE}}(F_{\text{THz}} + F_{\text{bias}}) - S_{\text{QCSE}}(F_{\text{THz}}) \\
 &\propto (F_{\text{THz}} + F_{\text{bias}})^2 - (F_{\text{THz}})^2 \\
 &\propto 2F_{\text{THz}}F_{\text{bias}} + F_{\text{bias}}^2
 \end{aligned} \tag{5.1}$$

Since F_{bias} has a constant value, the second part of the last equation will appear as a constant offset that we subtract in all data, finally providing a signal that is proportional to the THz electric field and consequently also detects the field polarity. Furthermore, the ratio of $2F_{\text{THz}}F_{\text{bias}}$ and the offset F_{bias}^2 can be used to determine the THz electric field strength, if the bias field in the quantum dots is known. The signal can be increased by a factor of two via modulation between $-F_{\text{bias}}$ and $+F_{\text{bias}}$, finally leading to $S_{\Delta} \propto 4F_{\text{THz}}F_{\text{bias}}$. The derivation of a polar signal from a unipolar mechanism is also described in fig. 5.1, highlighting the fact, that the differential bias effectively gives the derivative of the underlying QCSE scaling.

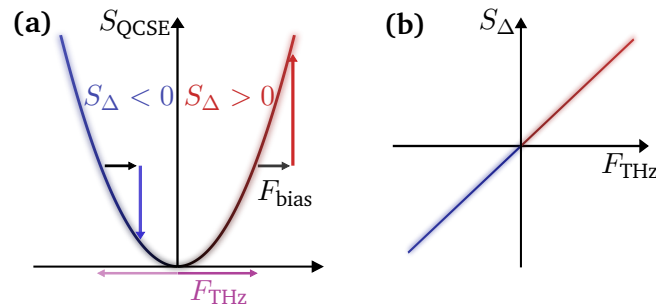


Fig. 5.1: Principle of polarity sensitive detection with quantum dots. (a) The QCSE in quantum dots shows a nonlinear scaling with the absolute value of the electric field. A positive bias leads to a higher/lower signal for positive/negative THz fields, thus, the differential signal S_{Δ} for bias on and off is polarity sensitive. (b) The derived signal S_{Δ} provides a polarity sensitive signal proportional to the electric field in case of $S_{\text{QCSE}} \propto F^2$, because the differential detection with and without bias practically leads to a derivative of the underlying scaling. Here, the offset arising from the bias field itself has been removed.

Experimental realization of the electro-absorptive antenna

The electric field bias is implemented by applying a voltage across a gap in a gold structure, or in other words to a small capacitor. The implementation as well as the development of the THz waveform from the unipolar signal is illustrated in fig. 5.2(a,b). The employed CdSe-CdS core-shell quantum dots consist of a CdSe-core of 3.7 nm diameter and a CdS shell of 2.2 nm radius and are fabricated by Hua Zhu in the group of Prof. Mounqi G. Bawendi (Massachusetts Institute of Technology). The absorption and emission spectra are shown in fig. 5.2(c). The nanocrystals are deposited via drop-casting on top of the gold structure, which consists of interdigitated electrodes with gold strips of $10\mu\text{m}$ separated by $10\mu\text{m}$ on top of a quartz glass substrate. The electrodes are contacted with conductive silver lacquer to copper wires. A photograph of the whole structure is shown in fig. 5.2(d). We modulate the bias field using a function generator (square wave, typical frequency $f_{\text{mod.}} = 220\text{ Hz}$) and a voltage supply with up to $U_{\text{bias}} = 60\text{ V}$ that drive a voltage switch, delivering a modulated voltage between 0 V and U_{bias} at $f_{\text{mod.}}$

In contrast to measurements of S_{QCSE} , here, the THz beam is not modulated. We measure absorption changes for bias on and off with a pair of balanced photodiodes, a boxcar averager and a lockin-amplifier set to the modulation frequency f_{mod} , as described earlier in section 3.3. The sampling pulse with a wavelength of 480 nm is focused in between two gold electrodes and delayed with respect to the THz pulse to sample its waveform. The employed THz pulses are polarized perpendicular to the electrode gap and exhibit an incident peak field of about 400 kV cm^{-1} , which can be varied by a wire-grid polarizer. Typically, two wire-grid polarizers are employed to preserve the polarization of the attenuated beam, but, here, the electrode structure acts as a second wire-grid polarizer.

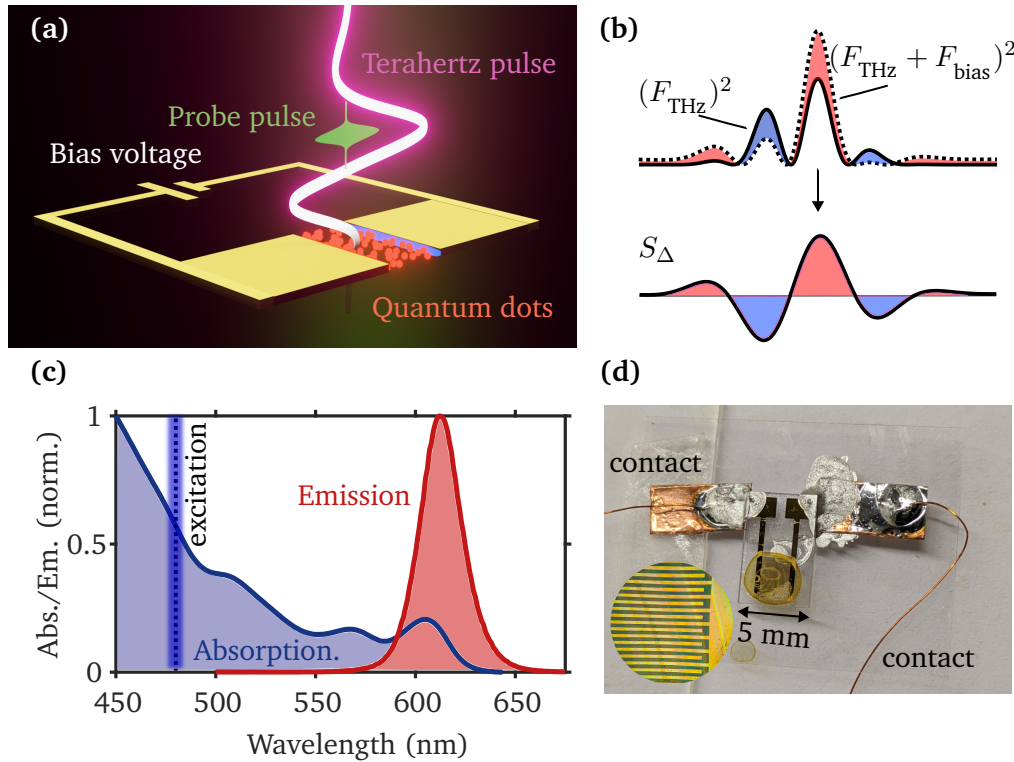


Fig. 5.2: Quantum dot THz antenna based on electro-absorptive detection. (a) A strong THz pulse impinges a gold structure with quantum dots in between the electrodes. The electric field in the gap generated by the applied voltage creates the bias electric field F_{bias} parallel to the THz field. In order to derive the polar THz waveform, the differential absorption in the quantum dots with and without bias field S_{Δ} is detected with an ultrafast probe pulse as a function of the temporal delay between THz pump and optical probe pulse. (b) The bias field enhances (red area) or reduces (blue area) the THz-induced unipolar QCSE signal, depending on its polarity with respect to the bias field direction. In case of a quadratic dependence of S_{QCSE} from the electric field, the difference signal S_{Δ} delivers, apart from a constant offset, the polar THz waveform. (c) Absorption (blue) and emission (red) spectra of the employed quantum dots along with the excitation wavelength of 480 nm. This data has been acquired by Hua Zhu. (d) Photograph of the quantum dot antenna. The electrodes are contacted to copper wires using silver lacquer and a copper patch. The inset shows the gold microstructure, with metallic bars separated by $10 \mu\text{m}$.

5.2 Electro-absorptive THz sampling using quantum dots

Field enhancement in the antenna

Given the dimensions of the electrode structure, we simulate the THz electric field in the gaps using the approach described in section 3.1. The average field enhancement inside the gaps, without substrate, is given by $P/w = 20\ \mu\text{m}/10\ \mu\text{m} = 2$. The simulated electric field enhancement, using a refractive index for the quartz substrate of $n = 2$ [131] and gold height of 150 nm, is provided in fig. 5.3(a) with a mean intra-gap enhancement of 1.3. This factor leads to a mean peak field strength of $520\ \text{kV cm}^{-1}$ in the experiment. From the simulated incident and enhanced electric field waveform, we calculate the frequency-dependent enhancement, provided in fig. 5.3(b), that shows a nearly constant enhancement for frequencies between 0 and 4 THz, relevant for the typical incident THz pulse employed in this work.

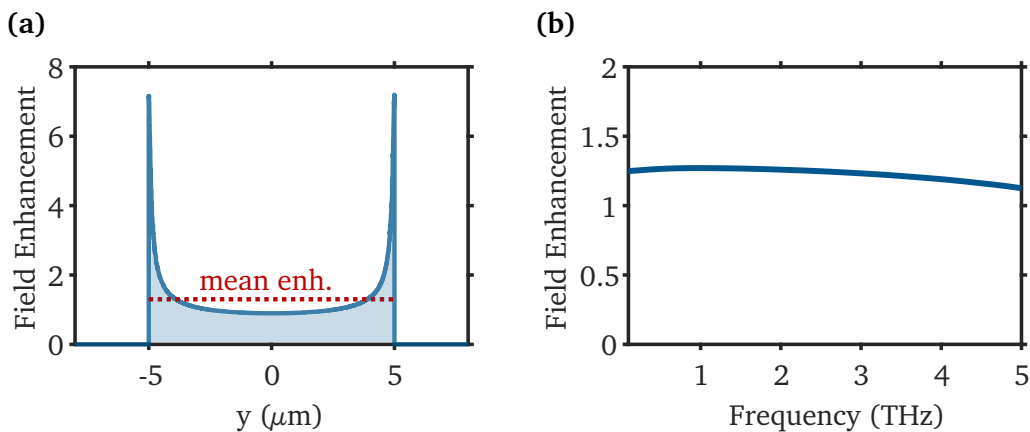


Fig. 5.3: THz field enhancement factor in the electrode structure. (a) The simulated field enhancement factor has a mean value of 1.3. (b) The spectral enhancement factor is nearly constant in the relevant frequency range between 0 and 4 THz.

Sampling pulse duration limited detection bandwidth

The frequency bandwidth for temporal sampling techniques depends on the temporal duration of the sampling pulse and its corresponding frequency bandwidth, as described in section 2.5. Therefore, we determine the pulse lengths at the two wavelengths relevant for EOS and QCSE, 1030 nm and 480 nm, using a home-built collinear, interferometric auto-correlator. In particular, we employ two-photon absorption in photodiodes with bandgaps larger than the respective energy of the pulses (1030 nm: G5645, *Hamamatsu*; 480 nm: JEA0.1S, *Laser Components*) to enable nonlinear detection of the pulse pairs, necessary

for the determination of pulse durations. The temporal delay between the two arms of the interferometer is generated using a mirror attached to a shaking audio speaker driven at a few Hz in one arm. We detect the nonlinear autocorrelations using an oscilloscope triggered to the speaker frequency. Finally, the central frequency of the incident pulses are used to calculate the temporal separation of the fringes in the autocorrelation and, thus, the temporal axis. The resulting interferometric autocorrelations (IAC) are provided in fig. 5.4(a,b). Typically, one expects ideally a peak-to-background ratio of 8 : 1, that is experimentally higher in the case of 1030 nm, which we attribute to a small amount of three-photon-absorption, which would lead to a ratio of 32 : 1 [132]. We Fourier filter the spectral parts around frequency zero to obtain the intensity autocorrelation. The intensity pulse duration is then determined by its $1/e^2$ -width divided by a factor of $\sqrt{2}$, assuming a Gaussian pulse shape [132]. The analysis yields pulse durations of (150 ± 10) fs for 1030 nm and (240 ± 10) fs for 480 nm, hence a higher accessible bandwidth for the 1030 nm pulse, as evident in the calculated spectral transfer function G for the two pulses in fig. 5.4(c) following eq. (2.23). In particular, the $1/e^2$ frequency bandwidth is approximately 5 THz for 480 nm and 8 THz for 1030 nm.

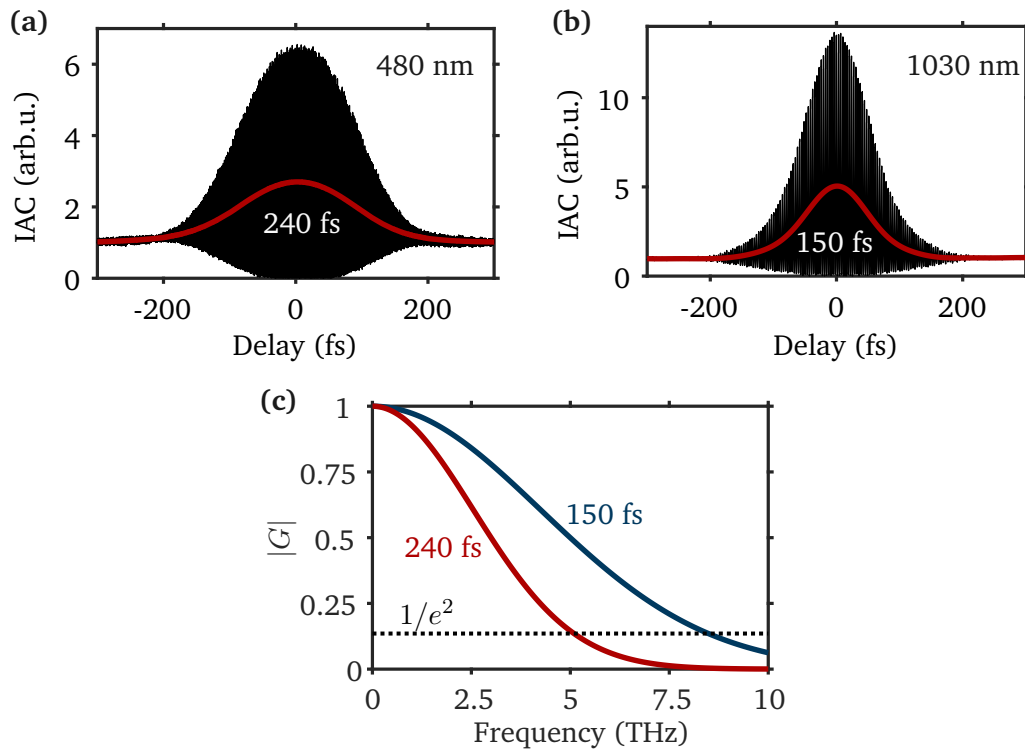


Fig. 5.4: Sampling pulse duration and resulting bandwidth. (a) Interferometric, nonlinear autocorrelation (IAC) (black) for the pulses at 480 nm, along with the extracted intensity autocorrelation (red) yielding a $1/e^2$ -pulse duration of approx. 240 fs. (b) IAC for the pulses 1030 nm in the same format as (a) showing a pulse duration of approx. 150 fs. (c) The spectral transfer function in the sampling process for the two pulse durations.

Comparison to conventional electro-optical sampling

First, we benchmark our newly developed technique against conventional EOS. The THz waveforms measured with the two techniques provide comparable results as well as the amplitude spectra, see fig. 5.5. In the time trace, the THz pulse measured with EOS appears slightly shorter, which is also evident in the broader spectrum compared to the quantum dot measurement. We attribute the deviations mostly to the different sampling pulse durations, which provide therefore different accessible bandwidths. To underline this, we study the ratio of the Fourier amplitudes in fig. 5.5(b), which shows a roll-off at higher frequencies, attributed to the longer pulse duration involved in the quantum dot measurement. Additionally, the underlying unbiased signal in fig. 5.5(c), where we modulated the THz beam, shows the unipolar trace that originates from the nonlinear scaling of the QCSE.

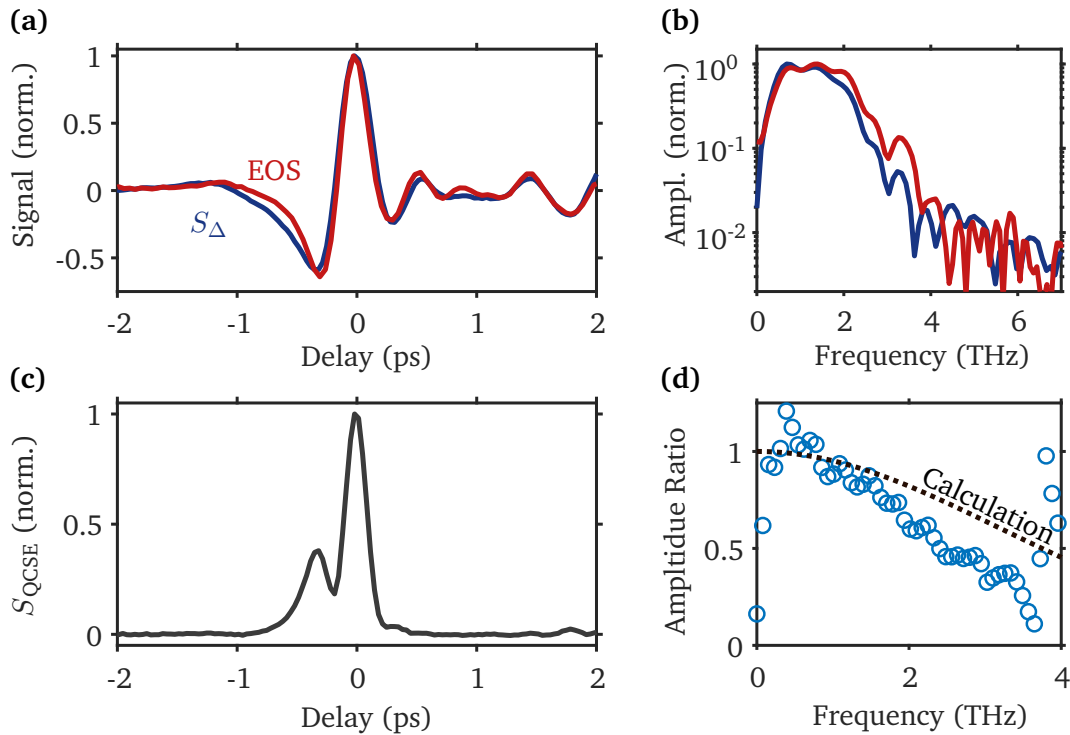


Fig. 5.5: Electro-absorptive sampling of a THz pulse in comparison to electro-optical sampling. (a) The S_{Δ} -trace (blue) shows high agreement with the THz waveform, detected via EOS (red). Notably, we added a CEP-shift of 0.1π to the EOS data due to the uncertainty in the exact focus position and removed a constant offset in the S_{Δ} -curve, arising from the bias electric field. (b) The corresponding amplitude spectra show for the EOS data a slightly broader bandwidth of the pulse compared to the quantum-dot antenna. (c) The unbiased QCSE-trace shows only the unipolar signal and suppresses, due to the quadratic scaling, the smaller features. (d) The ratio of the amplitude spectra of S_{Δ} and EOS (blue circles) illustrate the higher bandwidth for the EOS measurement. We attribute this mostly to the different sampling pulse durations, as the ratio of the spectral amplitude transfer functions (dotted) for the two pulse durations shows a comparable behavior.

Scaling behavior of the quantum dot antenna

Now, we study the involved signals as a function of the bias and THz field. The underlying signal S_{QCSE} for varying F_{bias} and F_{THz} is shown in fig. 5.6(a,b) in a double-logarithmic representation and a linear fit provides essentially the required quadratic scaling with the field strength. Hence, we expect a linear scaling of the differential QCSE signal S_{Δ} with the bias field, following eq. (5.1). Therefore, we vary F_{bias} at the THz peak field and detect S_{Δ} , see fig. 5.6(c), yielding a linear dependency. Finally, we study S_{Δ} for different THz peak field strengths for two cases: F_{bias} and F_{THz} pointing in the same and in the opposite direction, see fig. 5.6(d). Both measurements provide a signal that scales linearly with the THz field, as we require for the linear field sampling. In the first case, the fields add up and result in an effective higher field, that leads to a saturation in the signal. This effect is mitigated in the opposite case due to the lower field. We attribute this behavior to the saturation of the QCSE, that we already describe in our quantitative 1d model in section 4.2.

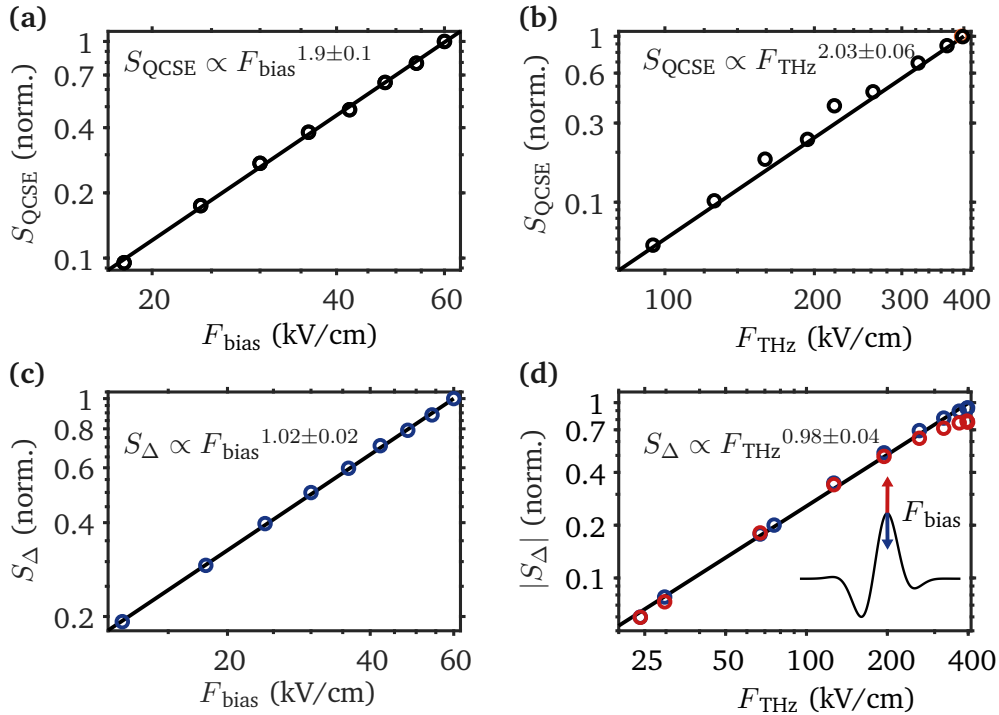


Fig. 5.6: Field scaling behavior of S_{Δ} and S_{QCSE} (a,b) The absorption modulation due to the QCSE is shown as a function of bias and THz field in a double-logarithmic representation. Evident from a linear fit (black line), both curves scale with the respective field strength. The exact results are provided in the upper corners of the figures and the error is given by the 95% confidence interval of the linear fit. (c) S_{Δ} at the THz peak field scales linearly with the bias field. (d) Our key observable S_{Δ} for varying THz field strengths regarding two cases: the bias field increases/decreases the total field (red/blue). Both curves show initially a linear scaling, but a saturation in the high field case above 200 kV cm^{-1} is observed, attributed to saturation in the QCSE.

Due to the derivative character of S_{Δ} , the saturation of S_{QCSE} is translated in a pronounced saturation and subsequent roll-off of the linear field signal with increasing field, as we showcase in the generic simulated scaling curves in fig. 5.7(a). We use the lowest transition to study the QCSE signal, using the size of core and shell and a quasi-type II band alignment. In particular, we reproduce the saturation by calculating the S_{Δ} curve from the simulation using the two different bias field directions, yielding the linear curve, that saturates earlier fields for the adding-up fields. In detail, we use a bias field $F_{\text{bias}} = \pm 40 \text{ kV cm}^{-1} = \pm 0.05 F_{\text{THz}}^{\text{max}}$. Similarly, the linearity of the S_{Δ} signal as a function of the bias field is also affected by the saturation, as the threshold is given by the total electric field, see fig. 5.7(b).

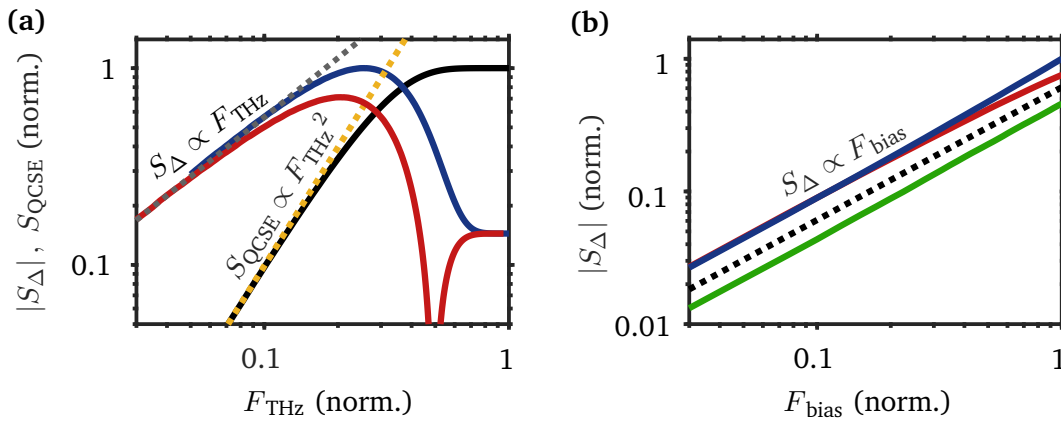


Fig. 5.7: Simulation of the QCSE saturation influence. (a) S_{QCSE} scales initially quadratic and saturates at high fields. From this, we calculate the S_{Δ} scaling for the two bias directions, yielding the blue and red curve, showcasing the earlier onset of saturation in the case of same field direction of THz and bias field (red). The dashed lines indicate linear (gray) and quadratic scaling (yellow) with the THz field. (b) S_{Δ} for varying bias fields in the linear (green, $F_{\text{THz}} = 0.075$) and saturation ($F_{\text{THz}} = 0.2$) regime shows linear scaling (dashed) and only small influence of the saturation. The red and blue curve represent the two bias field directions.

We further examine the influence of the direction of the bias field in fig. 5.8(a), comparing the THz waveforms for both bias directions. The waveforms are mirrored on the x-axis but show similar form, despite a lower peak signal in the case of parallel THz and bias field, due to the aforementioned saturation in the QCSE. Exemplary, we correct this nonlinear response at the highest field by applying the inverted scaling curve, see fig. 5.8(b), reverting the saturation.

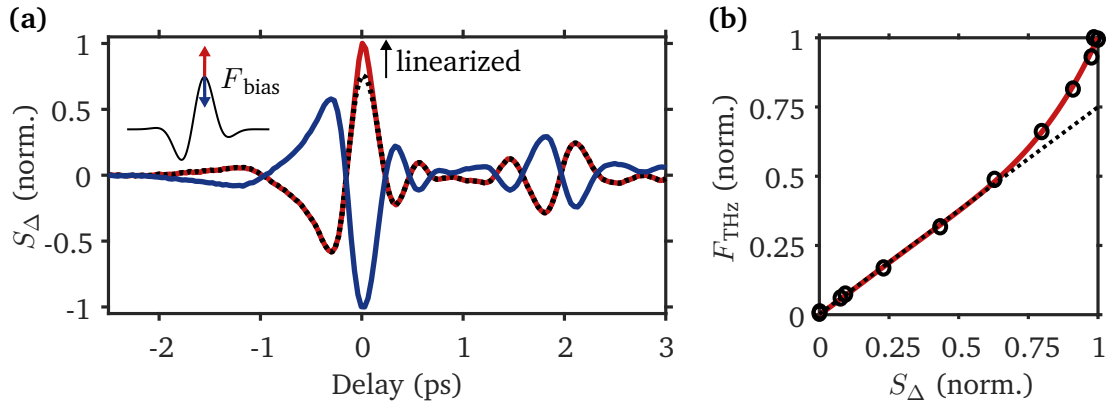


Fig. 5.8: THz waveforms for the different bias field directions (a) The measured S_{Δ} -curves for the two bias field polarities show mirrored but similar behavior. The color coding follows fig. 5.6(d). In particular, we corrected the saturation observed in the case of adding-up fields (dashed line) using the scaling curve from fig. 5.6(d). (b) The inverted scaling curve is fitted using a 4th-order polynomial (red) to provide a continuous function for the linearization. The dashed line illustrates a linear scaling.

5.3 First spectroscopic application of the quantum dot antenna

We now show proof-of-principle spectroscopic application of the quantum dot antenna by measuring the THz transmission through two straightforward samples: water vapor at ambient conditions and a HR-Si wafer.

Terahertz absorption in water vapor

Rotational transitions in water vapor lead to a large number of absorption lines in the THz transmission spectrum [133], and result in characteristic, oscillatory decays after the THz pulse in the time-domain signals. We reduce the humidity in the THz beam path using a box purged with dry air. The sampled THz waveforms after trespassing 15 cm of air in fig. 5.9(a) show reduced oscillations after the pulse for 8% humidity compared to 45%. The corresponding Fourier spectra in fig. 5.9(b) show sharp absorption lines for ambient conditions that are attenuated for the purged measurement. In particular, the comparison with reference data from the HITRAN database verifies the spectral positions of the absorption lines [134]. The spectral resolution of the antenna measurement is 0.1 THz, given by the inverse of the temporal delay range. We can assign the absorption lines to the reference data beyond 3 THz. From the spectrum above 5 THz, we can estimate the signal-to-noise ratio to ≈ 100 .

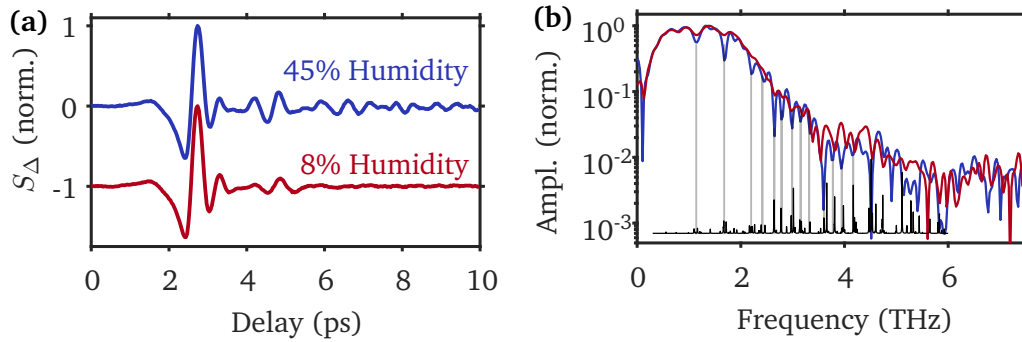


Fig. 5.9: Spectroscopy of water vapor using the biased QCSE. (a) The THz waveform after passing through air at 45% humidity shows oscillations after the pulse originating from rotational and transitions in water vapor molecules. By reducing the humidity, the oscillations are reduced. (b) The spectra for the humid air show characteristic absorption lines compared to the purged measurement. The observed lines are in agreement with the HITRAN reference dataset, which is shown in a linear fashion at the bottom.

Silicon transmission

The sampling traces with and without a HR-Si wafer are shown in fig. 5.10(a). Beside the temporally shifted pulse for the sample trace, also the peak field is reduced to about 70 %, which is also evident in the spectral amplitudes in fig. 5.10(b), where we also show the spectral amplitude ratio. Generally, the amplitude transmission coefficient through a thick sample is given by $T = \frac{4n_1n_2}{(n_1+n_2)^2}$, using the refractive index of the sample n_2 and the surrounding medium n_1 [135]. Using the refractive indices of HR-Si $n_2 = 3.4$ [131] and air $n_1 = 1$, 70 % transmission is calculated, as observed in the experiment. Using the temporal delay $\Delta\tau_{\text{Si}} = 1.9$ ps and the thickness of the wafer of $d = 240 \mu\text{m}$, measured with a caliper, we can exemplarily calculate the (frequency-averaged) refractive index to $\frac{\Delta\tau_{\text{Si}} \cdot c}{d} + 1 \approx 3.4$.

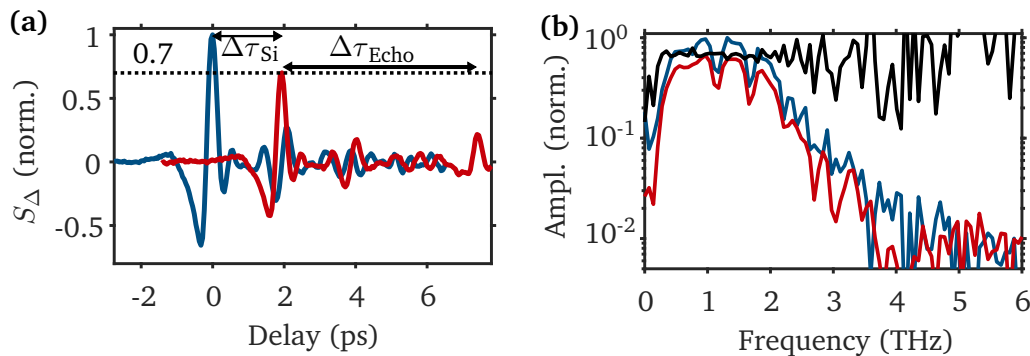


Fig. 5.10: THz waveform transmitted through a silicon wafer measured with the quantum dot antenna. (a) The THz waveform (blue) is lowered by 30% after transmission through a HR-Si wafer (red). The peak of the transmitted pulse appears delayed by $\Delta\tau_{\text{Si}} = 1.9$ ps as well as an echo delayed by $\Delta\tau_{\text{Echo}} = 5.5$ ps originating from reflections in the wafer. (b) The corresponding spectra show a frequency independent attenuation of the pulse, as evident from the ratio of the amplitudes (black) showing 70 % transmission.

5.4 Summary & outlook

In conclusion, our new detection technique based on the quadratic scaling of the QCSE is able to detect polar THz waveforms by introducing an external bias field as a reference direction. Experimentally, the signal readout is straightforward, compared to e.g. the rather delicate conventional EOS. Also, one can easily adapt the employed quantum dots to the sampling wavelength by tuning their size. We expect further improvements on the antenna performance by optimizing the readout wavelength and pulse duration, leading to a higher sensitivity and bandwidth. Limits in the bandwidth of the QCSE have not yet been fully explored and recent studies suggest that this effect can also occur in the mid-infrared region [136]. Additionally, the maximal bias voltage in this study is technically limited by the employed voltage source. Additionally, an increased signal strength by a factor of two is given by a modulation between $-F_{\text{bias}}$ and F_{bias} . In case of saturation in the QCSE, an optimal bias field strength that maximizes the signal can be found, see ref. [137]. In particular, absolute THz field strength calibration is feasible upon knowledge of the exact field attenuation in the quantum dot layer. Here, we only detect the THz field components parallel to the bias field – using a quadrant electrode structure also polarimetry [21] is within sight.

Quantum-Probe Field Microscopy

Quantum dots offer high photostability, flexibility, and quantum yield that make them ideal for imaging applications [138]. Moreover, the nanocrystals have been successfully applied to super-resolution techniques with resolutions beyond the diffraction limit [139]. Recently, field-induced quantum dot luminescence has been used to image pulsed THz radiation [140, 141]. However, their scheme does not allow for temporal sampling of the THz waveform in contrast to the QCSE. As a logical step, we combined the imaging capabilities of the quantum dots with the field sensitivity of the QCSE. Based on this, we developed a new technique for imaging of THz near-fields based on the QCSE in quantum dots that offers sub-cycle temporal and sub-diffraction limited spatial resolution. As the nanocrystals act as field-sensitive quantum probes, we called our method Quantum-Probe Field Microscopy (QFIM).

Regarding the diameter of the employed quantum dots of about 10 nm, they are ideal to act as local THz near-field sensors. Specifically, the (reactive) near-field of a short antenna is defined as the region with radius $\frac{\lambda_{\text{ant}}}{2\pi}$ using the antenna wavelength λ_{ant} [142]. Thus, the near-field around an antenna resonant at 1 THz can be observed within a distance of 50 μm . Therefore, the quantum dots are sufficiently small to spatially resolve the near-field with the QCSE.

Parts of this chapter are published in:

Heindl, M. B., Kirkwood, N., Lauster, T., Lang, J. A., Retsch, M., Mulvaney, P., Herink, G.
Ultrafast Imaging of Terahertz Electric Waveforms Using Quantum Dots. *Light: Science & Applications* **11**, 5 (2022)

Figures are adapted with permission from the journal.

6.1 Experimental realization of an ultrafast field microscope based on quantum dots

The experimental setup is based on the ultrafast field-induced changes in the absorption of quantum dots. Here, we focus specifically on the imaging of these changes in the emission. This is realized by expanding the earlier described setup with conventional fluorescence imaging, employing a cooled CCD-camera and a microscope objective, see fig. 6.1. This enables imaging of terahertz near-fields by detection of far-field luminescence of the quantum dots. A widefield illumination in the focus of the THz beam is ensured with an additional widefield lens in the OPA beam path. The OPA was tuned to either 480 nm or 530 nm to excite the emission of the CdSe-CdS core-shell quantum dots at 645 nm. Details on the quantum dots are presented in section 4.1. The fluorescence of the quantum dots is collected with the objective, and light at the excitation wavelength is filtered. In particular, we image differential emission using a mechanical chopper in the THz pump beam path. Femtosecond temporal resolution is implemented with a mechanical delay stage in the pump beam path in order to sample the phase-stable terahertz fields. For further experimental details concerning the readout and employed components, see section 3.3.

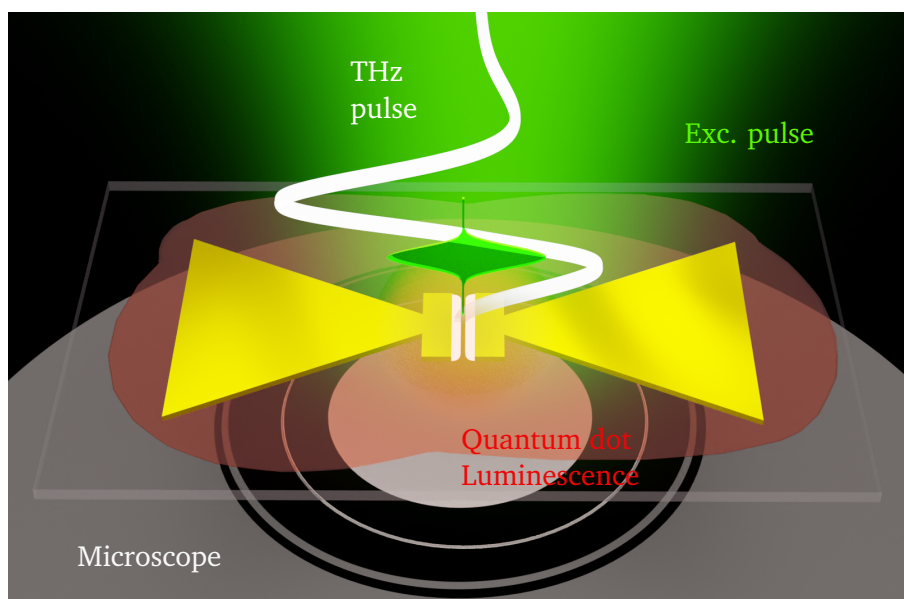


Fig. 6.1: Scheme of Quantum-Probe Field Microscopy. Changes in the emission of quantum dots due to strong, enhanced THz fields are imaged by collecting the modulated fluorescence with a microscope objective and a camera. Sub-cycle temporal resolution is provided by a short femtosecond probe pulse that excites the quantum dot luminescence.

6.2 Imaging of ultrafast terahertz field evolutions in a bowtie antenna

First, we apply QFIM to a single bowtie antenna – a structure broadly used for, e.g., detection and broadband enhancement of terahertz radiation. The antenna design and the resulting gold structure, fabricated with optical lithography, are shown in fig. 6.2. Additionally, a fluorescence image of the area close to the bowtie gap is provided. The polarization of the THz beam is aligned perpendicular to the gap of the bowtie to ensure a high field enhancement. We capture multiple snapshots of changes in the emission with a temporal separation $\Delta\tau = 30$ fs. For each timestep, a total of 50 pairs with THz radiation on and off are acquired, that we use to generate differential images using software. From the whole series, 15 representative QFIM images are displayed in fig. 6.3, revealing three rectified half-cycles of the underlying electric field.

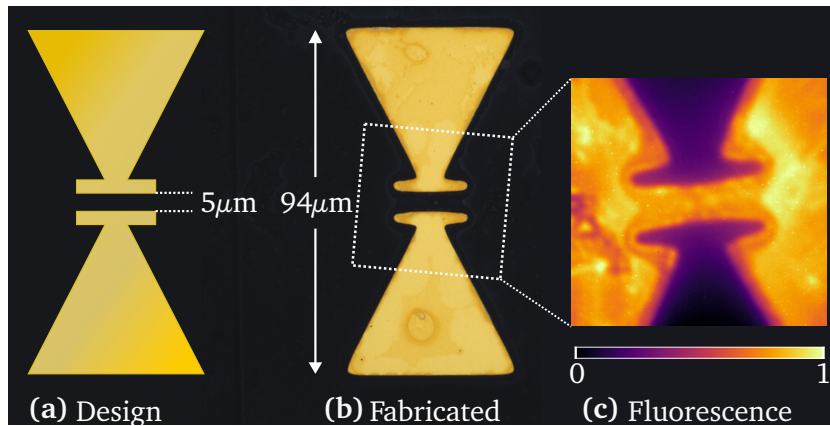


Fig. 6.2: Terahertz bowtie antenna. (a,b) Design template and optical photograph of the fabricated bowtie gold antenna with a $5\ \mu\text{m}$ gap. (c) Fluorescence microscope image of the dotted area in (b).

The characteristic field enhancement pattern of the bowtie antenna is imprinted in the QFIM images, as evident in fig. 6.4(a,b), where we compare the QFIM image at the peak signal with a finite-element simulation of the structure, demonstrating the capability of our method to image electric near-fields. Here, 1000 image pairs are used to generate the differential image. The peak field in the gap is estimated from the time-transient simulation to about $7\ \text{MV cm}^{-1}$ using the incident peak field strength of $400\ \text{kV cm}^{-1}$. The changes in the emission intensity arise from modulated absorption in the quantum dot, as described earlier in this thesis. We underline this by measuring the differential transmission $\Delta\text{Trans.}$ of the optical excitation pulse at the peak THz near-field, showing an inverted, complementary pattern to the QFIM data, see fig. 6.4(c). Thus, besides the imaging of intensity, changes in the absorption can also be utilized to study the near-field.

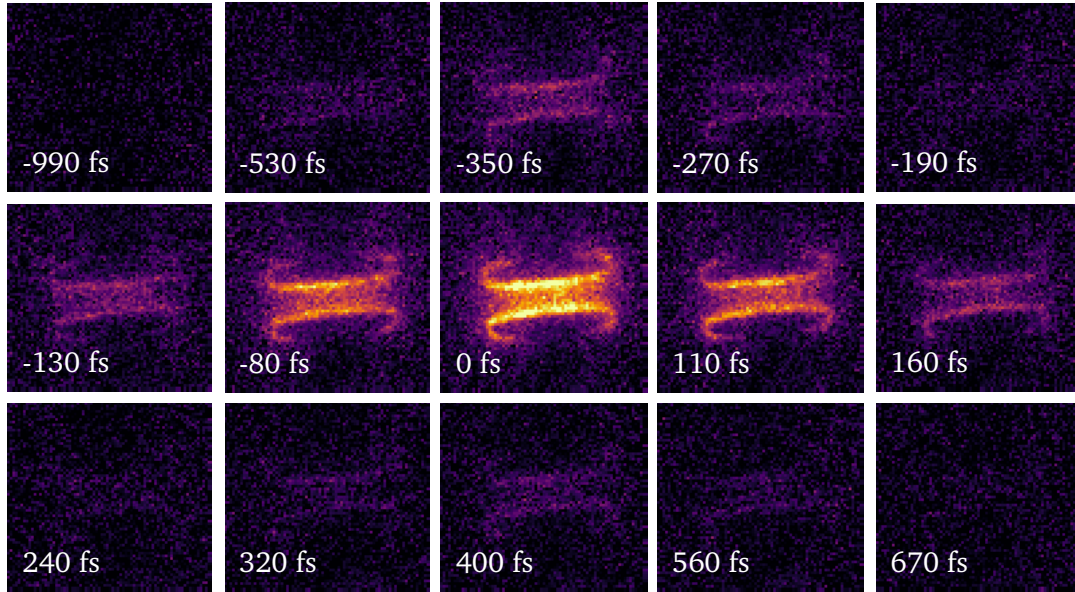


Fig. 6.3: QFIM of the ultrafast electric near-field in the bowtie. 15 exemplary QFIM snapshots with the temporal delay between optical and THz pulse set to 0 fs at the highest signal. Three peaks at $\Delta\tau = -350$ fs, 0 fs and 400 fs are apparent, showing all the same spatial pattern.

The spatial resolution of our technique profits from the detection of visible fluorescence, which offers a much lower wavelength than the investigated THz radiation and thus provides a substantially better achievable optical resolution. At a frequency of $f_{\text{THz}} = 1$ THz, corresponding to a wavelength of $\lambda_{\text{THz}} = 300 \mu\text{m}$, the Abbe diffraction limit is approximately $\frac{\lambda_{\text{THz}}}{2} = 150 \mu\text{m}$, using a numerical aperture equal to 1 [143]. The spatial resolution of QFIM in this measurement is discussed in fig. 6.4(d), showing a resolution of $2 \mu\text{m}$, thus offering a far sub-diffraction limited resolution with regard to the THz regime.

In particular, we also investigate the field enhancement pattern in the bowtie for THz polarization approximately parallel to the bowtie gap. For this purpose, we took a QFIM image at the peak field, see fig. 6.5(a). The highest signal is observed at the outer edges of the bars, and a slight tilt angle of the bowtie with respect to the THz polarization translates into an asymmetric pattern. We compare this to a finite element simulation in fig. 6.5(b), verifying the experimental finding also with regard to the slight asymmetry in the enhancement.

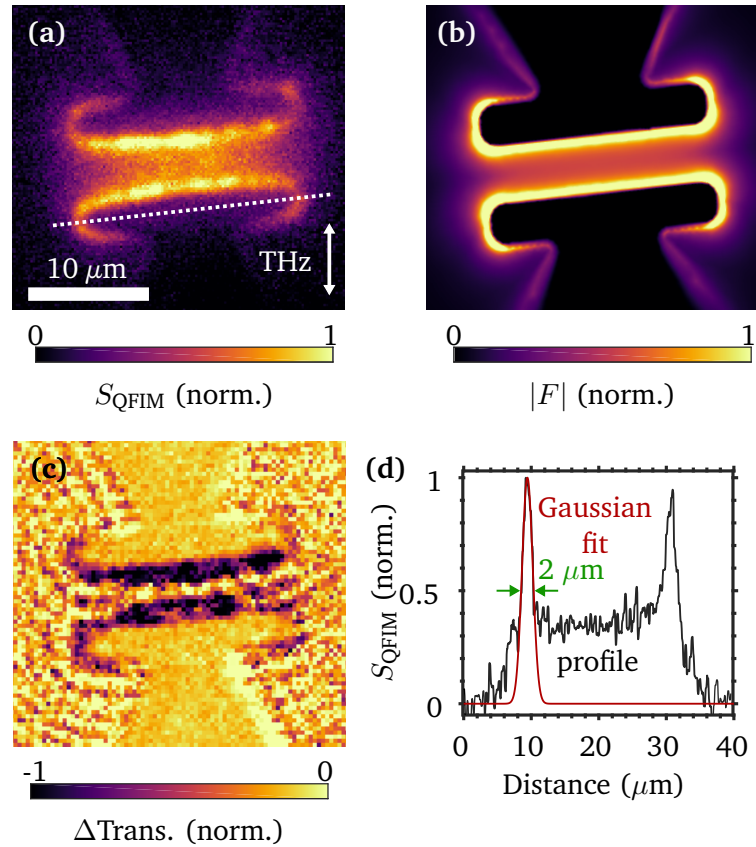


Fig. 6.4: QFIM image detected in emission and absorption compared to simulation.

(a) High-resolution QFIM image in the bowtie at the peak signal. (b) The absolute value of the simulated in-plane electric field in the antenna shows a similar pattern to the QFIM data, highlighting the field sensitivity in the presented scheme. Here, we used the time-transient technique described in section 3.1. (c) The transient transmission image directly maps differences in the absorption of the quantum dots and, thus, provides an inverted but matching dataset to (a), which detects changes in the emission. (d) The resolution of the dataset is estimated using the cut-line in (a) (white, dashed) yielding the profile (black). From a Gaussian fit (red), we determine the FWHM to $2 \mu\text{m}$, far beyond the diffraction limit of the THz radiation.

Besides studying the spatial field distribution, we also investigate the temporal evolution of the electric field in the gap. Therefore, we average the signal from the QFIM video inside the bowtie gap, leading to fig. 6.6(a), showing the three half-cycles of the electric field. The direct extraction of the underlying electric field is non-trivial, as the signal is rectified, nonlinearly scaled, and convoluted with the non-finite sampling pulse duration. Firstly, the scaling of the QFIM signal is studied by variation of the incident field strength and the detection of the fluorescence with a PMT. Here, we detune the THz generation process leading to lower field strengths and obtain the traces in fig. 6.7. In particular, the expected quadratic scaling of the QFIM signal with the electric field is also observed in this dataset, showing a close to quadratic scaling.

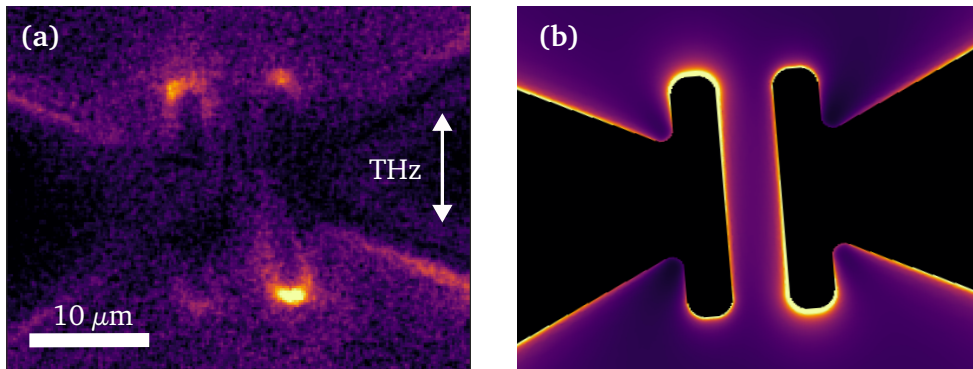


Fig. 6.5: QFIM image for the rotated bowtie antenna. (a) The QFIM image for THz polarization parallel to the gap provides practically no signal in the gap but at the edges of the bars. A small offset in the antenna rotation of about 6° leads to an asymmetric field pattern. (b) The simulated electric field distribution in the tilted bowtie provides a similar asymmetric pattern. This simulation has been done by Julia A. Lang using a finite-element solver (COMSOL multiphysics) in the frequency domain.

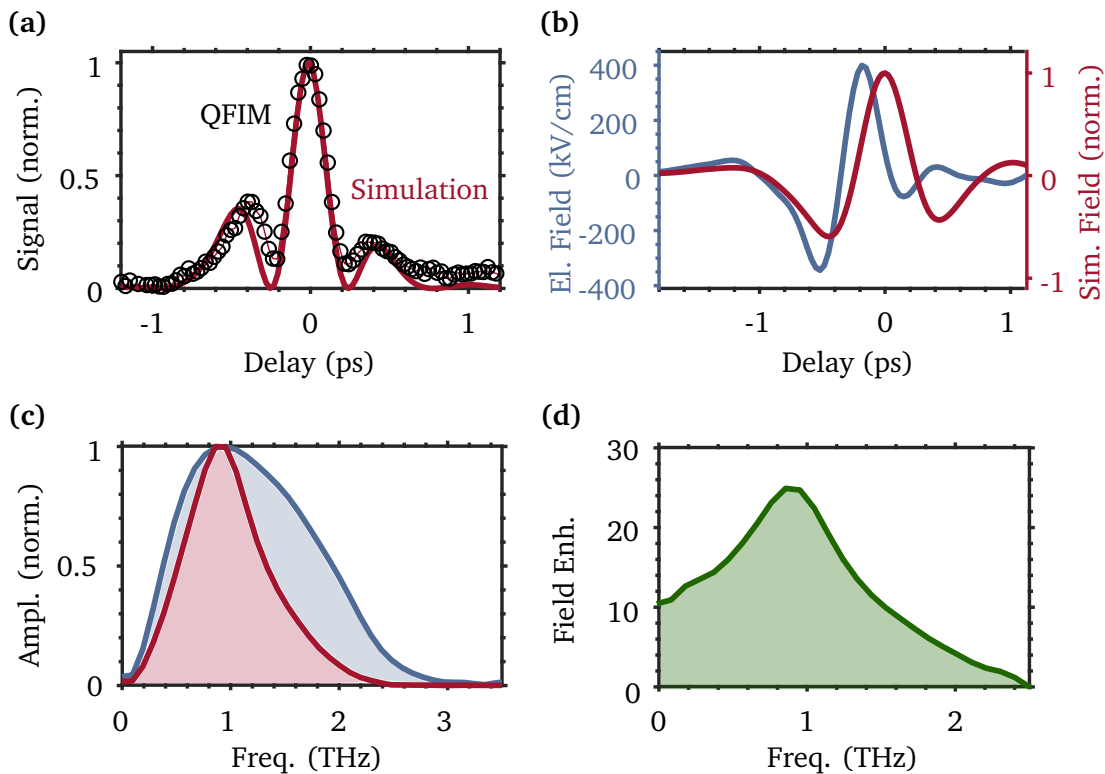


Fig. 6.6: Waveform analysis in the bowtie gap. (a) The QFIM trace, evaluated in the bowtie gap, shows good agreement with the simulated trace. We applied a CEP shift of 0.1π to the simulated waveform to account for uncertainty in the focus position. (b) For the time-transient simulation, we used the measured incident THz field (blue) as the driving field and calculated the THz near-field inside the bowtie gap (red). (c) The corresponding amplitude spectra for the waveforms from (b) show a broadband resonance of the antenna around 0.9 THz. (d) The frequency-dependent field enhancement close to the gold bars in the bowtie gap shows a peak field enhancement of 25 at 0.9 THz.

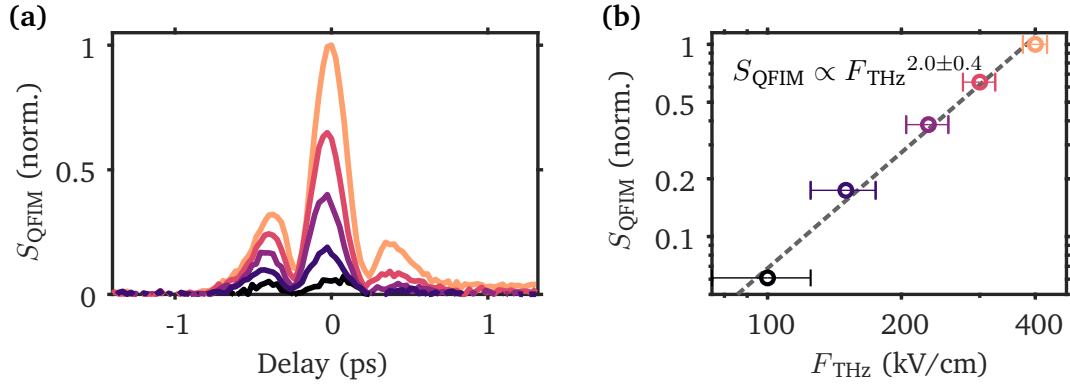


Fig. 6.7: Scaling of the QCSE in the bowtie antenna. (a) QFIM-traces for varying incident electric fields (100, 150, 240, 300, 400 kV cm^{-1}) measured with a PMT and a lockin-amplifier. We detune the efficiency of the generation process to lower the peak field strength, leading also to a slightly different waveform. (b) S_{QFIM} scales quadratically with the incident electric field, as determined with a linear fit (dashed line). For the data points, we average the time traces around the peak signal at 0 delay from (a). The error bars are estimated from the detuning process.

Based on the quadratic scaling, we model the QFIM dataset from the electric near-field simulated in the time-domain found on the incident THz waveform measured via EOS. The incoming electric field, along with the antenna-shaped field in the antenna gap, is provided in fig. 6.6(b). In particular, we evaluated the electric field close to the capacitive gold bars, providing the highest field enhancement. The corresponding Fourier spectra in fig. 6.6(c) show a broadband enhancement of the incident spectrum. From the spectral amplitudes, the frequency-dependent peak field enhancement factor close to the bars is determined to a value of 25 at 0.9 THz.

6.3 Mapping of field patterns in a split-ring resonator

Conventional THz-TDS is often used to study meta-materials such as filters by analysis of the transmitted THz radiation, but therefore only measures signals averaged over the whole THz spot on the sample, typically in the far-field. Here, we demonstrate the imaging of the transient response of a single gold electric split-ring resonator (eSRR, fig. 6.8) to a THz pulse [144] with polarization perpendicular to the capacitive gap. Six QFIM snapshots in fig. 6.9(a) reveal a spatially inhomogeneous pattern in the near-field of the antenna. Therefore, we evaluate the QFIM signal at two distinct regions: in the antenna gap and the edges of the capacitive bars, as indicated in the aforementioned figure. The resulting curves in fig. 6.9(b) showcase the capability of QFIM to investigate the near-field.

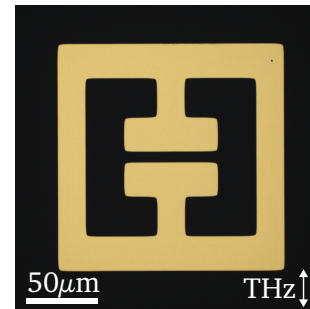


Fig. 6.8: THz eSRR.

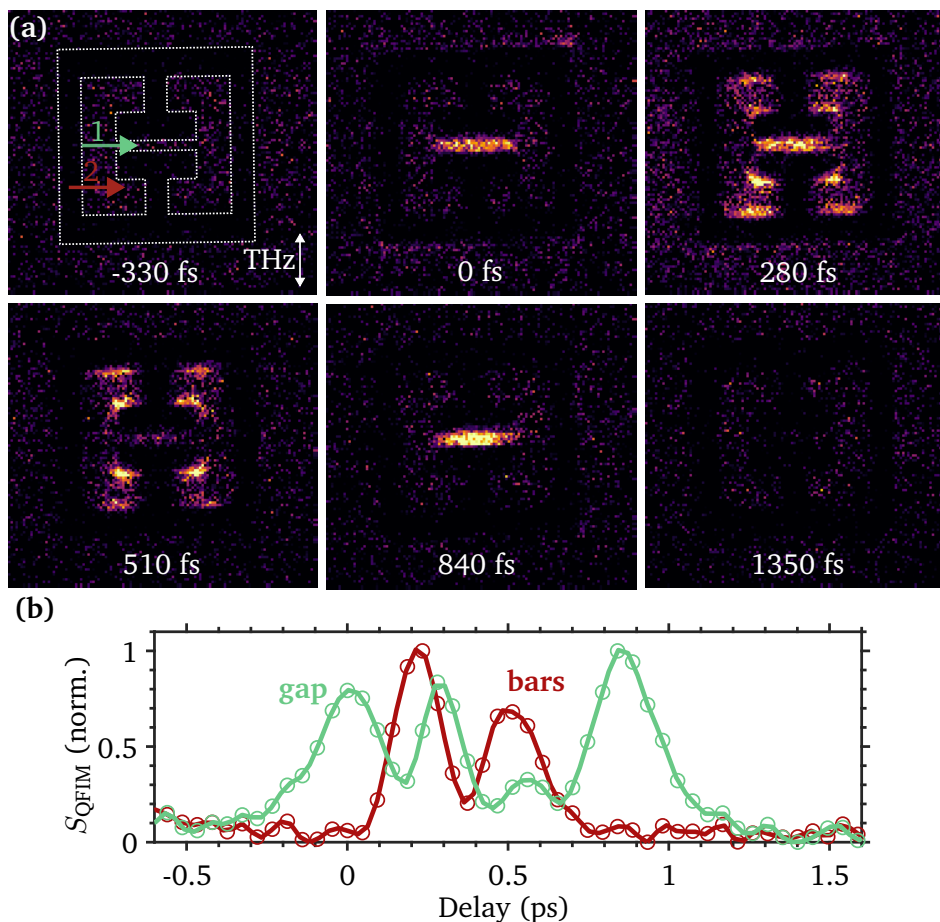


Fig. 6.9: QFIM snapshots of an electric split-ring resonator. (a) Six QFIM images at different temporal delays show the transient response of an eSRR. (b) The QFIM signal is evaluated in the gap (green) and at the bars of the capacitor (red), as also indicated in the first image of (a). The circles correspond to the data points, the lines to guides-to-the-eye.

6.4 Tracking of propagating terahertz waves in a sub-wavelength slit

The QFIM method also provides the possibility to detect spatio-temporal coupled effects – typically hidden to far-field detection methods. Therefore, we study gold slits in a periodic arrangement with sub-wavelength gaps of $2\ \mu\text{m}$ coated with quantum dots that we irradiate with strong THz pulses at the edge, as illustrated in fig. 6.10(b). Besides the non-resonant enhancement of the electric field in the gaps, the structure provides a slotline waveguide from another point-of-view, see fig. 6.10(a). THz waveguiding has been intensively studied in various structures, and a good overview is provided in ref. [145]. From theory, the wavelength of the propagation λ_{prop} in a slotline can be estimated in the quasi-static regime by using the relative permittivities from the substrate ϵ'_s and air $\epsilon_a = 1$ [146]:

$$\lambda_{\text{prop.}} = \frac{\lambda_0}{\sqrt{\frac{1+\epsilon'_s}{2}}} \quad (6.1)$$

Using for soda lime glass $\epsilon'_s = 6.78$ at 1 THz [92], the propagation wavelength is approximately $\lambda_0/2$. This means that the wave propagates in an effective refractive index of about two, and therefore, its speed is expected to be about half the speed of light in vacuum.

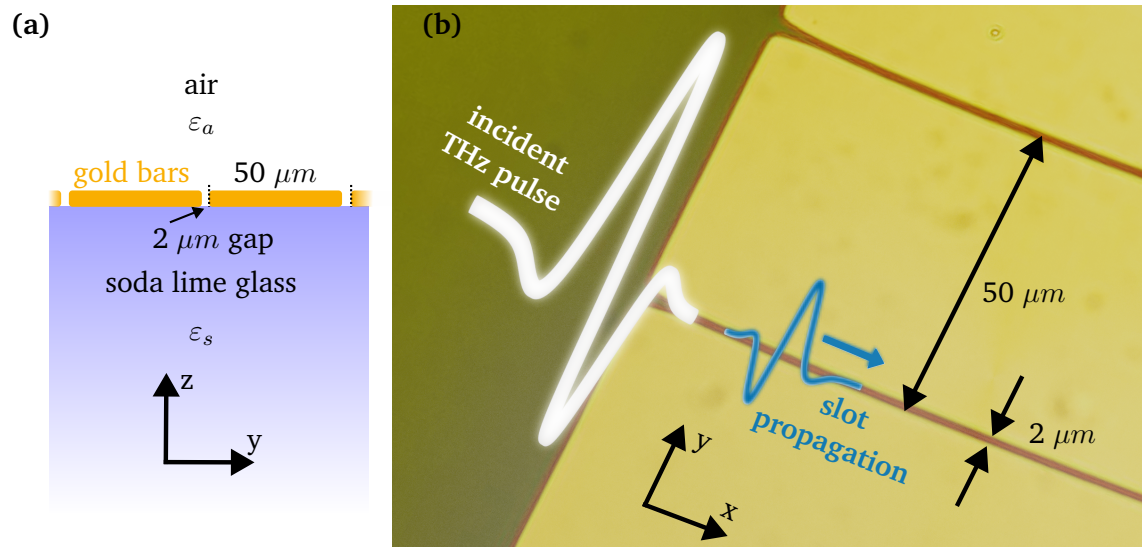


Fig. 6.10: Schematic of the launching of a THz slot propagation in a gold slit arrangement. (a) Geometry of the slot waveguide, as seen from the side. The gold bars have a height of roughly 150 nm, separated by $2\ \mu\text{m}$ with a $50\ \mu\text{m}$ periodicity. The dielectric environment is given by the soda lime glass substrate and air. (b) Top view of the slotlines. The gold slits (optical microscope image) are impinged by a THz pulse (white) with polarization perpendicular to the gaps. At the edges of the slits, waves (blue) are launched that propagate inside the structure.

We present the QFIM images in a 2d spatio-temporal representation (distance to the edge x , temporal delay $\Delta\tau$) in fig. 6.11(a) by averaging the signal perpendicular to the gap. This allows us to identify first the direct enhancement of the THz radiation inside the gap followed by a propagating wave that is launched at the edges of the slits and travels in the inside of the array. Here, we observe a propagation speed $c_{\text{prop.}}$ below the vacuum speed of light c_0 . At first sight, only the propagation of the second half-cycle is visible. However, due to the rather short propagation length that we observe, the propagation of the first half-cycle is only visible in a lowered QFIM signal around $(x, \Delta\tau) = (75 \mu\text{m}, 0.3 \text{ ps})$ in fig. 6.11(a). We simulate the electric field evolution of the THz pulse in the slotline in the time-domain and also identify the two regimes of direct enhancement and propagation of a wave inside the slit. The corresponding 2d representation of the simulated fields in fig. 6.11(c) shows, due to the full illumination of the slits, two gap excitations launched at the two edges of the structure. From the propagating waves, we estimate a mean propagation speed of $c_{\text{prop.}} \approx c_0/2$, in good agreement with the experimental finding. In the experiment, the THz focus is too small to hit both edges and, therefore, we move the sample, and the measured QFIM data reproduces the traveling wave at the opposite side of the slit array, as shown in fig. 6.11(b). We repeat the experiments for different slit lengths of $75 \mu\text{m}$, $100 \mu\text{m}$ and $150 \mu\text{m}$, smaller than the THz spot size of approximately $400 \mu\text{m}$. The results in the spatio-temporal 2d representation are shown in fig. 6.12. Generally, all slit lengths provide the incoupling at both edges, traveling inside the structure. In particular, the propagations superimpose each other in the center and, in the case of the two smaller samples, travel across each other. Especially from the dataset for $75 \mu\text{m}$, one can clearly see that the interaction of both waves leads to an increased signal.

The extraction of the propagation length of the slot excitation from the experimental data is not straightforward since the propagation is superimposed by the strong direct enhancement in the slits. Therefore, we subtract the signal in the region without propagation (beyond $140 \mu\text{m}$ in fig. 6.11(a)) and an exponential fit reveals a $1/e$ -propagation length of $l_{\text{prop.}} = (75 \pm 15) \mu\text{m}$ and is shown in fig. 6.13. Since the QCSE is proportional to the squared electric field, this value corresponds to the intensity propagation length. The related attenuation coefficient is $\alpha = 1/l_{\text{prop.}} = (133 \pm 30) \text{ cm}^{-1}$. The losses in the measured slotline are rather high compared, e.g., to a parallel-plate copper waveguide in air in ref. [147], where THz propagation is observed over 20 mm with an amplitude attenuation factor $\alpha_a < 0.2 \text{ cm}^{-1}$. In general, losses in slotlines can be divided into dielectric, conductor (metallic), and radiative losses [146].

First, concerning the dielectric losses, the permittivity of soda lime glass at a frequency of 1 THz is $\epsilon_s = 6.78 + i0.79$ [92], THz radiation suffers from significant loss in the glass as the (intensity) absorption coefficient $\alpha = \frac{4\pi\kappa}{\lambda_0} = 64 \text{ cm}^{-1}$, using the imaginary part of the refractive index of the glass κ and the wavelength of the THz radiation in vacuum λ_0

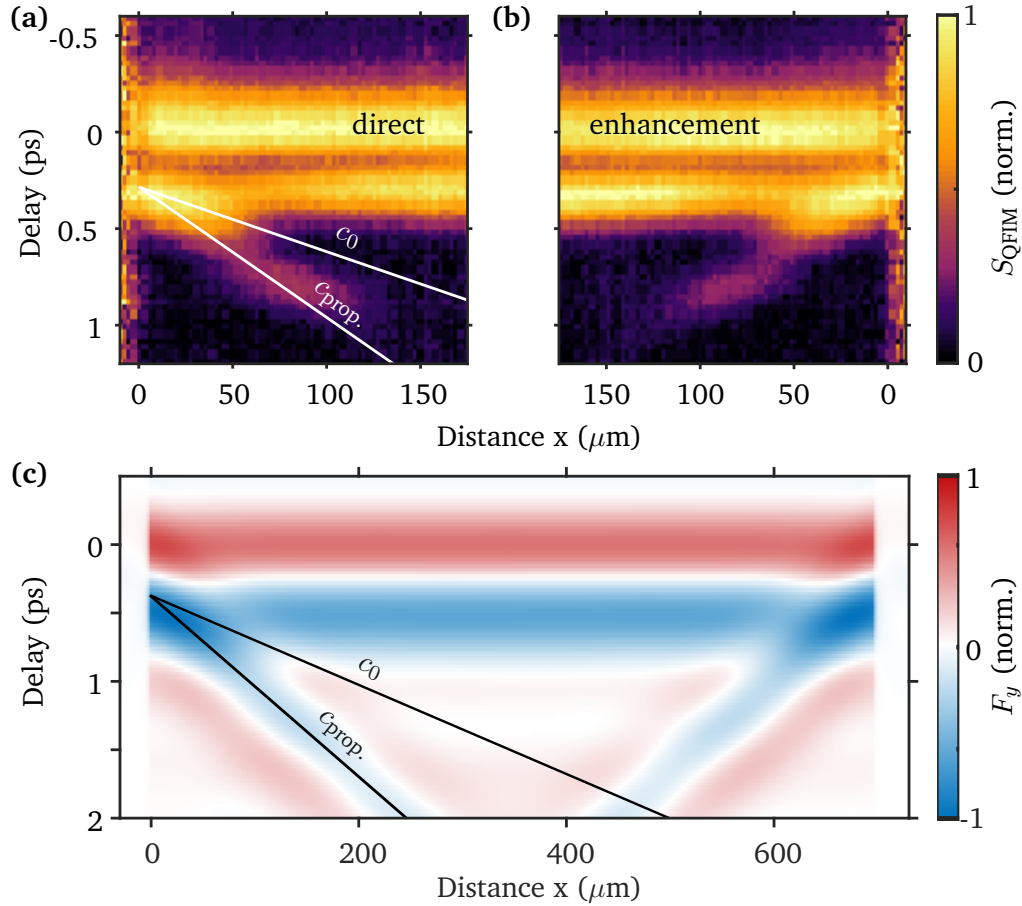


Fig. 6.11: Observation of direct enhancement and a THz slot propagation with QFIM. (a) The THz radiation hitting the left edge ($x = 0 \mu\text{m}$) of the slit array leads to a direct enhancement in the slits and a propagation that starts at the edge and propagates inside the gold structure. The propagation speed $c_{\text{prop.}} = c_0/2$ is taken from the field simulation in (c). For the 2d-representation, we average and normalize the QFIM signal in the slit and show the resulting data as a function of the distance to the edge and the temporal delay. (b) The analog experiment to (a) from the other side of the slit leads to a mirrored dataset, as the wave now travels in the opposite direction starting from the edge of the structure. (c) From a Comsol time-transient simulation, we show the resulting electric fields perpendicular to the gaps in the same 2d-representation as (a,b). The two regimes can be identified again, and a propagation speed of about $c_0/2$ is found.

at 1 THz [79]. Second, the gold film provides a finite conductivity that leads to losses, depending on the exact slot width in the order of a few cm^{-1} [148]. Last and typically the strongest loss channel is given by radiative losses into the substrate due to the large difference of the dielectric constants of air and the substrate and will depend strongly on the employed substrate and the overall dimensions of the slot [148, 149]. This kind of loss can be minimized by reducing the permittivity mismatch [148].

In the time-transient simulation, the metal film is approximated by a thin, perfect electric conductor. Therefore, metallic losses are neglected. Also, the substrate is assumed

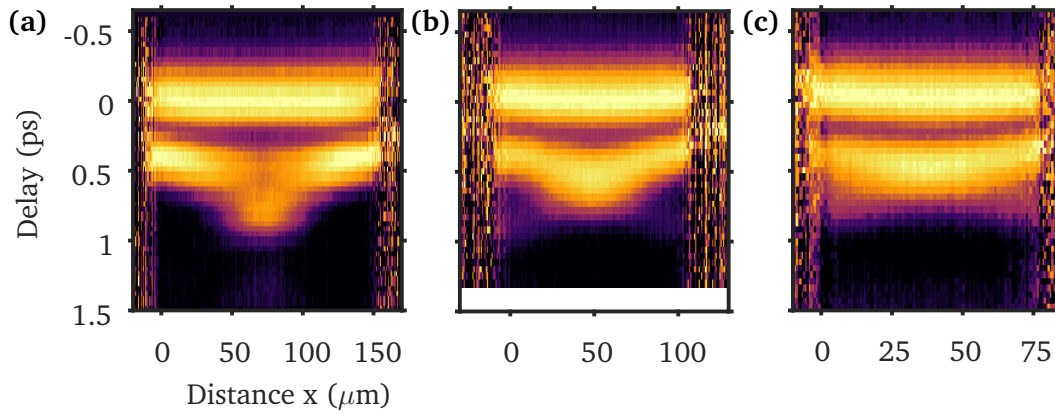


Fig. 6.12: THz slot propagation detected with QFIM for different slot lengths. (a) For a slot length of $150\ \mu\text{m}$, the two slot propagations launched at the edge add up in the center of the structure. (b) A shorter slot length of $100\ \mu\text{m}$ provides propagations that travel across each other. (c) The shortest slot length, $75\ \mu\text{m}$, shows propagations like in (b) that can be observed until the opposite side of the incoupling, even though they can not be separated from the direct enhancement as clearly as in the case of the longer slits.

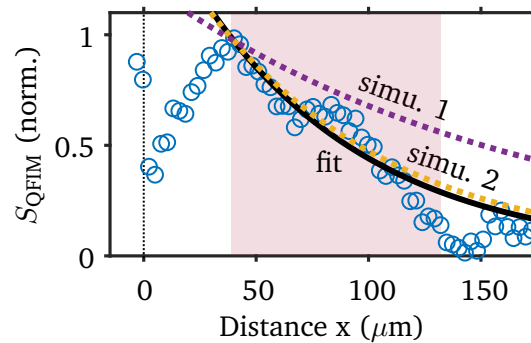


Fig. 6.13: Estimation of the propagation distance. The QFIM signal (circles) from fig. 6.11(a), after removing the direct enhancement, is fitted in the shaded area with an exponential decay (black). Due to the normalization process in the data treatment, not the whole curve can be fitted from the edge of the structure (vertical dashed line). The results from simulations incorporating radiative decay only (purple dashed) and all decay channels (yellow dashed) show a smaller and similar attenuation, respectively.

to be loss-free. Thus, the simulation does not take into account dielectric losses, only radiative losses. From the simulated electric fields in the time domain, we can roughly estimate $\alpha \approx 60\ \text{cm}^{-1}$. Using the open-source software „Characterization of Printed Transmission Lines at High Frequencies“, written in MATLAB [150], we can calculate the absorption coefficient at 1 THz incorporating also the finite conductivity of the gold and dielectric losses in the substrate to $\alpha \approx 120\ \text{cm}^{-1}$. This leads to a $1/e$ -intensity propagation length of about $85\ \mu\text{m}$, close to the estimation from the experimental QFIM data. The respective exponential decays from the simulations are also added in fig. 6.13.

6.5 Summary & outlook

Summarizing, we demonstrate the imaging of THz near-fields employing visible fluorescence of colloidal quantum dots. The electric fields are imprinted in changes in the absorption and, therefore, allow for the detection in the far-field using conventional fluorescence microscopy. This enables, along with ultrafast probe pulses, a sub-cycle and sub-diffraction limited detection, as we showcase exemplary for a single bowtie antenna. The spatial super-resolution is enabled by the huge difference between the pump and probe wavelength at $300\ \mu\text{m}$ (1 THz) and $0.645\ \mu\text{m}$, respectively. Especially, the all-optical readout permits the implementation of super-resolution techniques such as stimulated emission depletion (STED) microscopy, in order to reach a resolution better than 100 nm [139]. The near-field approach allows us to detect more complex mode patterns, as we show for a single eSRR. In particular, we investigate propagating THz waves in slit arrays with different dimensions. In future studies, the attenuation of the traveling wave can be reduced by using a substrate with less absorption and potentially a (more) homogeneous dielectric surrounding of the slotline.

Conclusion and outlook

In this work, we developed novel ultrafast terahertz (THz) near-field microscopy and spectroscopy techniques using colloidal CdSe-CdS core-shell quantum dots. Therefore, we used the quantum-confined Stark-effect (QCSE), that alters the optical properties of the nanocrystals. In detail, the two most apparent signatures of the QCSE are changes of the transition dipole moment upon an external electric field due to modified wavefunctions and a red-shift of the emission/absorption spectrum that scales quadratically with the electric field. We detect this effect via visible photons from the quantum dot luminescence. In combination with sampling of phase-stable far-infrared THz pulses in the time-domain, we achieve sub-cycle resolution of the oscillations of the electric waveforms.

First, we generated the THz pulses from an amplifier laser system in a nonlinear process using the tilted pulse front technique. Therefore, we designed and optimized a setup for the high-field source. We implemented the electro-optical sampling (EOS) method to characterize the THz waveform in the time-domain with absolute field strength calibration. The phase-stable single-cycle pulses with field strengths up to 400 kV/cm centered at a frequency of 1 THz built the foundation for our ultrafast QCSE experiments. In order to increase, shape, and localize the THz fields, we have developed different gold microstructures that enhance the THz fields up to several MV/cm. The development of the structures was guided by finite-element simulations to determine spatial and spectral field enhancement factors.

Second, a setup for terahertz-pump/optical-probe spectroscopy was implemented to investigate changes in the optical properties of quantum dots in strong fields with femtosecond temporal resolution. Here, sensitive techniques for detecting changes in the emission and absorption of the nanocrystals were employed based on lock-in or differential detection. In the experiments, we studied spectro-temporal modulations of the emission and absorption process in static and ultrashort electric fields. In addition to the quadratic scaling of the transition energy, we measured and confirmed via simulations that also the total change in the absorption scales quadratic before saturation occurs. In general, the momentary THz fields modulate optical transitions in the nanocrystals comparable to static fields, and the oscillations of the electric field are directly imprinted in the absorption of the quantum dots. In contrast, the emission process itself is not efficiently altered by the picosecond THz pulses due to the nanosecond radiative lifetime. Still, we observed a significant effect of the THz pulses in a time window of 10 picoseconds after a

quantum dot excitation with high fluence. First observations indicate that the THz pulses influence the picosecond dynamics of multiexcitons.

The QCSE in symmetric quantum dots is insensitive to the direction of the electric field. This complicates time-domain spectroscopy because only the rectified electric field is accessible. Therefore, we provided two techniques based on the Gouy-phase and the Hilbert transform to reconstruct the polarity. However, we achieved to experimentally resolve the polarity directly by introducing a static bias field in addition to the THz field that breaks the symmetry in the polarity. This is enabled by the quadratic scaling of the changes in the absorption of the quantum dots with the electric field. The differential changes induced by the bias practically yield the derivative of the quadratic scaling and result in an observable that represents the linear electric field. We implemented this method in an electro-absorptive THz antenna and characterized it in detail with respect to conventional EOS. Moreover, we demonstrated the first application of the device to THz time-domain spectroscopy.

As a main result of this thesis, we developed a novel ultrafast THz near-field microscopy technique called Quantum-Probe Field Microscopy (QFIM). Therefore, we imaged the THz-induced changes in the quantum dot emission with conventional fluorescence microscopy. This allows us to benefit from the optical resolution at 645 nm and the sub-cycle temporal resolution in the sampling process, leading to spatio-temporal mapping of strong THz near-fields with sub-cycle and sub-diffraction limited resolution. We introduced QFIM by recording ultrafast videos of MV/cm electric near-fields in a single THz bowtie antenna. From the measurement, we derived a spatial resolution of $2 \mu\text{m}$, far beyond the diffraction limit of the THz radiation. QFIM is inherently able to resolve spatially inhomogeneous field evolutions in the time-domain, as we showed for propagations in a THz sub-wavelength slotline waveguide. Our findings are supported by finite-element simulations of the near-field evolutions in the microstructures.

In summary, we introduced two new techniques based on the quantum-confined Stark-effect: Quantum-Probe Field Microscopy and the electro-absorptive quantum dot antenna. The efficient generation of phase-stable far-infrared pulses as an ultrafast field bias is described in detail, as well as the characterization of the picosecond THz pulses. As a basis, we experimentally investigated the QCSE in quantum dots in static and terahertz electric fields. Based on measurements, we explicitly worked out the similarities and differences between static and ultrafast fields in the QCSE. Especially the emission of the quantum dots after excitation can not be substantially modified. Here, we show a potential perspective to modulate the emission by creating fast decay channels via excitation with high fluence. The electro-absorptive quantum dot antenna enables the detection of ultrafast, polar electric fields using the unpolar QCSE. Therefore, we bypass the inability of quantum dots to sense the field direction by applying a differential, static bias field

that enables the linear detection. Finally, QFIM combines robust, far-field fluorescence microscopy with the QCSE and allows for super-resolution imaging of ultrafast terahertz waveforms in the time-domain enabling the access to confined MV/cm fields.

At this stage, the intrinsic physical limitations of QFIM and, in general, the QCSE have not been reached. Future developments may explore the temporal limits of the QCSE with phase-stable multi-THz pulses and suitable femtosecond sampling pulses. The combination of QFIM with optical super-resolution techniques such as STED microscopy may increase the spatial resolution far beyond $1 \mu\text{m}$ [139]. Higher THz fields lead to stronger modulations in the absorption, yet saturation will occur at some point. As an ultimate limit, the high fields alone may lead to THz-driven luminescence due to potential interdot charge transfer [140]. Besides the presented static biasing of the quantum dots, oriented asymmetric structures should provide for linear field sensing and imaging [86]. Moreover, in the case of a high fluence excitation, the regime of a single exciton in the quantum dots is surpassed, and multiexcitonic states are relevant in the interaction with THz fields, as first results on a THz enhanced emission indicate. This kind of transient modulation of luminescence by a THz pulse has not yet been described in the literature, and the finding could enable a new way to study multiexcitonic states with THz pulses.

Acronyms

ABCD air-breakdown coherent detection

ADC analog-digital converter

BD balanced photodetector

BS beam splitter

CEP carrier-envelope phase

DFG difference-frequency generation

DOS density of states

EOS electro-optical sampling

eSRR electric split-ring resonator

FOM figure of merit

FWHM full-width at half-maximum

HR-Si high-resistivity silicon

IAC interferometric autocorrelation

ML monolayer

ND neutral density

OPA optical parametric amplifier

OR optical rectification

PCA photoconductive antenna

PEC perfect electric conductor

PMC perfect magnetic conductor

PMT photo-multiplier tube

QCSE quantum-confined Stark-effect

QFIM Quantum-Probe Field Microscopy

SBC scattering boundary condition

SHG second harmonic generation

STED stimulated emission depletion

TDS time-domain spectroscopy

THz terahertz

TO-PR transversal-optical phonon resonance

UV ultraviolet

WL white light

WP Wollaston prism

Bibliography

1. Maxwell, J. C. VIII. A dynamical theory of the electromagnetic field. *Philosophical Transactions of the Royal Society of London* **155**, 459–512 (1865).
2. Hertz, H. Ueber electrodynamische Wellen im Luftraume und deren Reflexion. *Annalen der Physik* **270**, 609–623 (1888).
3. Franz, W. Einfluß eines elektrischen Feldes auf eine optische Absorptionskante. *Zeitschrift für Naturforschung A* **13**, 484–489 (1958).
4. Keldysh, L. V. Behavior of Non-metallic Crystals in Strong Electric Fields. *Soviet Journal of Experimental and Theoretical Physics* **6**, 763 (1958).
5. Miller, D. A. B. *et al.* Band-Edge Electroabsorption in Quantum Well Structures: The Quantum-Confined Stark Effect. *Physical Review Letters* **53**, 2173–2176 (1984).
6. Rossetti, R., Nakahara, S. & Brus, L. E. Quantum size effects in the redox potentials, resonance Raman spectra, and electronic spectra of CdS crystallites in aqueous solution. *The Journal of Chemical Physics* **79**, 1086–1088 (1983).
7. Ekimov, A., Efros, A. & Onushchenko, A. Quantum size effect in semiconductor microcrystals. *Solid State Communications* **56**, 921–924 (1985).
8. Murray, C. B., Norris, D. J. & Bawendi, M. G. Synthesis and characterization of nearly monodisperse CdE (E = sulfur, selenium, tellurium) semiconductor nanocrystallites. *Journal of the American Chemical Society* **115**, 8706–8715 (1993).
9. Empedocles, S. A. & Bawendi, M. G. Quantum-Confined Stark Effect in Single CdSe Nanocrystallite Quantum Dots. *Science* **278**, 2114–2117 (1997).
10. Hoffmann, M. C., Monozon, B. S., Livshits, D., Rafailov, E. U. & Turchinovich, D. Terahertz electro-absorption effect enabling femtosecond all-optical switching in semiconductor quantum dots. *Applied Physics Letters* **97**, 231108 (2010).
11. Huber, A. J., Keilmann, F., Wittborn, J., Aizpurua, J. & Hillenbrand, R. Terahertz Near-Field Nanoscopy of Mobile Carriers in Single Semiconductor Nanodevices. *Nano Letters* **8**, 3766–3770 (2008).
12. Basov, D. N., Fogler, M. M. & de Abajo, F. J. G. Polaritons in van der Waals materials. *Science* **354** (2016).
13. Lundeberg, M. B. *et al.* Tuning quantum nonlocal effects in graphene plasmonics. *Science* **357**, 187–191 (2017).

14. Jepsen, P. U., Jacobsen, R. H. & Keiding, S. R. Generation and detection of terahertz pulses from biased semiconductor antennas. *Journal of the Optical Society of America B* **13**, 2424 (1996).
15. Blanchard, F. *et al.* Real-time terahertz near-field microscope. *Optics Express* **19**, 8277 (2011).
16. Cocker, T. L. *et al.* An ultrafast terahertz scanning tunnelling microscope. *Nature Photonics* **7**, 620–625 (2013).
17. Von Ribbeck, H.-G. *et al.* Spectroscopic THz near-field microscope. *Optics Express* **16**, 3430–3438 (2008).
18. Ryabov, A. & Baum, P. Electron microscopy of electromagnetic waveforms. *Science* **353**, 374–377 (2016).
19. Koch, M., Mittleman, D. M., Ornik, J. & Castro-Camus, E. Terahertz time-domain spectroscopy. *Nature Reviews Methods Primers* **3**, 48 (2023).
20. Naftaly, Vieweg & Deninger. Industrial Applications of Terahertz Sensing: State of Play. *Sensors* **19**, 4203 (2019).
21. Leitenstorfer, A. *et al.* The 2023 terahertz science and technology roadmap. *Journal of Physics D: Applied Physics* **56**, 223001 (2023).
22. Neu, J. & Schmuttenmaer, C. A. Tutorial: An introduction to terahertz time domain spectroscopy (THz-TDS). *Journal of Applied Physics* **124**, 231101 (2018).
23. Fülöp, J. A., Tzortzakis, S. & Kampfrath, T. Laser-Driven Strong-Field Terahertz Sources. *Advanced Optical Materials* **8**, 1900681 (2020).
24. He, G. *Nonlinear optics and photonics* 1st ed. (Oxford University Press, Oxford, 2015).
25. Manzoni, C & Cerullo, G. Design criteria for ultrafast optical parametric amplifiers. *Journal of Optics* **18**, 103501 (2016).
26. Hoffmann, M. C. & Fülöp, J. A. Intense ultrashort terahertz pulses: generation and applications. *Journal of Physics D: Applied Physics* **44**, 083001 (2011).
27. Hafez, H. A. *et al.* Extremely efficient terahertz high-harmonic generation in graphene by hot Dirac fermions. *Nature* **561**, 507–511 (2018).
28. Maleki, A. *et al.* Strategies to enhance THz harmonic generation combining multi-layered, gated, and metamaterial-based architectures. **arXiv:2405.17125** (2024).
29. Auston, D. H. & Smith, P. R. Generation and detection of millimeter waves by picosecond photoconductivity. *Applied Physics Letters* **43**, 631–633 (1983).
30. Cook, D. J. & Hochstrasser, R. M. Intense terahertz pulses by four-wave rectification in air. *Optics Letters* **25**, 1210 (2000).

31. Dai, J., Xie, X. & Zhang, X.-C. Detection of Broadband Terahertz Waves with a Laser-Induced Plasma in Gases. *Physical Review Letters* **97**, 103903 (2006).
32. Karpowicz, N. *et al.* Coherent heterodyne time-domain spectrometry covering the entire “terahertz gap”. *Applied Physics Letters* **92**, 011131 (2008).
33. Seifert, T. *et al.* Efficient metallic spintronic emitters of ultrabroadband terahertz radiation. *Nature Photonics* **10**, 483–488 (2016).
34. Rouzegar, R. *et al.* Broadband Spintronic Terahertz Source with Peak Electric Fields Exceeding 1.5 MV/cm. *Physical Review Applied* **19**, 034018 (2023).
35. Chekhov, A. *et al.* Broadband Spintronic Detection of the Absolute Field Strength of Terahertz Electromagnetic Pulses. *Physical Review Applied* **20**, 034037 (2023).
36. Green, B. *et al.* High-Field High-Repetition-Rate Sources for the Coherent THz Control of Matter. *Scientific Reports* **6**, 22256 (2016).
37. Hebling, J., Yeh, K.-L., Hoffmann, M. C., Bartal, B. & Nelson, K. A. Generation of high-power terahertz pulses by tilted-pulse-front excitation and their application possibilities. *Journal of the Optical Society of America B* **25**, B6 (2008).
38. Wu, Q. & Zhang, X.-C. Ultrafast electro-optic field sensors. *Applied Physics Letters* **68**, 1604–1606 (1996).
39. Marple, D. T. F. Refractive Index of ZnSe, ZnTe, and CdTe. *Journal of Applied Physics* **35**, 539–542 (1964).
40. Skauli, T. *et al.* Improved dispersion relations for GaAs and applications to nonlinear optics. *Journal of Applied Physics* **94**, 6447–6455 (2003).
41. Pradarutti, B. *et al.* Highly efficient terahertz electro-optic sampling by material optimization at 1060nm. *Optics Communications* **281**, 5031–5035 (2008).
42. Bond, W. L. Measurement of the Refractive Indices of Several Crystals. *Journal of Applied Physics* **36**, 1674–1677 (1965).
43. Nakamura, M. *et al.* Optical Damage Resistance and Refractive Indices in Near-Stoichiometric MgO-Doped LiNbO₃. *Japanese Journal of Applied Physics* **41**, L49–L51 (2002).
44. Pan, F. *et al.* Electro-optic properties of the organic salt 4-N,N-dimethylamino-4'-N-methyl-stilbazolium tosylate. *Applied Physics Letters* **69**, 13–15 (1996).
45. Auston, D. H. Subpicosecond electro-optic shock waves. *Applied Physics Letters* **43**, 713–715 (1983).
46. Hebling, J., Almasi, G., Kozma, I. & Kuhl, J. Velocity matching by pulse front tilting for large area THz-pulse generation. *Optics Express* **10**, 1161 (2002).
47. Hebling, J. Derivation of the pulse front tilt caused by angular dispersion. *Opt Quant Electron* **28**, 1759–1763 (1996).

48. Pálfalvi, L., Hebling, J., Kuhl, J., Péter, Á. & Polgár, K. Temperature dependence of the absorption and refraction of Mg-doped congruent and stoichiometric LiNbO₃ in the THz range. *Journal of Applied Physics* **97**, 123505 (2005).
49. Pálfalvi, L. *et al.* Nonlinear refraction and absorption of Mg doped stoichiometric and congruent LiNbO₃. *Journal of Applied Physics* **95**, 902–908 (2004).
50. Fülöp, J. A., Pálfalvi, L., Almási, G. & Hebling, J. Design of high-energy terahertz sources based on optical rectification. *Optics Express* **18**, 12311 (2010).
51. Wang, L., Tóth, G., Hebling, J. & Kärtner, F. Tilted-Pulse-Front Schemes for Terahertz Generation. *Laser & Photonics Reviews* **14**, 2000021 (2020).
52. Tokodi, L., Hebling, J. & Pálfalvi, L. Optimization of the Tilted-Pulse-Front Terahertz Excitation Setup Containing Telescope. *Journal of Infrared, Millimeter, and Terahertz Waves* **38**, 22–32 (2017).
53. Wu, Q. & Zhang, X.-C. Free-space electro-optic sampling of terahertz beams. *Applied Physics Letters* **67**, 3523–3525 (1995).
54. Keiber, S. *et al.* Electro-optic sampling of near-infrared waveforms. *Nature Photonics* **10**, 159–162 (2016).
55. Boyd, R. W. *Nonlinear optics* 3rd ed. (Academic Press, Amsterdam, 2008).
56. Nye, J. F. *Physical properties of crystals: their representation by tensors and matrices* 1st published in pbk. with corrections (Oxford University Press, Oxford, 1985).
57. Loeffler, T. *Erzeugung intensiver Pulse im Terahertzfrequenzbereich mittels laser-generierter Plasmen* PhD thesis (Johann Wolfgang Goethe-Universität, Frankfurt am Main, 2003).
58. Planken, P. C. M., Nienhuys, H.-K., Bakker, H. J. & Wenckebach, T. Measurement and calculation of the orientation dependence of terahertz pulse detection in ZnTe. *Journal of the Optical Society of America B* **18**, 313 (2001).
59. Van Der Valk, N. C. J., Wenckebach, T. & Planken, P. C. M. Full mathematical description of electro-optic detection in optically isotropic crystals. *Journal of the Optical Society of America B* **21**, 622 (2004).
60. Wu, B., Cao, L., Fu, Q., Tan, P. & Xiong, Y. Comparison of the Detection Performance of Three Nonlinear Crystals for the Electro-optic Sampling of a FEL-THz Source. *Proceedings of the 5th Int. Particle Accelerator Conf. IPAC2014* (2014).
61. Bell, G. & Hilke, M. Polarization Effects of Electro-optic Sampling and Over-rotation for High Field THz Detection. *Journal of Infrared, Millimeter, and Terahertz Waves* **41**, 880–893 (2020).
62. Gallot, G. & Grischkowsky, D. Electro-optic detection of terahertz radiation. *Journal of the Optical Society of America B* **16**, 1204 (1999).

63. Berozashvili, Y., Machavariani, S, Natsvlishvili, A & Chirakadze, A. Dispersion of the linear electro-optic coefficients and the non-linear susceptibility in GaP. *Journal of Physics D: Applied Physics* **22**, 682–686 (1989).
64. *Handbook of optical constants of solids II* (ed Palik, E. D.) (Academic Press, Boston, 1991).
65. Nelson, D. F. & Turner, E. H. Electro-optic and Piezoelectric Coefficients and Refractive Index of Gallium Phosphide. *Journal of Applied Physics* **39**, 3337–3343 (1968).
66. Kaltenecker, K. J., Kelleher, E. J. R., Zhou, B. & Jepsen, P. U. Attenuation of THz Beams: A “How to” Tutorial. *Journal of Infrared, Millimeter, and Terahertz Waves* **40**, 878–904 (2019).
67. Blanchard, F., Nkeck, J. E., Matte, D., Nechache, R. & Cooke, D. G. A Low-Cost Terahertz Camera. *Applied Sciences* **9**, 2531 (2019).
68. Self, S. A. Focusing of spherical Gaussian beams. *Applied Optics* **22**, 658 (1983).
69. Pampaloni, F. & Enderlein, J. Gaussian, Hermite-Gaussian, and Laguerre-Gaussian beams: A primer. [arXiv:physics/0410021](https://arxiv.org/abs/physics/0410021) (2004).
70. Porras, M. A. Characterization of the electric field of focused pulsed Gaussian beams for phase-sensitive interactions with matter. *Optics Letters* **34**, 1546 (2009).
71. Hoff, D. *et al.* Tracing the phase of focused broadband laser pulses. *Nature Physics* **13**, 947–951 (2017).
72. Hoffmann, M. C., Yeh, K.-L., Hebling, J. & Nelson, K. A. Efficient terahertz generation by optical rectification at 1035 nm. *Optics Express* **15**, 11706 (2007).
73. Sitnikov, D. S. *et al.* Estimation of THz field strength by an electro-optic sampling technique using arbitrary long gating pulses. *Laser Physics Letters* **16**, 115302 (2019).
74. Ashcroft, N. W. & Mermin, N. D. *Solid state physics* (Saunders college publishing, New York, 1976).
75. Weis, P. *et al.* Spectrally Wide-Band Terahertz Wave Modulator Based on Optically Tuned Graphene. *ACS Nano* **6**, 9118–9124 (2012).
76. Cuevas, A. & Macdonald, D. Measuring and interpreting the lifetime of silicon wafers. *Solar Energy* **76**, 255–262 (2004).
77. Wehrenfennig, C., Eperon, G. E., Johnston, M. B., Snaith, H. J. & Herz, L. M. High Charge Carrier Mobilities and Lifetimes in Organolead Trihalide Perovskites. *Advanced Materials* **26**, 1584–1589 (2014).
78. Novotny, L. & Hecht, B. *Principles of Nano-Optics* 2nd ed. (Cambridge University Press, Cambridge, 2012).

79. Dressel, M. & Grüner, G. *Electrodynamics of solids: optical properties of electrons in matter* (Cambridge University Press, Cambridge, 2002).
80. Olmon, R. L. *et al.* Optical dielectric function of gold. *Physical Review B* **86**, 235147 (2012).
81. Brändli, G. & Sievers, A. J. Absolute Measurement of the Far-Infrared Surface Resistance of Pb. *Physical Review B* **5**, 3550–3557 (1972).
82. Ordal, M. A. *et al.* Optical properties of the metals Al, Co, Cu, Au, Fe, Pb, Ni, Pd, Pt, Ag, Ti, and W in the infrared and far infrared. *Applied Optics* **22**, 1099 (1983).
83. Tsiatmas, A., Fedotov, V. A., García De Abajo, F. J. & Zheludev, N. I. Low-loss terahertz superconducting plasmonics. *New Journal of Physics* **14**, 115006 (2012).
84. Feynman, R. P. *The Feynman lectures on physics. Volume 2: Mainly electromagnetism and matter* The new millennium edition, paperback first published (Basic Books, New York, 2011).
85. Haynes, W. M. *CRC Handbook of Chemistry and Physics* 95th ed. (CRC Press, Hoboken, 2014).
86. Park, K., Deutsch, Z., Li, J. J., Oron, D. & Weiss, S. Single Molecule Quantum-Confined Stark Effect Measurements of Semiconductor Nanoparticles at Room Temperature. *ACS Nano* **6**, 10013–10023 (2012).
87. Novitsky, A. *et al.* Non-resonant terahertz field enhancement in periodically arranged nanoslits. *Journal of Applied Physics* **112**, 074318 (2012).
88. Shalaby, M. *et al.* Concurrent field enhancement and high transmission of THz radiation in nanoslit arrays. *Applied Physics Letters* **99**, 041110 (2011).
89. *RF Module User's Guide 5.4* <https://doc.comsol.com/5.4/doc/com.comsol.help.rf/RFModuleUsersGuide.pdf>. Accessed: 2024-06-20. COMSOL Multiphysics, 2018.
90. *Resolving Time-Dependent Waves - Knowledge Base 1118* <https://www.comsol.com/support/knowledgebase/1118>. Accessed: 2024-06-24. COMSOL Multiphysics.
91. *Acoustics Module User's Guide 5.4* <https://doc.comsol.com/5.4/doc/com.comsol.help.aco/AcousticsModuleUsersGuide.pdf>. Accessed: 2024-06-20. COMSOL Multiphysics, 2018.
92. Rubin, M. Optical properties of soda lime silica glasses. *Solar Energy Materials* **12**, 275–288 (1985).
93. Pein, B. C. *et al.* Terahertz-Driven Stark Spectroscopy of CdSe and CdSe–CdS Core–Shell Quantum Dots. *Nano Letters* **19**, 8125–8131 (2019).
94. Green, M. The nature of quantum dot capping ligands. *Journal of Materials Chemistry* **20**, 5797 (2010).

95. Bozyigit, D., Yarema, O. & Wood, V. Origins of Low Quantum Efficiencies in Quantum Dot LEDs. *Advanced Functional Materials* **23**, 3024–3029 (2013).
96. Gollner, C. *et al.* Ultrafast Electro-Absorption Switching in Colloidal CdSe/CdS Core/Shell Quantum Dots Driven by Intense THz Pulses. *Advanced Optical Materials* **10**, 2102407 (2022).
97. Sacra, A., Norris, D. J., Murray, C. B. & Bawendi, M. G. Stark spectroscopy of CdSe nanocrystallites: The significance of transition linewidths. *The Journal of Chemical Physics* **103**, 5236–5245 (1995).
98. Aubret, A., Orrit, M. & Kulzer, F. Understanding Local-Field Correction Factors in the Framework of the Onsager-Böttcher Model. *ChemPhysChem* **20**, 345–355 (2019).
99. Bublitz, G. U. & Boxer, S. G. Stark Spectroscopy: Applications in Chemistry, Biology, and Materials Science. *Annual Review of Physical Chemistry* **48**, 213–242 (1997).
100. Stark, J. Observation of the Separation of Spectral Lines by an Electric Field. *Nature* **92**, 401–401 (1913).
101. Harrison, P. & Valavanis, A. *Quantum wells, wires and dots: theoretical and computational physics of semiconductor nanostructures* 4th ed. (John Wiley & Sons, Chichester, 2016).
102. Grivas, C. *et al.* Single-mode tunable laser emission in the single-exciton regime from colloidal nanocrystals. *Nature Communications* **4**, 2376 (2013).
103. Piryatinski, A., Ivanov, S. A., Tretiak, S. & Klimov, V. I. Effect of Quantum and Dielectric Confinement on the Exciton-Exciton Interaction Energy in Type II Core/Shell Semiconductor Nanocrystals. *Nano Letters* **7**, 108–115 (2007).
104. Nandan, Y. & Mehata, M. S. Wavefunction Engineering of Type-I/Type-II Excitons of CdSe/CdS Core-Shell Quantum Dots. *Scientific Reports* **9**, 2 (2019).
105. *Nanocrystal quantum dots* 2nd ed. (ed Klimov, V. I.) (CRC Press, Boca Raton, 2010).
106. Kantner, M. *Electrically Driven Quantum Dot Based Single-Photon Sources: Modeling and Simulation* 1st ed. (Springer International Publishing, Cham, 2020).
107. Mastria, R. & Rizzo, A. Mastering heterostructured colloidal nanocrystal properties for light-emitting diodes and solar cells. *Journal of Materials Chemistry C* **4**, 6430–6446 (2016).
108. Hiroshima, T. & Lang, R. Well size dependence of Stark shifts for heavy-hole and light-hole levels in GaAs/AlGaAs quantum wells. *Applied Physics Letters* **49**, 639–641 (1986).
109. Harris, C. R. *et al.* Array programming with NumPy. *Nature* **585**, 357–362 (2020).

110. Şahin, M., Nizamoglu, S., Kavruk, A. E. & Demir, H. V. Self-consistent computation of electronic and optical properties of a single exciton in a spherical quantum dot via matrix diagonalization method. *Journal of Applied Physics* **106**, 043704 (2009).
111. Efros, Al. L. *et al.* Band-edge exciton in quantum dots of semiconductors with a degenerate valence band: Dark and bright exciton states. *Physical Review B* **54**, 4843–4856 (1996).
112. Jaskólski, W. & Bryant, G. W. Multiband theory of quantum-dot quantum wells: Dim excitons, bright excitons, and charge separation in heteronanostructures. *Physical Review B* **57**, R4237–R4240 (1998).
113. *Manual SR850 – Lock-in Amplifier, Rev. 2.0* (Stanford Research Systems, Sunnyvale, 2009).
114. *Signal Recovery with PMTs* <https://www.thinksrs.com/downloads/pdfs/applicationnotes/SignalRecovery.pdf>. Accessed: 2024-06-24. Stanford Research Systems.
115. Heindl, M. B. *et al.* Ultrafast imaging of terahertz electric waveforms using quantum dots. *Light: Science & Applications* **11**, 5 (2022).
116. Ghosh, Y. *et al.* New Insights into the Complexities of Shell Growth and the Strong Influence of Particle Volume in Nonblinking “Giant” Core/Shell Nanocrystal Quantum Dots. *Journal of the American Chemical Society* **134**, 9634–9643 (2012).
117. Colvin, V. L., Cunningham, K. L. & Alivisatos, A. P. Electric field modulation studies of optical absorption in CdSe nanocrystals: Dipolar character of the excited state. *The Journal of Chemical Physics* **101**, 7122–7138 (1994).
118. Hache, F., Ricard, D. & Flytzanis, C. Quantum-confined Stark effect in very small semiconductor crystallites. *Applied Physics Letters* **55**, 1504–1506 (1989).
119. Colvin, V. L. & Alivisatos, A. P. CdSe nanocrystals with a dipole moment in the first excited state. *The Journal of Chemical Physics* **97**, 730–733 (1992).
120. Kuo, Y. *et al.* Characterizing the Quantum-Confined Stark Effect in Semiconductor Quantum Dots and Nanorods for Single-Molecule Electrophysiology. *ACS Photonics* **5**, 4788–4800 (2018).
121. Rowland, C. E. *et al.* Electric Field Modulation of Semiconductor Quantum Dot Photoluminescence: Insights Into the Design of Robust Voltage-Sensitive Cellular Imaging Probes. *Nano Letters* **15**, 6848–6854 (2015).
122. Guicking, D. *Schwingungen* 1st ed. (Springer Fachmedien Wiesbaden, Wiesbaden, 2016).
123. *Photoactive Semiconductor Nanocrystal Quantum Dots: Fundamentals and Applications* 1st ed. (ed Credi, A.) (Springer International Publishing, Cham, 2017).

124. Melnychuk, C. & Guyot-Sionnest, P. Multicarrier Dynamics in Quantum Dots. *Chemical Reviews* **121**, 2325–2372 (2021).
125. Karki, K. J. *et al.* Multiple exciton generation in nano-crystals revisited: Consistent calculation of the yield based on pump-probe spectroscopy. *Scientific Reports* **3**, 2287 (2013).
126. Shabaev, A., Hellberg, C. S. & Efros, A. L. Efficiency of Multiexciton Generation in Colloidal Nanostructures. *Accounts of Chemical Research* **46**, 1242–1251 (2013).
127. Shi, J. *et al.* Terahertz Field-Induced Reemergence of Quenched Photoluminescence in Quantum Dots. *Nano Letters* **22**, 1718–1725 (2022).
128. Klimov, V. I., Mikhailovsky, A. A., McBranch, D. W., Leatherdale, C. A. & Bawendi, M. G. Quantization of Multiparticle Auger Rates in Semiconductor Quantum Dots. *Science* **287**, 1011–1013 (2000).
129. Sha, W., Norris, T. B., Burm, J. W., Woodard, D. & Schaff, W. J. New coherent detector for terahertz radiation based on excitonic electroabsorption. *Applied Physics Letters* **61**, 1763–1765 (1992).
130. Aguilar, M. *et al.* Linear electroabsorption in semi-insulating GaAs/AlGaAs asymmetric double quantum wells. *Journal of Applied Physics* **86**, 3822–3825 (1999).
131. Grischkowsky, D., Keiding, S., Van Exter, M. & Fattinger, Ch. Far-infrared time-domain spectroscopy with terahertz beams of dielectrics and semiconductors. *Journal of the Optical Society of America B* **7**, 2006 (1990).
132. Weiner, A. M. *Ultrafast Optics* 1st ed. (John Wiley & Sons, Hoboken, 2009).
133. van Exter, M., Fattinger, Ch. & Grischkowsky, D. Terahertz time-domain spectroscopy of water vapor. *Optics Letters* **14**, 1128 (1989).
134. Gordon, I. *et al.* The HITRAN2020 molecular spectroscopic database. *Journal of Quantitative Spectroscopy and Radiative Transfer* **277**, 107949 (2022).
135. Duvillaret, L., Garet, F. & Coutaz, J.-L. A reliable method for extraction of material parameters in terahertz time-domain spectroscopy. *IEEE Journal of Selected Topics in Quantum Electronics* **2**, 739–746 (1996).
136. Diroll, B. T. Optical stark effect on CdSe nanoplatelets with mid-infrared excitation for large amplitude ultrafast modulation. *Nanotechnology* **34**, 245706 (2023).
137. Turchinovich, D. *Encoding an optical signal using a radio-frequency signal* US 2012/0148252 A1. Patent 2012.
138. Gao, X. *et al.* In vivo molecular and cellular imaging with quantum dots. *Current Opinion in Biotechnology* **16**, 63–72 (2005).
139. Hanne, J. *et al.* STED nanoscopy with fluorescent quantum dots. *Nature Communications* **6**, 7127 (2015).

140. Pein, B. C. *et al.* Terahertz-Driven Luminescence and Colossal Stark Effect in CdSe–CdS Colloidal Quantum Dots. *Nano Letters* **17**, 5375–5380 (2017).
141. Shi, J. *et al.* A room-temperature polarization-sensitive CMOS terahertz camera based on quantum-dot-enhanced terahertz-to-visible photon upconversion. *Nature Nanotechnology* **17**, 1288–1293 (2022).
142. Balanis, C. A. *Antenna theory: analysis and design* 3rd ed. (John Wiley & Sons, Hoboken, 2005).
143. Abbe, E. Beiträge zur Theorie des Mikroskops und der mikroskopischen Wahrnehmung. *Archiv für Mikroskopische Anatomie* **9**, 413–468 (1873).
144. Schurig, D., Mock, J. J. & Smith, D. R. Electric-field-coupled resonators for negative permittivity metamaterials. *Applied Physics Letters* **88**, 041109 (2006).
145. Koala, R. A. S. D., Fujita, M. & Nagatsuma, T. Nanophotonics-inspired all-silicon waveguide platforms for terahertz integrated systems. *Nanophotonics* **11**, 1741–1759 (2022).
146. Edwards, T. C. & Steer, M. B. *Foundations for Microstrip Circuit Design* 1st ed. (John Wiley & Sons, Hoboken, 2016).
147. Mendis, R. & Grischkowsky, D. Undistorted guided-wave propagation of subpicosecond terahertz pulses. *Optics Letters* **26**, 846 (2001).
148. Pahlevaninezhad, H., Heshmat, B. & Darcie, T. E. Efficient terahertz slot-line waveguides. *Optics Express* **19**, B47 (2011).
149. Grischkowsky, D., Duling III, I. N., Chen, J. C. & Chi, C. C. Electromagnetic shock waves from transmission lines. *Physical Review Letters* **59**, 1663–1666 (1987).
150. S. L. Van Berkel, A. Garufo, A. Endo, N. Lombart & A. Neto. *Characterization of printed transmission lines at high frequencies in The 9th European Conference on Antennas and Propagation (EuCAP 2015)* (Lisbon, Portugal, 2015).

Eidesstattliche Versicherung

Hiermit versichere ich an Eides statt, dass ich die vorliegende Arbeit selbstständig verfasst und keine anderen als die von mir angegebenen Quellen und Hilfsmittel verwendet habe. Weiterhin erkläre ich, dass ich die Hilfe von gewerblichen Promotionsberatern bzw. -vermittlern oder ähnlichen Dienstleistern weder bisher in Anspruch genommen habe, noch künftig in Anspruch nehmen werde.

Zusätzlich erkläre ich hiermit, dass ich keinerlei frühere Promotionsversuche unternommen habe.

Ort, Datum

Moritz Benedikt Heindl

Acknowledgement

Als Erstes möchte ich Prof. Georg Herink danken, dass er mich als seinen ersten Doktoranden geleitet und mit unzerstörbarer Freude an der Physik immer wieder motiviert hat. Denn jedem Anfang wohnt ein „*Sauber!*“ (sic!) inne. Ebenso möchte ich Prof. Markus Lippitz danken, dass er mich zu dieser Promotion ermutigt hat.

I want to thank Nicholas Kirkwood and Hua Zhou for providing the CdSe-CdS quantum dots. Mein Dank gilt auch Tobias Lauster, Stefan Rettinger und Nelson Pech-May für die Photolithographie-Strukturen, die oft am Besten gestern fertig sein sollten. Auch danke ich Simon Biberger für die Gold-Beschichtung der Strukturen.

Ebenfalls danke ich allen EP3(+5)lern, die stets hilfsbereit, freundlich und motiviert waren. Ich danke Dr. Thorsten Schumacher fürs Couchteilen, physikalische und unphysikalische Diskussionen. Julia Lang hat es lange mit mir im Büro ausgehalten und mir auf unkonventionelle Weise mit einer guten Portion Galgenhumor so manches erleichtert. Danke an meinen anfänglichen Bürokollegen Michael Seidel, der mir insbesondere die DPG Konferenzen und gemeinsame Fussballabende zu einem unvergleichlichen Event werden hat lassen. Danke an Valentin Dichtl für seinen Glauben ans Gute und seine Kochkünste. Vorrei ringraziare Robert Weiner, detto Don Rob, per la sua amicizia, le sue battute e i suoi eccellenti programmi LabView e componenti elettronici. Ebenso danke ich Angelika Maier-Raithel für top Organisation.

Ich danke auch pauschal dem Uniorchester, mich von der Physik abgelenkt zu haben, was auch manchmal nötig war. Ebenso danke ich meinem Klavierlehrer Eduard Hubert für fast schon psychotherapeutischen Klavierunterricht, der mein Klavierspiel auf ein höheres Niveau gebracht hat.

Zu guter Letzt - und sicher nicht am wenigsten - möchte ich mich bei meinen Eltern bedanken, die mich in allem, was ich bin, geprägt haben und die mich zu dem werden ließen, was ich werden wollte. Euer Vertrauen in mich hab ich als bedingungslos wahrgenommen. Gleichsam danke ich meinen Brüdern Felix und Christoph, meiner Schwägerin Katharina und meinen Großeltern, dass sie gleichzeitig Interesse und Desinteresse an meiner Arbeit gezeigt haben. Schließlich danke ich meiner Sophie, die mich unterstützt und von allem ablenkt, was nicht wichtig ist!

Colophon

This thesis was typeset with \LaTeX 2 ϵ . It uses the *Clean Thesis* style developed by Ricardo Langner. The design of the *Clean Thesis* style is inspired by user guide documents from Apple Inc.

Download the *Clean Thesis* style at <http://cleanthesis.der-ric.de/>.